

Parameterizing mesoscale eddy buoyancy transport over sloping topography

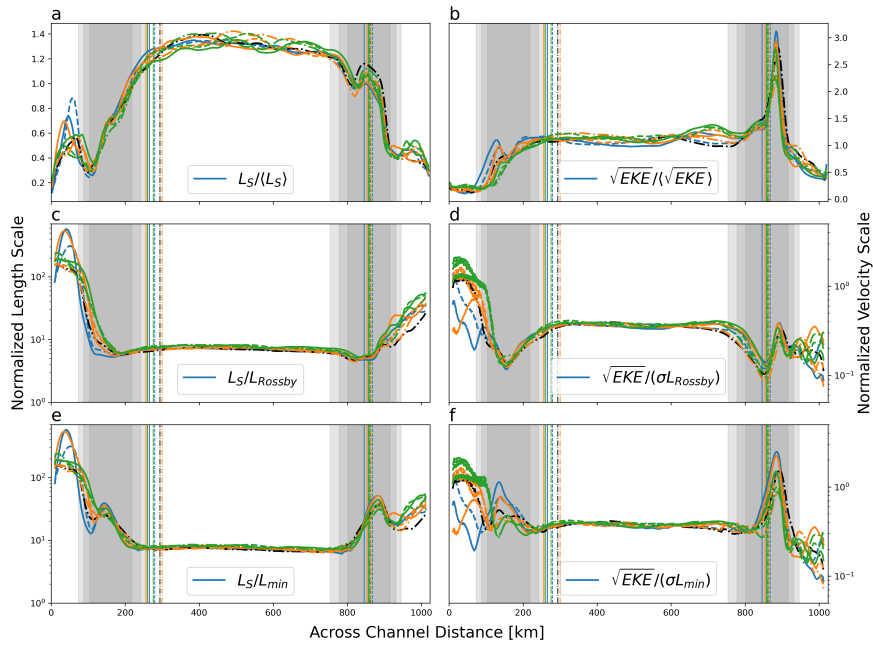
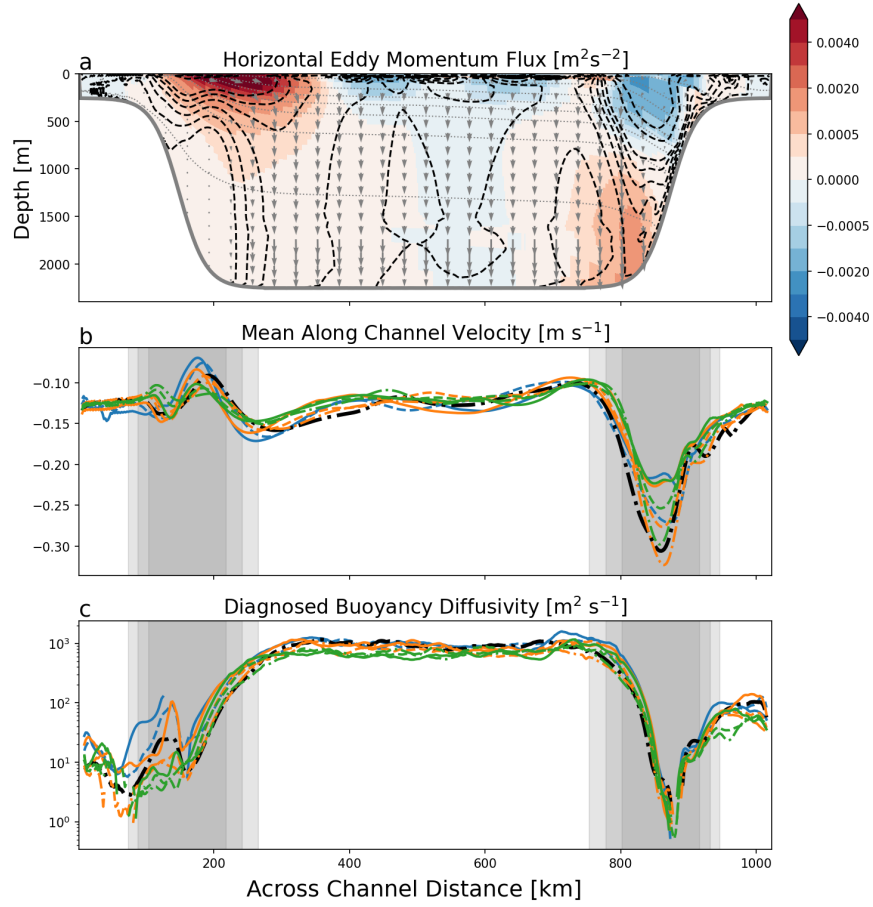
Aleksi Nummelin¹ and Pål Erik Isachsen¹

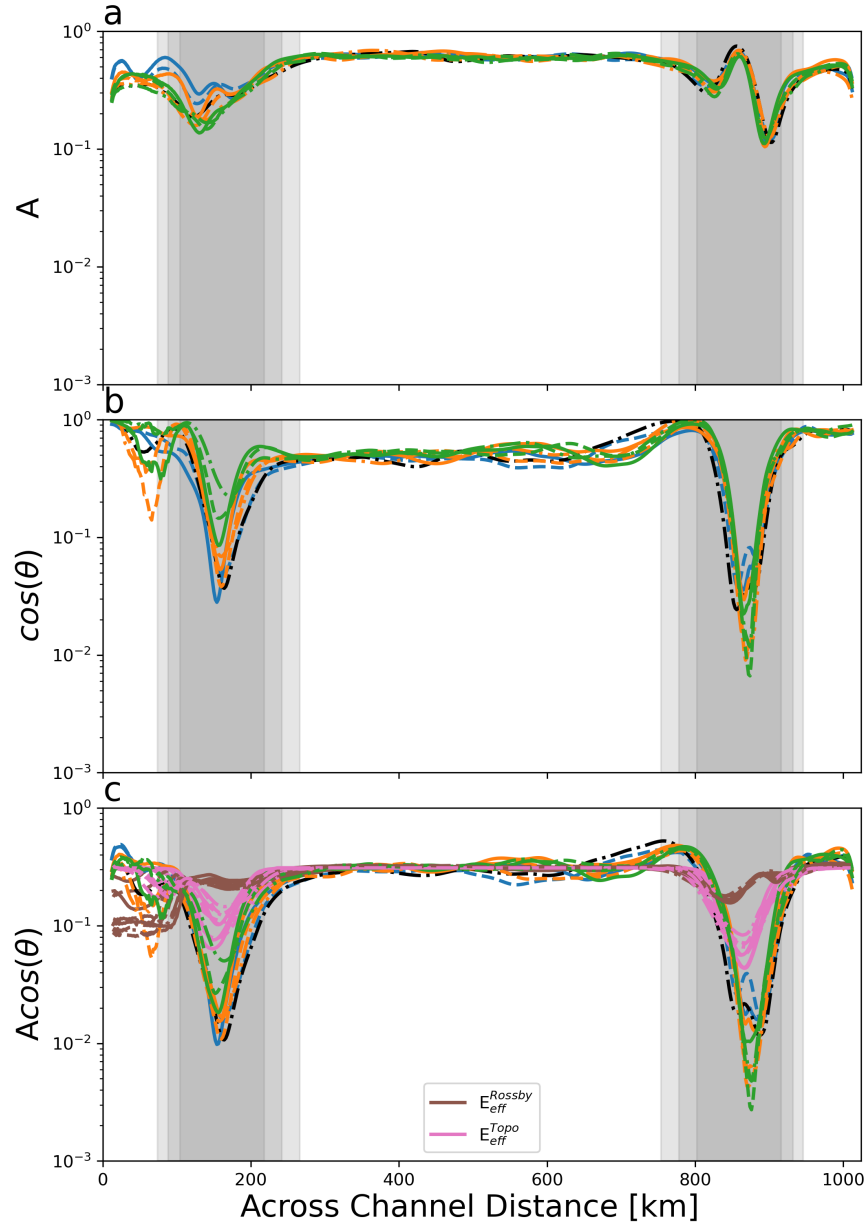
¹University of Oslo

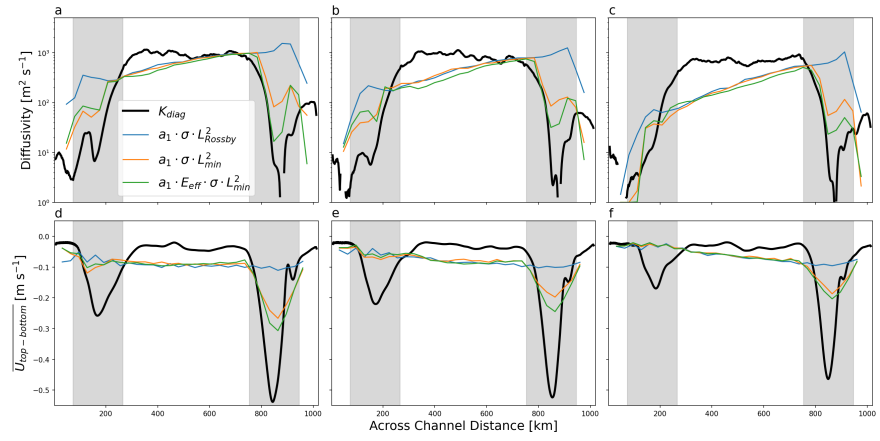
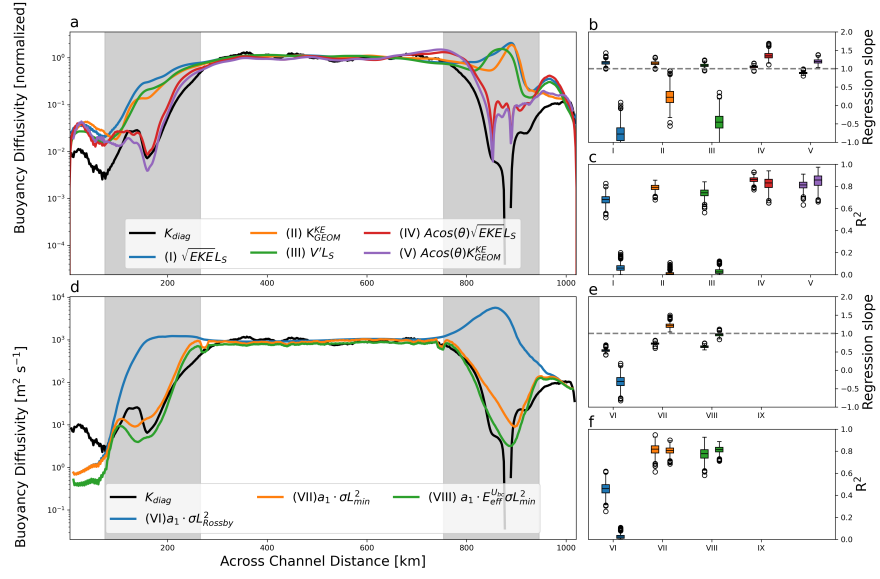
May 13, 2023

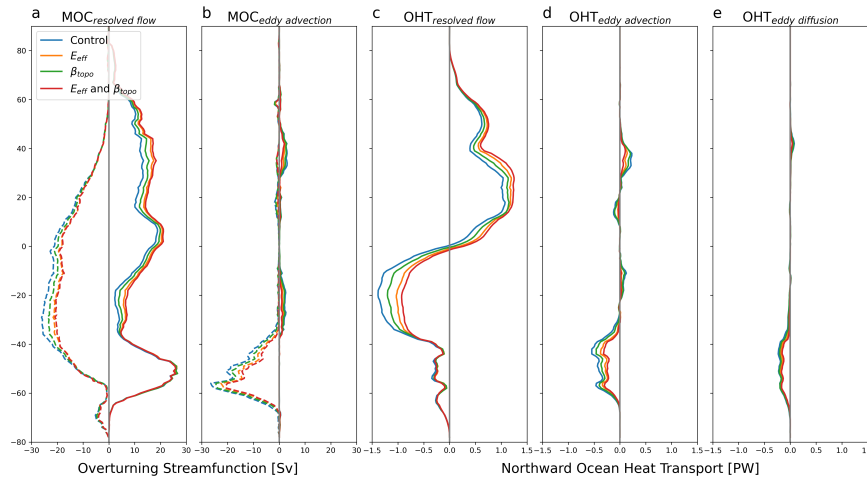
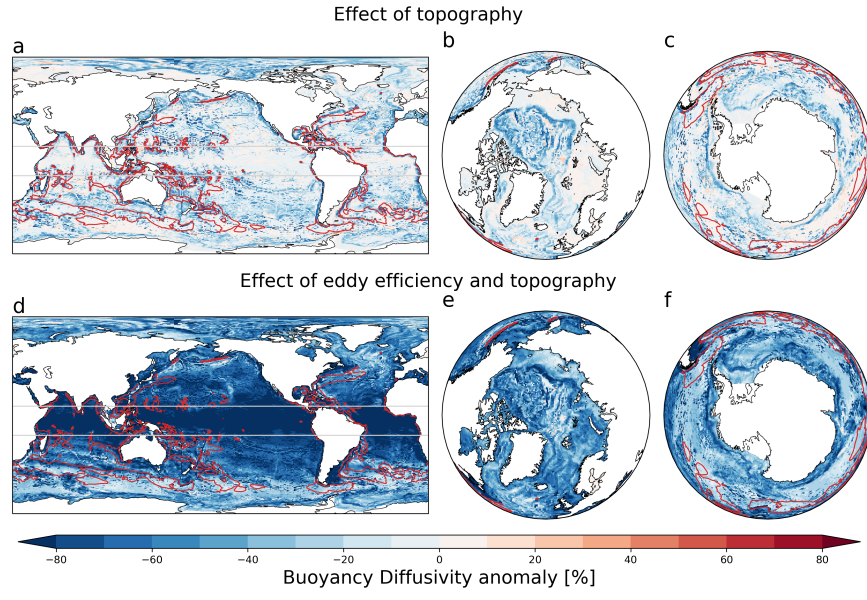
Abstract

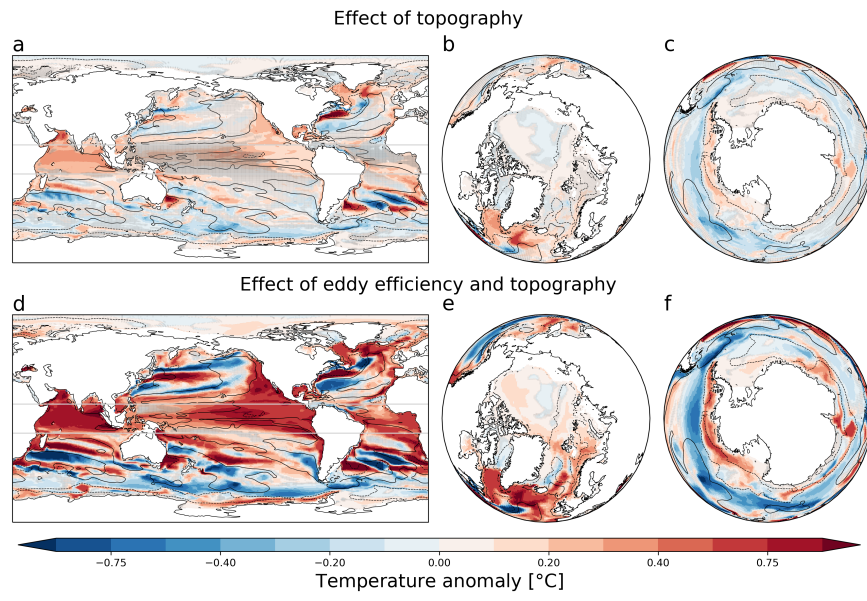
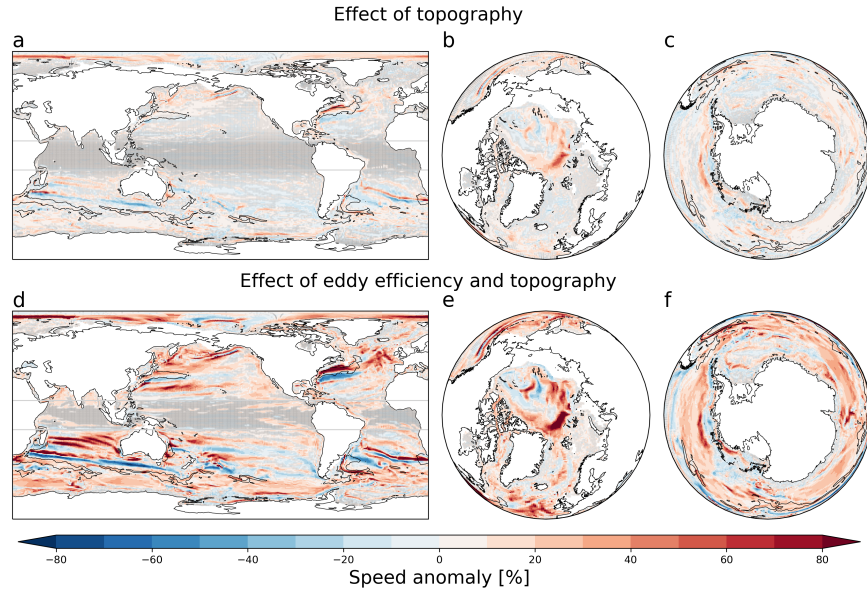
Most of the ocean's kinetic energy is contained within the mesoscale eddy field. Models that do not resolve these eddies tend to parameterize their impacts through down-gradient transport of buoyancy and tracers, aiming to reduce the large-scale available potential energy and spread tracers. However, the parameterizations used in the ocean components of current generation Earth System Models (ESMs) rely on an assumption of a flat ocean floor even though observations and high-resolution modelling show that eddy transport is sensitive to the potential vorticity gradients associated with a sloping sea floor. We show that buoyancy diffusivity diagnosed from idealized eddy-resolving simulations is indeed reduced over both prograde and retrograde bottom slopes (topographic wave propagation along or against the mean flow, respectively) and that the reduction can be skilfully captured by mixing length parameterization by introducing the topographic Rhines scale as a length scale. This modified 'GM' parameterization enhances the strength of thermal wind currents over the slopes in coarse-resolution, non-eddy, simulations. We find that in realistic global coarse-resolution simulations the impact of topography is most pronounced at high latitudes, enhancing the mean flow strength and reducing temperature and salinity biases. Reducing buoyancy diffusivities further with a mean-flow dependent eddy efficiency factor has notable effects also at lower latitudes and leads to reduction of global mean biases.

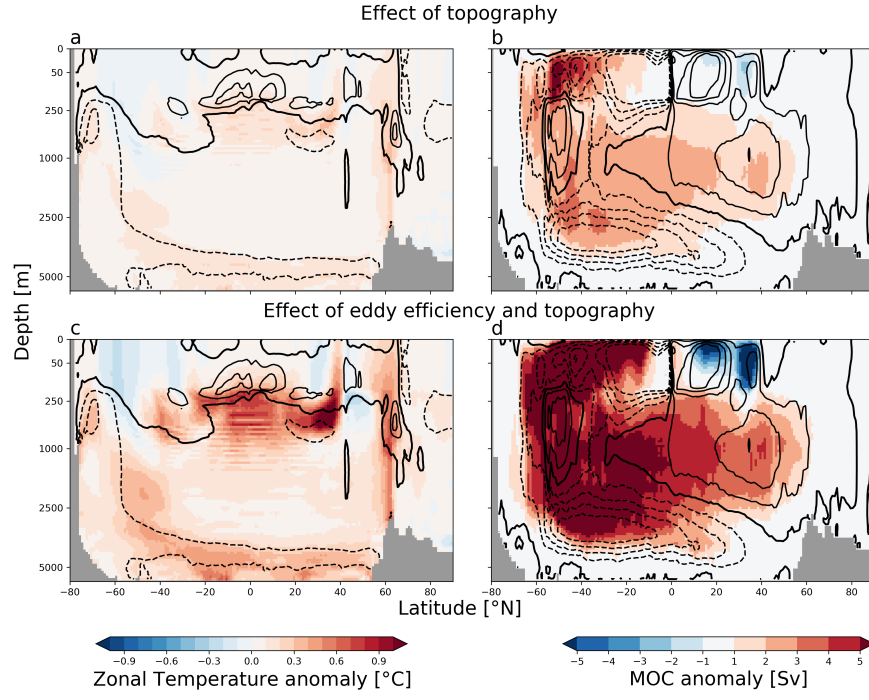












1 **Parameterizing mesoscale eddy buoyancy transport**
2 **over sloping topography**

3 **Aleksi Nummelin^{1,2,3}, Pål Erik Isachsen^{1,4}**

4 ¹University of Oslo, Department of Geosciences, Oslo, Norway

5 ²NORCE Norwegian Research Centre AS and Bjerknes Centre for Climate Research, Bergen, Norway

6 ³Finnish Meteorological Institute, Helsinki, Finland

7 ⁴Norwegian Meteorological Institute, Oslo, Norway

8 **Key Points:**

- 9 • Eddy buoyancy diffusivity reduction over bottom slopes can be parameterized using the Eady growth rate and topographic Rhines scale.
10 • Realistic reduction in buoyancy diffusivity in a coarse resolution model enhances baroclinic boundary currents.
11 • A topographically-aware eddy efficiency factor improves the parameterization and
12 further reduces biases in global simulations.
13
14

Abstract

Most of the ocean’s kinetic energy is contained within the mesoscale eddy field. Models that do not resolve these eddies tend to parameterize their impacts through down-gradient transport of buoyancy and tracers, aiming to reduce the large-scale available potential energy and spread tracers. However, the parameterizations used in the ocean components of current generation Earth System Models (ESMs) rely on an assumption of a flat ocean floor even though observations and high-resolution modelling show that eddy transport is sensitive to the potential vorticity gradients associated with a sloping sea floor. We show that buoyancy diffusivity diagnosed from idealized eddy-resolving simulations is indeed reduced over both prograde and retrograde bottom slopes (topographic wave propagation along or against the mean flow, respectively) and that the reduction can be skilfully captured by mixing length parameterization by introducing the topographic Rhines scale as a length scale. This modified ‘GM’ parameterization enhances the strength of thermal wind currents over the slopes in coarse-resolution, non-eddying, simulations. We find that in realistic global coarse-resolution simulations the impact of topography is most pronounced at high latitudes, enhancing the mean flow strength and reducing temperature and salinity biases. Reducing buoyancy diffusivities further with a mean-flow dependent eddy efficiency factor has notable effects also at lower latitudes and leads to reduction of global mean biases.

Plain Language Summary

Due to their high computational costs, global climate models are usually run at coarse spatial resolution, which does not allow them to resolve the ocean weather—mesoscale eddies—which are an important part of the ocean energy cycle and contribute to mixing of tracers such as heat and carbon. Eddies are instead parameterized in an idealized manner which relates the eddy-driven transport to the strength of the vertical and horizontal density gradients in the ocean. Such parameterization do not take into account impacts of large-scale bottom bathymetry which have been shown to weaken the eddy driven transport. Here we use high-resolution eddy-resolving simulations to improve existing parameterizations so that they become sensitive to the bottom slope. We show that such a parameterization qualitatively captures the transport reduction seen in idealized high-resolution simulations and can also reduce errors in realistic global simulations.

1 Introduction

At present, the ocean components of most global climate models are used at resolutions that require parameterizing the oceanic mesoscale (Fox-Kemper et al., 2019). And although coupled simulations with eddy ocean fields are slowly emerging (Chang et al., 2020), mesoscale eddy parameterizations are still likely part of ocean models for another decade. Most present-day parameterizations have their origins in the works of Gent and McWilliams (1990); Gent et al. (1995) and Redi (1982), tackling eddy-induced advection and tracer mixing, respectively. The ‘GM’ advection is cast in terms of a horizontally down-gradient and vertically up-gradient buoyancy diffusion which acts to reduce available potential energy. And ‘Redi’ diffusion mixes tracers down-gradient along isopycnals (Gent, 2011). In practice, most model implementations focus on estimating an eddy diffusion coefficient, or eddy diffusivity, which is then used to drive both eddy induced advection and mixing. It is generally understood that these are separate processes. However, previous studies have suggested that GM and Redi coefficients differ only in their vertical structure (K. S. Smith & Marshall, 2009; Abernathey et al., 2013; Bachman et al., 2020) and, therefore, that their depth-averaged values should be similar up to a constant factor.

64 Depth-averaged eddy diffusion coefficients in coarse-resolution climate models are
 65 often parameterized following mixing length theory, set proportional to the product of
 66 some eddy velocity scale and a mixing length scale. Some work has gone into estimat-
 67 ing the eddy velocity scale by implementing a prognostic equation for eddy energy (Eden
 68 & Greatbatch, 2008; Marshall et al., 2012; Mak et al., 2018; Bachman, 2019; Jansen et
 69 al., 2019), but this is still very much an active field of research. The study by Visbeck
 70 et al. (1997) therefore continues to influence the practical use of the mixing length ap-
 71 proach. Drawing on earlier works by Green (1970) and Stone (1972), the authors pro-
 72 posed that the velocity scale be based on the product of the growth rate of baroclinic
 73 instability in the linearized Eady model (Eady, 1949) and some length scale. Assuming
 74 that the mixing length is also set by the same scale, the diffusivity will then scale as the
 75 Eady growth rate and the square of the length scale. Visbeck et al. (1997) associated
 76 the mixing length with the 'width of the baroclinic zone' which they defined as "the width
 77 of the region where the local growth rate exceeds 10% of the maximum growth rate of
 78 the field". The concept, however, is hard to define in any but the the most idealized model
 79 geometries, and length scales therefore need to be formed from theoretical dynamical ar-
 80 guments.

81 As proposed by Stone (1972), one obvious candidate for length scale is the internal
 82 deformation radius, the approximate scale of fastest unstable growth in the Eady model.
 83 Solid observational evidence for the relevance of this length scale has been presented by
 84 Stammer (1997) and Eden (2007). However, other relevant scales arise if dynamics be-
 85 yond the Eady framework is accounted for, most notably bottom friction and internal
 86 potential vorticity (PV) gradients. Jansen et al. (2015), for example, examined the role
 87 of bottom friction and the planetary vorticity gradient in a two-layer flat-bottom chan-
 88 nel model. They found that bottom friction primarily influences the vertical distribu-
 89 tion of eddy energy and that the mixing length in most of their simulations is set by the
 90 Rhines scale, i.e. the transition scale between nonlinear and linear PV dynamics on the
 91 flat-bottom planetary beta plane (Rhines, 1977). More generally, Jansen et al. (2015)
 92 found that in order to cover various dynamical regimes, the smaller of several candidate
 93 length scales should be chosen. And, in fact, the observational studies of both Stammer
 94 (1997) and Eden (2007) specifically pointed to a minimum of the internal deformation
 95 radius and the Rhines scale as a best fit for eddy length scales over much of the world
 96 oceans.

97 These principles remain the standard in state-of-the-art models, although devel-
 98 opment has occurred in later years. As mentioned above, there has been extensive fo-
 99 cus on developing prognostic equations for eddy energy. And a considerable effort has
 100 gone into studying effects of horizontal eddy anisotropy (R. D. Smith & Gent, 2004) and
 101 the suppression of mixing across strong mean flows (Ferrari & Nikurashin, 2010; Klocker
 102 et al., 2012, and references therein). It's worth noting, however, that most of the devel-
 103 opment up until recently has been guided by observed dynamics in low- and mid-latitudes.
 104 Current parameterizations thus lack any treatment of two aspects that are potentially
 105 of huge importance in high latitude oceans, namely the presence of sea ice and the po-
 106 tential vorticity gradients imposed by sloping bottom topography. A sea ice cover can
 107 effectively have the same influence as bottom friction on both growth of baroclinic in-
 108 stability as well as dissipation of existing mesoscale and sub-mesoscale eddies (Meneghello
 109 et al., 2021). But this topic will be left out from the present study. We will instead fo-
 110 cus on the dynamical impacts of bottom slopes, i.e. continental slopes and mid-ocean
 111 ridge systems, whose imprints can be easily seen in observations of both mean currents
 112 and mesoscale energy fields, especially at high northern latitudes (Nøst & Isachsen, 2003;
 113 Koszalka et al., 2011; Trodahl & Isachsen, 2018). Such imprints of topographic PV gra-
 114 dients can also be seen at lower latitudes, e.g. in drifter and float paths (LaCasce, 2000;
 115 Fratantoni, 2001).

116 Sloping bottom topography can suppress growth rate and reduce length scales of
 117 baroclinic instability (e.g. Blumsack & Gierasch, 1972; Mechoso, 1980; Isachsen, 2011;
 118 Brink, 2012) as well as impact finite-amplitude eddy fields (e.g. Bretherton & Haidvogel,
 119 1976; Vallis & Maltrud, 1993; Lacasse & Brink, 2000; K. Stewart et al., 2015; Wang
 120 & Stewart, 2018). To this end, new topography-aware parameterizations have started
 121 to emerge, both for eddy-induced advection and isopycnal mixing. In particular, Wang
 122 and Stewart (2020) and Wei et al. (2022) used high-resolution model simulations of flows
 123 over idealized continental slopes in a re-entrant channel to test different scaling relations
 124 for the GM diffusivity. The two works examined eddy characteristics and fluxes across
 125 retrograde and prograde mean currents, respectively, meaning currents that are in the
 126 opposite and same direction as topographic waves. Both studies diagnosed the eddy en-
 127 ergy from the high-resolution fields and used this to examine traditional mixing length
 128 formulations in addition to the 'GEOMETRIC' formulation of Marshall et al. (2012) which
 129 is based on eddy energy and the inverse of the Eady growth rate. In general, the two for-
 130 mulations performed similarly, suggesting that a good knowledge of the eddy energy field
 131 is key. But, importantly, both studies also found that empirical prefactors that depend
 132 on the topographic slope are needed to reproduce the very weak eddy buoyancy fluxes
 133 across sloping bottom topography.

134 Wei and Wang (2021) carried on from Wang and Stewart (2020), but focused on
 135 the along-isopycnal tracer (Redi) diffusivity—in retrograde flows only. The authors scaled
 136 the Redi diffusivity from (the square root of) the diagnosed eddy kinetic energy and the
 137 internal deformation radius. But here too it was found that the effective diffusivity over
 138 the slope was suppressed below the original scale estimate. However, instead of testing
 139 a set of empirical slope-dependent prefactors, as done by Wang and Stewart (2020) and
 140 Wei et al. (2022), this study picked up from Ferrari and Nikurashin (2010) and argued
 141 that mean flow suppression could explain the observed reduction in cross-slope fluxes near
 142 the surface, whereas eddy velocity anisotropy contributed to the reduction close to the
 143 bottom.

144 In other words, both sets of studies (see also Brink, 2012, 2016; Hetland, 2017) con-
 145 cluded that the strength of eddy fluxes over sloping bottoms is not only given by eddy
 146 energy and length (or time) scales but also by additional dynamical impacts of the bot-
 147 tom topography. Essentially, perfect knowledge of the eddy energy and either length scales
 148 or time scales will only produce an upper bound on eddy diffusivity. Eddy velocity anisotropy
 149 is one obvious factor which may then bring the diffusivity down from this upper bound.
 150 The other and perhaps more important factor is the possibility that velocity and tracer
 151 perturbations are not very well in phase (the two being in quadrature would give zero
 152 transport). Most likely, the topography-dependent prefactors of the above-mentioned stud-
 153 ies primarily address such imperfect phase relationships.

154 The present study will focus on eddy buoyancy transport and thus on GM diffu-
 155 sivities. It is inspired by and builds directly on the results obtained by Wang and Stew-
 156 art (2020) and Wei et al. (2022). However, as noted, the above works examined prograde
 157 and retrograde flows separately and also constructed diffusivities from eddy energy lev-
 158 els diagnosed from very idealized but high-resolution fields. So here we aim to i) study
 159 fluxes and diffusivities over both types of flow situations under one and the same frame-
 160 work, ii) examine how far one can get without diagnosing the actual eddy energy field
 161 and, finally, iii) assess the impacts both in an idealized setting and in a realistic global
 162 ocean simulation.

163 In the process, we also revisit the question of what is the relevant eddy length scale
 164 over continental slopes. The starting point will be the internal deformation radius since
 165 this remains a relevant parameter in the Eady problem, even when this includes a bot-
 166 tom slope (Blumsack & Gierasch, 1972). But we also consider the topographic Rhines
 167 scale, i.e. the scale where topographic Rossby waves (rather than planetary Rossby waves)
 168 mark the transition between linear and non-linear PV dynamics. The above-mentioned

169 idealized channel studies give conflicting evidence about the relevance of this scale. We
 170 are nevertheless inspired by the findings of Stammer (1997), Eden (2007) and Jansen et
 171 al. (2015) and therefore bring up this approach here again. Finally, we also examine and
 172 attempt to parameterize the role of eddy velocity anisotropy and the phase relationship
 173 between flow and buoyancy perturbations.

174 The paper is structured as follows: In section 2 we introduce the modelling tools
 175 and various diagnostics and parameterizations used. In section 3 we begin by diagnos-
 176 ing eddy fields from a high-resolution channel simulations that contain both prograde
 177 and a retrograde flows at the same time. We then see how far mixing-length and GE-
 178 OMETRIC parameterizations can take us in reproducing the diagnosed depth-averaged
 179 GM diffusivity—with and without accounting for effect of anisotropy and phase relations
 180 between eddy velocity and tracer perturbations. At the end of this section we examine
 181 the impact of a topographically-aware parameterization in a coarse-resolution version
 182 of the channel model. In section 4 we finally employ the new parameterization in real-
 183 istic global ocean simulation. We then take a critical look into some of our parameter-
 184 ization choices and their interpretation in section 5 before summarizing our findings in
 185 section 6.

186 2 Methods

187 2.1 Model setup

188 We use the Bergen Layered Ocean Model (BLOM), the ocean component of the
 189 Norwegian Earth System Model (NorESM; Seland et al., 2020), in an idealized channel
 190 configuration as well as in a realistic global setup. BLOM uses 51 isopycnal levels (po-
 191 tential density referenced to 2000 dbar) with a 2-level bulk mixed layer at the surface.

192 The channel setup is re-entrant in the zonal (x) direction. The domain is 416 km
 193 long (zonally) and 1024 km wide (meridionally). At both sides of the channel there are
 194 continental slopes centered at 150 km from the domain edge, stretching 2000 m in ver-
 195 tical from the shelf break at 250 m depth to the bottom of the slope at 2250 m depth.
 196 In addition, to trigger instabilities we add random noise with standard deviation of 10 m
 197 to the bottom topography. The model is initialized from rest with constant salinity and
 198 a horizontally homogeneous temperature profile. The temperature, which here determines
 199 density alone, has a maximum at the surface and decays exponentially towards the bot-
 200 tom. We place the channel in the northern hemisphere, using a constant Coriolis param-
 201 eter, and then force the flow with a constant westward wind stress. The surface mixed
 202 layer is kept shallow by parameterization of submesoscale mixed layer eddies (Fox-Kemper
 203 et al., 2008) that counter the vertical mixing induced by the constant wind forcing. See
 204 Table 1 for further parameter settings.

205 We first run the channel model at eddy-resolving 2 km horizontal resolution. To
 206 investigate the effects of the two bottom slopes on eddy transport and, specifically, on
 207 eddy diffusivity, we vary the initial stratification and the width of the continental slope,
 208 i.e the slope angle. The various experiments are laid out in Table 2. All simulations are
 209 spun-up to a semi-equilibrium for 10 years, and the model fields are then diagnosed over
 210 an additional 5-year period (so between years 10–15). We then test and compare var-
 211 ious forms of parameterized eddy buoyancy fluxes at coarse resolution at 32 km resolu-
 212 tion in the same idealized channel. These are also run for 15 years, with the last 5 years
 213 being diagnosed.

214 Finally, the impact of the most skillful parameterization is assessed in realistic global
 215 simulations. These are nominal 1° resolution global forced ocean-ice experiments which
 216 follow the Ocean Model Intercomparison Project, OMIP-II protocol (Tsujino et al., 2020).
 217 In these simulations, the mean grid size north of 62°N and south of 64.5°S is approx-
 218 imately 32 km, similar to the coarse resolution channel. Two simulations are conducted,

219 one with the new parameterization and another with an existing eddy parameterization
 220 which does not include any effects of bottom topography. Each simulation is 110 year
 221 long (2 cycles of 55 long repeat cycle), and we diagnose the results using the last 30 years.
 222 At this point there is still a long term drift in the model (as seen in all models follow-
 223 ing the OMIP-II protocol; Tsujino et al., 2020), but the general circulation has stabi-
 224 lized.

225 **2.2 Diagnostics and Paramaterizations**

The key parameter of interest is the buoyancy diffusivity, as we have assumed that lateral eddy buoyancy transport can be expressed as down-gradient diffusion. In the idealized zonal channel simulations, where buoyancy is given by temperature, the cross-channel (i.e. meridional) buoyancy diffusivity can be diagnosed from

$$K_{diag} = -\frac{\langle v'T' \rangle}{\partial \langle T \rangle / \partial y}, \quad (1)$$

226 where v and T are meridional velocity and temperature, respectively. Angle brackets indi-
 227 cate a zonal (along-channel) mean and primes indicate deviations from such mean. So
 228 v' and T' are the across-channel velocity and temperature perturbations from the zonal
 229 mean.

Note that the cross-channel perturbation velocity is related to the eddy kinetic energy density

$$EKE = \frac{\langle u'^2 \rangle + \langle v'^2 \rangle}{2} \quad (2)$$

via the velocity anisotropy factor

$$A = \frac{\langle v'^2 \rangle}{\langle u'^2 \rangle + \langle v'^2 \rangle}, \quad (3)$$

so that

$$v' = (2A \cdot EKE)^{1/2}. \quad (4)$$

In practice, we use Parseval's theorem to diagnose the buoyancy flux from the cross spectrum of cross-channel velocity and temperature:

$$K_{diag} = \frac{\int \hat{C}o(v', T') dk}{\partial \langle T \rangle / \partial y}, \quad (5)$$

230 where $\hat{C}o(v', T')$ is the real part of the cross spectrum which we integrate over all zonal
 231 wavenumbers k .

232 In this study we focus exclusively on the depth-averaged diffusivity, and if not stated
 233 otherwise all variables are depth-averaged quantities. We leave the development of depth-
 234 varying parameterizations for future studies. A fruitful way forward for this may be to
 235 develop a flow-dependent structure function that distributes the depth-averaged diffu-
 236 sivity vertically (see e.g. Bachman et al., 2020; Wei & Wang, 2021). Finally, for anal-
 237 ysis of the channel simulations, we also average K_{diag} over time.

Parameterizing the diffusivity starts with a scale estimate. Two approaches are currently in use, the traditional mixing length and the GEOMETRIC approach. In the former, we write

$$K_{ML} \propto VL, \quad (6)$$

where V is a representative eddy velocity and L is a lateral mixing scale. Typically, this is often taken to be related to the size of eddies themselves. If complete information exists about the high-resolution eddy fields, it is natural to set $V = \sqrt{EKE}$ or, more correctly for the cross-channel diffusion we study here, $V = \langle v' \rangle$. The eddy length scale

L may also be diagnosed from the shape of velocity spectra. Several possibilities exist (see e.g. Eden, 2007), but here we chose

$$L_S = \frac{\int |\hat{v}(k)|^2 k^{-1} dk}{\int |\hat{v}(k)|^2 dk} \quad (7)$$

238 which can be thought of as a kinetic energy-weighted mean wavelength under the spec-
239 trum.

Alternatively, the energy-based diffusivity estimate of the GEOMETRIC frame-
work (Marshall et al., 2012; Mak et al., 2018) is constructed as

$$K_{GEOM} \propto \sigma_E^{-1} E, \quad (8)$$

where σ_E is the Eady growth rate and E is the total eddy energy. The Eady growth rate is

$$\sigma_E = 0.3 \frac{f}{Ri^{1/2}} \quad (9)$$

where f is the Coriolis parameter and Ri is the geostrophic Richardson number:

$$Ri = \frac{N^2}{|\partial U_g / \partial z|^2}. \quad (10)$$

Here

$$\begin{aligned} N^2 &= -\frac{g}{\rho_0} \frac{\partial \rho}{\partial z} \\ &= \partial b / \partial z \end{aligned} \quad (11)$$

is the squared buoyancy frequency (g is gravitational acceleration, ρ is density and b buoyancy, while ρ_0 is a reference density) and

$$\begin{aligned} |\partial U_g / \partial z| &= \left| \frac{g}{\rho_0 f} \nabla \rho \right| \\ &= |\nabla b / f| \end{aligned} \quad (12)$$

is the magnitude of the thermal wind shear. As said, E is the total eddy energy, i.e. the sum of the EKE and EPE (eddy potential energy). The latter is diagnosed from

$$EPE = \frac{1}{H} \sum_{i=1,n} \frac{1}{2} \frac{\rho_{i+1} - \rho_i}{\rho_0} g \langle \eta_{i+1/2}^2 \rangle, \quad (13)$$

240 where η is the height of an isopycnal surface (trivially diagnosed from the layered BLOM
241 model). The sum is taken over n density surfaces and, as in all of the above, the prime
242 marks deviations from the zonal mean.

Since the work on prognostic eddy energy budgets is still a topic of active research, we set out here to parameterize both the eddy velocity and eddy length scale from coarse-resolution variables. Thus, following Visbeck et al. (1997), we write

$$V_{par} = \sigma_E L, \quad (14)$$

which gives

$$K_{par} \propto \sigma_E L^2. \quad (15)$$

Two parameterizations for the eddy length scale are then assessed, namely the WKB-approximation to the internal Rossby deformation radius

$$L_R = \frac{\int N dz}{|f|}, \quad (16)$$

and the parameterized version of the topographic Rhines scale

$$L_T = \left(\frac{V_{par}}{\beta_T} \right)^{1/2} = \frac{\sigma_E}{\beta_T}, \quad (17)$$

243 where $\beta_T = (|f|/H)|\nabla H|$ and we have assumed $V_{par} = \sigma_E L_T$ (Eden & Greatbatch,
 244 2008). Parameterized velocity and length scales are always chosen consistently i.e. the
 245 parameterized diffusivities will depend on the Eady growth rate and the squared length
 246 scale of choice.

Finally, as outlined in the introductory section, it is important to remember that
 the above parameterizations most likely give upper bounds on diffusivities, correspond-
 ing to situations where there is perfect correlation between the eddy velocity and tem-
 perature perturbations, i.e. where the two quantities are either in perfect phase or anti-
 phase. To investigate if and how topographic slopes impact such phase relationship, we
 also utilize the high-resolution fields from the channel simulation to map out the cosine
 of the phase angle between the real and imaginary parts of the cross spectrum between
 v' and T' :

$$\cos(\theta) = \frac{\hat{C}o(v, T)}{\left[\hat{C}o(v, T)^2 + \hat{Q}u(v, T)^2 \right]^{1/2}} \quad (18)$$

247 where $\hat{Q}u(v, T)$ is the the imaginary part of the cross spectrum (the quadrature spec-
 248 trum). For analysis, we average θ across all wavenumbers (k) and over time before cal-
 249 culating the cosine. An attempt to parameterize the observed phase relationship is also
 250 presented in what follows.

251 3 Eddy fluxes in a channel model

252 3.1 Equillibrated flow field and eddy fluxes

253 Our setup (see section 2.1) is very similar to the setup in the series of papers by
 254 Wang and Stewart (2018, 2020), Wei and Wang (2021) and Wei et al. (2022), except that
 255 we now have continental slopes on both sides of the channel. The forcing is also slightly
 256 different as we employ a westward wind stress which, unlike in the previous studies, is
 257 kept constant across the channel. The mean ocean state, however, is very similar. Since
 258 the channel is in the northern hemisphere, the westward wind stress sets up a northward
 259 surface Ekman transport. Thus, Ekman divergence in the south and convergence in the
 260 north results in a time-mean sea surface tilt which is in geostrophic balance with a west-
 261 ward mean flow, as shown in the two upper panels of Figure 1. The Ekman-driven over-
 262 turning circulation in the y - z plane lifts up isopycnals in the south so that they slope with
 263 the bathymetry there. Conversely, downwelling in the north sets up isopycnals that slope
 264 against the topography.

265 Despite the simple wind forcing, the total baroclinic velocity field is rather com-
 266 plex. In the north there is a strong westward jet over the slope. This jet has a signifi-
 267 cant thermal wind shear but nonetheless extends all the way to the bottom. Over the
 268 southern slope the westward flow is weaker and much more surface-trapped. Lower lay-
 269 ers here are almost motionless, so the depth-averaged westward flow takes on a minimum
 270 over the slope. Instead there is a broad and nearly barotropic westward current which
 271 has its maximum strength immediately off the seaward side of the continental slope.

The north-south asymmetry is clearly not only a result of the stratification being
 weaker in the south than in the north. Thus, net impacts of mesoscale eddy fluxes must
 likely be taken into account. At the most basic level, the tilted isopycnals in both regions
 are baroclinically unstable, creating an eddy field whose residual mass transport will tend

to counter the Ekman-driven overturning circulation. However, because mesoscale eddies also transport momentum, the mean flow field reflects, in part, the integrated effects of eddy momentum and buoyancy fluxes. Their combined effects can be studied in the Transformed Eulerian Mean (TEM) version of the zonally-averaged zonal momentum equation:

$$\frac{\partial \langle u \rangle}{\partial t} - f \langle v^* \rangle = -\nabla_{yz} \cdot \mathbf{F}_{EP} + \frac{\partial \langle \tau^x \rangle}{\partial z}, \quad (19)$$

where

$$\mathbf{F}_{EP} = -\langle v'u' \rangle \hat{\mathbf{j}} + f \frac{\langle v'b' \rangle}{N^2} \hat{\mathbf{k}} \quad (20)$$

272 is the Eliassen-Palm flux. It consists of a lateral eddy momentum flux and an eddy form
 273 stress (this term arises after thickness-weighting). In (19) we have neglected small terms
 274 describing the transport of zonal mean momentum by the meridional mean flow as well
 275 as vertical flux of momentum (see Wang & Stewart, 2018). Note, however, that the eddy
 276 form stress term, which is connected to lateral buoyancy transport under the small-slope
 277 approximation, may be thought of as a vertical momentum flux. Finally, the Coriolis term
 278 contains the *residual* meridional velocity, i.e. the equivalent mass transport velocity which
 279 accounts for both the Eulerian-mean flow and the mass transport by eddy correlations.

280 The E-P flux is shown as arrows in the top panel of Figure 1. In general, both in
 281 the south and in the north, the downward eddy momentum flux is suppressed over the
 282 slopes, in agreement with earlier studies which indicate that baroclinic instability of sup-
 283 pressed over continental slopes. Our estimate of the depth-averaged cross-channel buoy-
 284 ancy diffusivity reflects this signature by being reduced by about two orders of magni-
 285 tude over the continental slopes (lower panel). What these simulations show, as also seen
 286 in the simulations of Wang and Stewart (2018) and Manucharyan and Isachsen (2019),
 287 is that eddy motions instead bring zonal momentum laterally across the slopes near the
 288 surface and dump it where the ocean bottom flattens off towards the deep basin (this
 289 lateral component $\langle v'u' \rangle$ is highlighted with color in the plot). And there, over the
 290 relatively flat bottom, baroclinic instability kicks in to bring the momentum down to the
 291 solid ground below.

292 As lateral eddy momentum fluxes are also clearly important in this and previous
 293 simulations, optimal parameterizations will likely need to be build up around down-gradient
 294 PV fluxes (see e.g. Wang & Stewart, 2018). However, it is also reasonable to expect that
 295 any framework which is successful at reproducing the order-of-magnitude drop in buoy-
 296 ancy diffusivities seen in Figure 1 will also improve the ocean state in coarse-grained mod-
 297 els. So we keep this focus here. Hence, on our way towards a practical parameterization
 298 of a GM diffusivity over continental slopes, we begin by examining the length scales and
 299 velocity scales associated with the mesoscale eddy field. This approach is motivated by
 300 the mixing length argument (Prandtl, 1925), relating diffusivity to an eddy velocity scale
 301 and a length scale. However, we will also compare this approach with the energy-based
 302 GEOMETRIC framework (Marshall et al., 2012; Mak et al., 2018).

303 3.2 Eddy length and velocity scales

304 Estimates of eddy length and velocity scales are shown in Figure 2. The length scale
 305 is estimated from (7), i.e. by calculating a spectral-weighted mean wavelength associated
 306 with north-south velocity perturbations. When normalized by its mean value across the
 307 channel the length scale shows a near-universal shape across the various model runs (up-
 308 per left panel). There is a broad maximum over the mid-basin before length scales drop
 309 over the continental slopes on both sides. There is, however, a consistent local maximum
 310 over mid-slope on the northern (prograde) side, coinciding with the maximum in mean
 311 zonal velocity. Scales then flatten out or even increase over the shelf regions. But, as with
 312 other diagnostics below, but we will largely ignore shelf values in the discussion below
 313 due to the proximity to the model walls. For the eddy velocity scale we show the square
 314 root of EKE. When normalized with the across-channel average (upper right panel), the

315 eddy velocity scale in all runs is reduced over the southern slope, save for a slight increase
 316 over the upper parts of the slope. In stark contrast, the northern slope is dominated
 317 by a large maximum, also that one centered over the upper parts of the slope. The eddy
 318 velocity then drops off and flattens out over both shelf regions.

319 It would seem that forming a diffusivity from the product of these diagnosed length
 320 and velocity scales may reproduce the observed reduction over the southern retrograde
 321 slope (Fig. 1), at least qualitatively. But it should also be clear that the same procedure
 322 would produce a diffusivity maximum over the northern slope—for which there is ab-
 323 solutely no indication in the model fields. We will return to this issue below but first ex-
 324 amine possible scaling approximations to the observed length and velocity scales.

325 We start by normalizing by the classical Stone (1972) prediction. So the length scale
 326 is normalized by the internal deformation radius L_R (16) and the velocity scale by the
 327 product of the Eady growth rate (9) and the deformation radius, so $V = \sigma_E L_R$. With
 328 such normalization both the length scales and velocity scales collapse really well in the
 329 mid-basin (middle panels). The normalized length scales then drop slightly over the lower
 330 parts of both slopes, indicating that the deformation radius overestimates scales there
 331 somewhat. Finally, there is a dramatic rise in normalized scales over the upper parts of
 332 both slopes as the deformation radius drops towards the shallow shelves. As with length
 333 scales, the normalized velocities drop over the lower parts of the slopes before rising again
 334 over the upper parts. The normalization brings the EKE peak over the upper parts of
 335 the slope down to values similar to those seen over the mid-basin, suggesting that the
 336 EKE peak there coincides with the region of active baroclinic instability.

Finally, we normalize by selecting a smooth minimum of length scales:

$$L_{min} = \frac{L_R L_T}{L_R + L_T}, \quad (21)$$

337 where L_T is the topographic Rhines scale (17). The results are similar over the central
 338 basin since the deformation radius is the smaller of the two scales there (the Rhines scale
 339 blows up). But now both normalized length and velocity scales peak over the slopes where
 340 the Rhines scale becomes the smaller of the two—and is quite clearly too small to ex-
 341 plain the observed fields. As such, consideration of the topographic Rhines scale does
 342 not seem to bring any improvement in skill over the continental slopes.

343 But before rejecting this scaling choice it is worth noting again that the construc-
 344 tion of a diffusivity from the original (non-normalized) length and velocity scale estimates
 345 (i.e. from the curves shown in the top row) would obviously result in a diffusivity max-
 346 imum over the central northern slope. Such a maximum is in no way suggested from Fig-
 347 ure 1. What is missing from the story here is a consideration of how eddy velocity anisotropy
 348 and the velocity-temperature phase relationship may act to bring diffusivities down over
 349 the slopes. So we turn to this issue next.

350 3.3 Anisotropy and phase relationship

351 Figure 3 shows the eddy velocity anisotropy A (3) and the cosine of the phase angle
 352 between real and imaginary parts of the v' and T' cross-spectra (18). As expected,
 353 the eddy velocity field is close to being isotropic in the middle of the basin (upper panel).
 354 Values there are around 0.6, implying that cross-channel velocity fluctuations v' are in
 355 fact slightly larger than along-channel fluctuations u' . The eddy fluctuations then be-
 356 come much more anisotropic towards the continental slopes, with A values over the up-
 357 per parts of the slope close to 0.1 (0.2) in the north (south). This implies that v' is about
 358 70% (50%) smaller than u' in the north (south). A notable exception is a peak over the
 359 center of the northern slope where v' is about 50% larger than u' . We have also tested
 360 other measures of anisotropy, such as the velocity based measure used by K. Stewart et

361 al. (2015) that takes rotational aspects into account, and the results are similar to those
 362 shown here.

363 The general behavior of increased anisotropy over the slopes, with $|v'| < |u'|$, will
 364 work to reduce the scale-based diffusivity there. But the variations in A from mid-basin
 365 values are not great and the mid-slope peak (where $|v'| > |u'|$) would actually increase
 366 the estimates there. So we conclude from this that velocity anisotropy alone can not ex-
 367 plain the consistent drop in diffusivity by two orders of magnitude over the slopes seen
 368 in Figure 1. The phase relation, however, is able to explain the observed order-of-magnitude
 369 drop over the slopes, as the v' and T' fields are close to 90° out of phase there (middle
 370 panel). Importantly, the low phase agreement over the northern slope largely cancels the
 371 local peak in anisotropy.

372 The lower panel in Figure 3 shows the product of A and $\cos(\theta)$, an indication of
 373 the total suppression of diffusivities over the scale-based upper bound. The total sup-
 374 pression is dominated by the information carried in the phase relationship, and veloc-
 375 ity anisotropy primarily plays a role near the edges of the two slopes. The suppression
 376 over the slopes amounts to more than an order of magnitude, so it is an effect which clearly
 377 needs to be parameterized.

Essentially, the slope-dependent prefactors which previous studies have needed to
 invoke to explain buoyancy diffusion in similar channel simulations are attempts at such
 parameterization (Brink, 2012, 2016; Hetland, 2017; Wang & Stewart, 2020; Wei et al.,
 2022). However, at this point we temporarily detour from those earlier studies and in-
 stead take as a starting point an expression which bears some resemblance to the final
 form of the mean flow suppression expression proposed by Ferrari and Nikurashin (2010).
 Thus, we construct an eddy efficiency factor as

$$E_{eff} = a_1 \frac{1}{1 + a_2 (U_{bc}^2 / V^2)}. \quad (22)$$

378 Here, U_{bc} is the large-scale baroclinic flow speed obtained after subtracting the depth-
 379 averaged velocity, V is the eddy velocity scale and a_1 and a_2 are scaling factors which
 380 we here take to be constant. The expression does not have a rigorous basis but a sim-
 381 ple intuitive interpretation. U_{bc} is directly related to the thermal wind shear and, hence,
 382 to the underlying energy source of baroclinic instability (e.g. Sutyrin et al., 2021). Qual-
 383 itatively, if U_{bc} is large and the flow is baroclinically unstable, one would expect V to
 384 be relatively large, giving $E_{eff} \sim 1$. But if V remains small despite large U_{bc} , some dy-
 385 namical constraints (e.g. a sloping bottom) must be reducing the efficiency of baroclinic
 386 energy conversion, implying $E_{eff} \ll 1$.

387 We evaluate (22) at each depth but then take the mean over the water column. The
 388 large scale baroclinic flow U_{bc} is extracted directly from the resolved (and zonally-averaged)
 389 velocity field, while the eddy velocity is parameterized from (14). The lower panel of Fig-
 390 ure 3 shows the resulting efficiency factor, using either L_R or L_T as length scale. The
 391 tuning constants a_1 and a_2 have been chosen manually but it is clear that using $L =$
 392 L_T can produce a suppression over the continental slope which is in fairly good agree-
 393 ment with $A \cdot \cos(\theta)$ over both slopes for a range of different simulations. We note that
 394 several tests with using the thermal wind instead of U_{bc} and with evaluating (22) with
 395 depth averaged-quantities (instead of taking the mean of a depth dependent expression)
 396 all produce similar results. Here we chose to use U_{bc} due the ease of implementation at
 397 coarse resolution.

398 3.4 Parameterized diffusivity

399 Given the above results, we then proceed with parameterizing the diagnosed buoy-
 400 ancy diffusivity. The aim is to capture the order-of-magnitude reduction in diffusivities
 401 from the mid-basin to the slope regions. The results are shown in Figure 6 where we dis-

402 tinguish between diagnostic (panels a–c) and full parameterizations (panels d–e). The
 403 diagnostic parameterizations include information about the mesoscale field itself which
 404 would not be directly available in a coarse resolution model (but could be parameter-
 405 ized in higher-order schemes), whereas the full parameterizations use large-scale metrics
 406 only and are therefore suitable for direct implementation in any existing coarse-resolution
 407 model. Panels a and c are from one single simulation, showing both the actual depth-
 408 averaged diffusivity diagnosed (black line) and the various approximations (distinguished
 409 by Roman numerals and color). Panels b–c and e–f then show statistics over both slope
 410 regions collected over the whole range of simulations.

411 A first thing to notice from the diagnostic parameterizations (panels a–c) is that
 412 the mixing length (I) and GEOMETRIC (II) approaches behave very similarly. As also
 413 noted by Wang and Stewart (2020), both give reduced diffusivities over the southern ret-
 414 rograde slope and produce a reasonable fit there ($r^2 > 0.6$). But the reduction is still
 415 underestimated by up to one order of magnitude. In the north, over the prograde slope,
 416 both approaches result in a serious qualitative mismatch as the high EKE levels there
 417 (seen in Fig. 2) produce a non-existing diffusivity peak over mid-slope.

418 The observed discrepancies, particularly the qualitative mismatch over the north-
 419 ern slope, confirms that scaling arguments alone are unable to create diffusivities that
 420 reproduce the observed buoyancy transport across the slope regions. Accounting for the
 421 diagnosed eddy velocity anisotropy, so that $\sqrt{EK\bar{E}}$ will be replaced with v' (III) improves
 422 the mixing length estimate slightly but not nearly enough. Multiplying the two estimates
 423 by $A \cos \theta$, however, largely removes the diffusivity peak in the north and even produces
 424 a clear suppression over the slope (IV and V). The values are still higher than the ob-
 425 served diffusivity, but the regression slope is close to one and the correlation r^2 values
 426 above 0.8. Over the retrograde slope in the south the match is even higher.

Guided by the observed agreement between the mixing length and GEOMETRIC
 estimates above, we focus on the former approach when examining how well full para-
 meterizations can do. So we assume that a diffusivity can be written as the Eady growth
 rate times the square of a length scale. Including our efficiency factor, the effective dif-
 fusivity becomes

$$K = a_1 \frac{K_0}{1 + a_2 (U_{bc}^2/V^2)}, \quad (23)$$

427 where $K_0 = \sigma_E L^2$ is the scaling estimate of diffusivity before considering the efficiency
 428 factor and where, as discussed above, we have a choice to make for the length scale. We
 429 start by looking at K_0 first. Using the traditional Stone (1972) expression where the length
 430 scale is taken to be the internal deformation radius everywhere, seriously overestimates
 431 diffusivities over both slope regions (VI). The estimate, in fact, bears some resemblance
 432 with both the mixing length and GEOMETRIC estimates based on diagnosed eddy quan-
 433 tities (I and II), but with even larger discrepancies over the slope regions.

434 Selecting as length scale the smooth minimum of the deformation radius and the
 435 parameterized topographic Rhines scale (VII) improves the estimate dramatically. The
 436 results are unchanged over the flat regions, as the deformation radius is selected there.
 437 But over the slopes where the Rhines scale is selected, the parameterized diffusivities drop
 438 by up to two orders of magnitude and start to match the observations quite well (with
 439 $r^2 > 0.8$ over both slopes). Multiplying this estimate with the parameterized efficiency
 440 factor (VIII) improves the match somewhat over the prograde slope in the north but not,
 441 as it turns out, over the retrograde southern slope.

442 Both Figures 3 and 6 indicate that Stone scaling, i.e. using the deformation radius
 443 as length scale, produces better estimates of observed eddy characteristics than does the
 444 topographic Rhines scale. And yet, these simulations suggest that applying the Rhines
 445 scale is absolutely crucial in reproducing the observed diffusivity reduction over topo-
 446 graphic slopes. This apparent contradiction may suggest that our parameterized topo-

447 graphic Rhines scale does not reflect the physical size of equilibrated eddies but rather
 448 a reduction in the effective mixing length. In other words, the mixing length is not triv-
 449 ially related to the eddy size. Given our parameterization, the effect will impact the scal-
 450 ing estimate significantly so that the need for an explicit suppression factor (our E_{eff})
 451 becomes smaller. But we leave further speculation on this topic to the discussion sec-
 452 tion and here carry on to see what effects the parameterized expression (VIII) will have
 453 in actual coarse-grained simulations.

454 3.5 Performance in a coarse-resolution channel simulation

455 The coarse-resolution channel setup is similar to the high-resolution channel setup,
 456 except for resolution (from 2 km to 32 km) and the activation of the GM-Redi param-
 457 eterization scheme. The model is forced and run similarly to the high-resolution setup.
 458 Figure 5 shows parameterized buoyancy diffusivities and the top-to-bottom thermal wind
 459 shear from three of the equilibrated simulations that had wide continental slopes but
 460 differing initial stratification. We also show the corresponding diagnosed quantities from
 461 the corresponding high-resolution simulations for comparison (thick black lines), but it
 462 should be remembered that that one is a distinct simulation. As in Figure 6, we show
 463 the three versions of the parameterized diffusivity (and corresponding thermal wind shears):
 464 one using the internal deformation scale (with $a_1 = 8$), one using the smooth minimum
 465 between internal deformation scale and topographic Rhines scale (with $a_1 = 8$) and,
 466 finally, one using the smooth minimum and also applying the parameterized eddy effi-
 467 ciency factor (with $a_1 = 32$ and $a_2 = 1$). In the last case a_1 is tuned so that the pa-
 468 rameterized buoyancy diffusivity matches the two former cases in the mid-basin.

469 The results show that over the mid-basin, where the internal Rossby radius will al-
 470 ways be selected as length scale, the parameterized diffusivity magnitude corresponds
 471 fairly well to the diagnosed diffusivity in the mid-basin. However, the parameterized dif-
 472 fusivity shows a clear north-south gradient in the magnitude, an effect caused by a stronger
 473 difference in stratification between north and south at coarse resolution which directly
 474 impacts the internal deformation radius. The deformation scale-based parameterization
 475 (orange line) then suggests local diffusivity maxima over both slopes, as also seen in Fig-
 476 ure 6. This run has a thermal wind shear which is not at all enhanced over the conti-
 477 nental slopes. Essentially, the high eddy buoyancy transport over the slope regions ef-
 478 fectively washes out any density front there. This, it should be remembered, is exactly
 479 the effect one wishes to reduce with a slope-sensitive parameterization.

480 The run using a parameterization which selects the minimum of the two length scales
 481 does much better over both continental slopes where the topographic Rhines scale kicks
 482 in. With suppressed diffusivities, the density front which is set up by the topographic
 483 PV gradient is no longer washed out completely. The result is an enhanced thermal wind
 484 shear over the northern slope, albeit with a lower absolute strength than in the high-resolution
 485 simulation. In the south, where the stratification is much weaker, the parameterization
 486 is not able to set up a thermal wind shear.

487 Further scaling by the eddy efficiency E_{eff} (Fig. 5, green) enhances the diffusiv-
 488 ity reduction in the north, but not necessarily in the south, as also observed for the high-
 489 diagnostics simulations. Therefore, the feedback to the resolved fields strengthens the
 490 baroclinic jet in the north further, but not in the south.

491 The above results are encouraging. However, although the channel setup is a rea-
 492 sonable test bed for development, it is extremely idealized and lacks multiple features
 493 from the real world (e.g. variable Coriolis parameter, uneven topography and complex
 494 atmospheric forcing). Therefore, we also test the slope-aware parameterization in the re-
 495 alistic global domain next.

496 4 Realistic global model simulations

497 4.1 Eddy parameterization adjustments

498 We carry out a 'control' simulation and 5 different perturbation experiments, but
 499 for simplicity, we focus on a comparison between the 'control' simulation and two of the
 500 perturbation experiments. All of these simulations operate with 2D diffusivities based
 501 on the depth-averaged Eady growth rate and a square length scale, as in (15). The con-
 502 trol run selects a length scale from the minimum of the internal deformation radius and
 503 the planetary Rhines scale. Then, in two distinct 'topo' runs we i) introduce the topo-
 504 graphic Rhines scale in the minimum function and ii) also turn on the eddy efficiency
 505 factor E_{eff} . The OMIP 'topo' runs then differ slightly from the coarse-resolution chan-
 506 nel setup in the choice of constant scaling factors. The constant factor a_1 which scales
 507 the overall diffusivity magnitude is set to 3 and factor a_2 used in E_{eff} is set to 1. In ad-
 508 dition, we scale the topographic Rhines scale further down with a constant factor 0.5 (stronger
 509 sensitivity to slopes). We view these constants as tuning factors specific to one partic-
 510 ular setup; for example, the resolution of the bottom topography dataset influences the
 511 strength of the topographic beta and thereby tuning the topographic Rhines scale might
 512 be needed. Finally, in all runs the diffusivity magnitude is scaled down with a resolu-
 513 tion function (Hallberg, 2013) when the deformation radius is resolved by the model grid.
 514 And, for simplicity, the along-isopycnal (Redi) tracer diffusivity is set to be the same as
 515 the GM diffusivity.

516 To put these experiments in some context, it should be mentioned that the model
 517 settings for the control run are similar to the NorESM model version used in the latest
 518 Climate Model Intercomparison Project (CMIP6) except for the GM diffusivity formu-
 519 lation. The CMIP6 version of the model included a mixing length formulation where the
 520 length scale was selected as the minimum of the internal deformation radius and the plan-
 521 etary Rhines scale—as in our control simulation. However, the local Eady growth rate
 522 was then evaluated at each model level, rendering a 3D profile for both eddy driven ad-
 523 vection (GM) and for along isopycnal mixing (Redi). Finally, the scaling-based diffusiv-
 524 ity was adjusted by a zonal velocity-dependent mean flow suppression following Ferrari
 525 and Nikurashin (2010), and as in the experiments here, a resolution function (Hallberg,
 526 2013) was also used.

527 The lack of vertical structure of the 2D parameterization proposed here, turned out
 528 to be a clear deficiency in the global domain as our initial simulations showed an unre-
 529 alistically strong sensitivity to bottom slopes in the low and mid-latitude deep ocean.
 530 For example, large reductions in the parameterized diffusivity across mid-ocean ridges
 531 were not seen in eddy-permitting studies that diagnosed eddy diffusivity in the global
 532 domain (e.g., Bachman et al., 2020). Therefore, to reduce the topographic impact on eddy
 533 fluxes in strongly stratified low and mid-latitude regions, we added an ad hoc 'limiter'
 534 of topographic effects—based on the assumption that if the resolved flow does not feel
 535 the bottom then it is unlikely that mesoscale eddies would do so either. Specifically, the
 536 topographic Rhines scale is scaled by $\cos(\alpha)^{-10}$ which rapidly increases the topographic
 537 Rhines scale when the angle α between the resolved flow and the bottom slope tangent
 538 vector deviate by more than $\sim 30^\circ$ i.e. when the resolved flow is not aligned with the bot-
 539 tom slope.

540 4.2 Model response in the global domain

541 As expected, introducing the topographic Rhines scale leads to locally reduced dif-
 542 fusivities over sloping topography, as shown in Figure 6 (top row). The effect is enhanced
 543 at high latitudes with a $\sim 50\%$ reduction over Arctic and Antarctic continental slopes.
 544 Bringing in the eddy efficiency E_{eff} leads to additional and more severe diffusivity re-
 545 duction globally, also away from topographic features (bottom row). This is in agree-
 546 ment with other recent studies that found the scaling by mean-flow dependent suppres-

547 sion to have the largest impact on diffusivity at global scale (Stanley et al., 2020; Zhang
 548 & Wolfe, 2022; Holmes et al., 2022). Note that in the tropics, the diffusivity is limited
 549 by the grid resolution function (Hallberg, 2013), i.e. the diffusivity is reduced when the
 550 grid size is smaller than the local deformation radius. Therefore, the large relative re-
 551 duction in tropical diffusivity is small in absolute terms and less important there as trans-
 552 port is dominated by the resolved flow. Finally, we note that a comparison between the
 553 top and the bottom rows in Figure 6 shows that in multiple continental slope regions,
 554 especially in the Arctic and around Antarctica, the eddy efficiency simply enhances the
 555 response seen with the topographic Rhine scale but the pattern stays the same. Indeed,
 556 the diffusivity reduction due to introducing the topographic Rhines scale and due to eddy
 557 efficiency are close to linearly additive (not shown).

558 As the impact of eddy efficiency on diffusivity is more broad, its impact on flow speed,
 559 temperature, and salinity is also more widespread than the impact of the topographic
 560 Rhines scale alone. Table 3 collects bias reductions (relative to the control case) across
 561 5 different experiments while Figures 7–9 show the spatial patterns for subsurface (100–
 562 200 m) current speed and temperature, as well as zonal-mean temperature and overturn-
 563 ing anomalies for the two ‘topo’ experiments that are in focus here. We show results for
 564 the subsurface response since the surface response in these forced simulations is strongly
 565 forced by the non-responsive atmosphere. Both the topographic Rhines scale alone and
 566 its combination with eddy efficiency increase the mean kinetic energy of the resolved flow
 567 globally (at 100–200 m depth, by 2.7% and 10.5%, respectively). This increase is espe-
 568 cially noticeable over sloping bathymetry where the two impacts contribute approximately
 569 equally to the overall increase (100–200 m depth where $\beta_t > 5E-10 \text{ m}^{-1}\text{s}^{-1}$, by 9.1%
 570 and 20.8%, respectively). The two modifications also warm the ocean below the global
 571 thermocline and cool the surface, reducing the overall temperature bias at depth. But
 572 they increase the temperature bias at the thermocline (Table 3; Fig. 9a,c). Overall, the
 573 mean overturning response in the ‘topo’ runs is characterized by a positive (cyclonic) anomaly
 574 which implies that the Atlantic overturning cell and the Deacon cell in the Southern Ocean
 575 strengthen, whereas the Antarctic Bottom Water cell and the shallow surface overturn-
 576 ing cells within the subtropical and subpolar gyres weaken. These changes generally re-
 577 duce biases. The simulated strength of the Atlantic overturning at $26^\circ N$ is 15.5 Sv in
 578 the the control simulation, 17 Sv when topographic Rhines scale is considered, and 18
 579 Sv with the addition of eddy efficiency, whereas the observational estimate from the RAPID
 580 array ($\sim 26^\circ N$) is 17 ± 3.3 Sv (Frajka-Williams et al., 2019). The Antarctic bottom wa-
 581 ter cell at $32^\circ S$ weakens from 26.0 Sv in the control simulation to 23.5 Sv with topographic
 582 Rhines scale and 20.3 Sv with addition of eddy efficiency, whereas inverse modelling sug-
 583 gest 20.9 ± 6.7 Sv (Lumpkin & Speer, 2007). The Deacon cell strengthens from 13.2 Sv
 584 in the control simulations to 15.2 Sv with the topographic Rhines scale and 18.4 Sv when
 585 eddy efficiency is considered, whereas previous modelling estimates (Döös et al., 2008)
 586 and observational estimates (Speer et al., 2000) suggest a strength of 20 Sv and 20–25
 587 Sv, respectively. The vertically-integrated mass and heat transports, plotted in Figure
 588 10, show that overall the overturning response leads to increasing heat transport towards
 589 the northern hemisphere. The northern hemisphere subtropical peak in northward heat
 590 transport in the Atlantic basin (globally) is 0.83 PW (1.07 PW) in the control simula-
 591 tion, 0.91 PW (1.15 PW) when topographic Rhines scale is considered, and 1.00 PW (1.26
 592 PW) with the addition of eddy efficiency, whereas Trenberth et al. (2019) estimate ap-
 593 proximately 1.1 PW (1.6 PW).

594 Some more specific impacts of the topographic Rhines scale and eddy efficiency are
 595 a poleward shift and strengthening of the boundary and slope currents, with E_{eff} gen-
 596 erally speeding up the boundary currents at locations where observations show the core
 597 of the currents (Fig. 7, observed currents in black). Changes in the net volume trans-
 598 ports in most key passages remain small (Table 4), but the results show a strengthen-
 599 ing of the ACC (Drake Passage transport; increased bias), a general enhancement of wa-
 600 ter exchange between the Arctic and mid-latitudes (opposing influence on the bias in dif-

601 ferent straits), and strengthening of the Gulf Stream (Florida–Bahamas strait transport,
 602 reduced bias). The spinup of the ACC is a direct consequence of reduced diffusivities,
 603 allowing for stronger thermal wind currents. In the northern North Atlantic, the cur-
 604 rent speed response is directly reflected in the temperature response as the Atlantic Wa-
 605 ter warms up along its path from the Nordic Seas to the Arctic (Fig. 8, reduced bias).
 606 Despite the speed-up of the Gulf Stream off the North American coast, its observed turn-
 607 ing around Grand Banks off Newfoundland is not reproduced. Due to this deficiency, the
 608 cold bias off Newfoundland strengthens (Fig. 8). This cold bias is a long standing issue
 609 in coarse resolution ocean models (Tsujino et al., 2020) and reducing the diffusivity along
 610 the current path or along the shelf break clearly does not mitigate the bias. We spec-
 611 ulate that, similar to the southern retrograde slope in the channel configuration and re-
 612 cent results on the Gulf Stream reported by Uchida et al. (2022), the eddy momentum
 613 flux convergence that is not included in the parameterization plays a crucial role in de-
 614 termining the current path.

615 Figure 10 summarizes the zonally-integrated impacts, breaking both volume and
 616 heat transport into resolved and parameterized eddy components. It illustrates how the
 617 reduced eddy mass transport across the ACC (panels a–b) also leads to less poleward
 618 heat transport (panels c–e) and therefore a cooling of the Southern Ocean surface, but
 619 also warming over the continental slopes (Fig. 8). Both these effects reduce the bias in
 620 the model. Note that the heat transport response is dominated by eddy-driven advec-
 621 tion with a smaller contribution due to the eddy diffusion (panels d–e). In contrast to
 622 the Southern Ocean, in the northern mid-latitudes the overall northward mass and heat
 623 transport increase as the mean overturning spins up (Fig. 10 panels a and c; Fig. 9 right
 624 panels) and the eddy contributions actually weaken (Fig. 10, panels b, d–e).

625 We note that since both the eddy efficiency and the topographic Rhines scale act
 626 to reduce the diffusivity, there is a limit to the effectiveness of these parameterizations
 627 because other processes and, specifically, the resolved flow start to dominate the model
 628 solution as the diffusivity weakens. For example, the reduction of globally integrated tem-
 629 perature and salinity biases seem to saturate as the topographic Rhines scale is tuned
 630 down and the eddy efficiency scaling is included (Table 3). This highlights the need to
 631 test parameterizations in realistic global settings and cautions against drawing conclu-
 632 sions of the effectiveness and utility of a parameterization based on assessing the diffu-
 633 sivity magnitude alone.

634 5 Discussion

635 Our study has focused on a relatively small range of parameterization choices, es-
 636 sentially i) re-examining the topographic Rhines scale as a relevant mixing length and
 637 ii) checking the importance of an additional suppression factor which we have called the
 638 eddy efficiency E_{eff} . The quite similar idealized studies by Wang and Stewart (2020)
 639 and Wei et al. (2022) did a more comprehensive sweep over possible parameterization
 640 choices but did not analyse prograde and retrograde bottom slopes under one and the
 641 same framework, which has been the intention here. Also, to the best of our knowledge,
 642 the current OMIP simulations constitute the first assessment of the impacts of a topographically-
 643 aware GM parameterization in realistic global ocean models. As such, this work should
 644 be taken as a pragmatic investigation into what can be achieved with simple parame-
 645 terization approaches applied to existing models that do not contain a prognostic eddy
 646 energy equation (which in itself requires parameterization choices). As with all param-
 647 eterizations, the options examined here are far from perfect, and below we discuss some
 648 shortcomings and unresolved questions.

5.1 The relevance of the topographic Rhines scale

Earlier idealized model studies have given conflicting evidence for the relevance of the topographic Rhines scale. Jansen et al. (2019) reported that using a generalized Rhines scale which accounts for both planetary and topographic beta in their eddy parameterization of flows in an idealized ACC-like domain improved their model skill. But the study, whose primary focus was on parameterizing an eddy energy budget, did not examine the length scale issue at any depth. More in line with our work here, the idealized channel studies of Wang and Stewart (2020) and Wei et al. (2022) found the topographic Rhines scale to be a useful choice over retrograde slopes—but not over prograde slopes. This conclusion was drawn, however, after an empirical slope-dependent prefactor was applied in the retrograde case but not in the prograde case. Both studies also constructed diffusivities from diagnosed depth-averaged EKE . In other words, they set the eddy velocity scale to be $V = \sqrt{EKE}$ and then defined $L_{Rh} = \sqrt{V/\beta_t}$, i.e. using the actual definition of the topographic Rhines scale. Our Figure 2, however, shows an EKE peak over the prograde slope which, if using their definition would clearly overestimate diffusivities over this slope. Here we find, somewhat surprisingly, that a full parameterization, using the Eady growth rate and the topographic beta parameter, produces a suppression over both prograde and retrograde slopes which nearly matches the ‘observations’ diagnosed from our high-resolution channel model.

We do not have a good understanding of this apparent paradox. But one possible problem with constructing a topographic Rhines scale from depth-averaged EKE is the fact that in a baroclinic system it is the bottom eddy velocity, rather than the depth-average, which should enter into the formulation. No considerations of the vertical structure of the eddy velocity was made here, but we suggest that future work on the topic investigates the skill in an equivalent barotropic formulation of the eddy velocity.

Moreover, the results shown in Figure 6 suggest that much of the discrepancy between the pure scaling-based diffusivity and the actual diffusivity is contained in the suppression factor which ours and other studies have pointed to. Essentially, the imperfect phase relationship between eddy velocity and buoyancy perturbations reduces the efficiency of eddy transfer by up to two orders of magnitude over continental slopes, possibly with larger suppression over prograde conditions. Any skillful parameterization clearly needs to try to account for this effect.

5.2 The interpretation of E_{eff}

Our parameterized expression (22), which is able to qualitatively reproduce such suppression, looks superficially similar to the final form of the mean-flow suppression expression of Ferrari and Nikurashin (2010, their equation 17). This first seems odd, given that their findings have traditionally been applied to tracer (Redi) diffusion and, as mentioned in the introduction, appears to quite successfully explain a reduction in passive tracer diffusion over a retrograde continental slope in the idealized simulations of Wei and Wang (2021). But eddy buoyancy transport at any one depth in the ocean is advective rather than diffusive, so it’s not at all obvious that the kinematic arguments of Ferrari and Nikurashin (2010) should apply to buoyancy diffusivities.

Indeed, Abernathey et al. (2013) use high-resolution model simulations to show that the vertical structure of buoyancy diffusivities differs from that of other tracer diffusivities (including PV diffusivities). And yet, as their equation 24 suggests, the depth-averaged value of the buoyancy diffusivity should be similar to that of PV and passive tracer diffusivities, at least in the case where the planetary vorticity gradient can be neglected. This makes some intuitive sense since one end result of a depth-integral of an eddy-induced overturning circulation, driven by baroclinic instability and with zero top-to-bottom volume transport, is a ‘diffusive’ buoyancy transport down the lateral buoyancy gradient (the other end result is an up-gradient vertical buoyancy transport).

700 But there are still difficulties with equating our E_{eff} with the mean-flow suppression
 701 formulation of Ferrari and Nikurashin (2010). Their suppression effect builds fun-
 702 damentally on the propagation speed of eddies relative to that of the mean flow. It is
 703 based on a set of key key assumptions, including the dominance of one wavenumber and
 704 a relationship between eddy decorrelation timescale, wavenumber and EKE. And in reach-
 705 ing their final equation 17, which takes on a form similar to our (23), they make the fur-
 706 ther assumption that the eddy speed is proportional to the mean flow speed. Since Ferrari
 707 and Nikurashin (2010) originally studied suppression at the sea surface, using satellite
 708 altimeter observations to pin down both mean and eddy velocity scales, this amounted
 709 to having to tune one proportionality constant. How their final expression 17 can be ap-
 710 plied through out the entire water column, as we're aiming for here, is less obvious. So
 711 we leave a further investigation into this particular relationship for future work.

It should also be mentioned that our E_{eff} can be related to the slope-dependent prefactors of some of the earlier channel studies as well as to a controlling parameter in the topographic Eady problem of Blumsack and Gierasch (1972). This connection becomes apparent if we evaluate the 2D version of (22). We begin by setting $U_{bc} = U_{tw}$, where U_{tw} is the top-to-bottom thermal wind shear (a 2D quantity). Then we first consider the slope region where the topographic Rhines scale will be the relevant length scale. So, here, $V = \sigma_E^2 / \beta_T$, where σ_E is now the depth-averaged (2D) Eady growth rate. Noting that in the Eady model, where both N^2 and $\partial U_g / \partial z$ are constant, $\sigma_E = 0.3 \cdot U_{tw} / L_R$. This allows us to rewrite (22) as

$$E_{eff} = a_1 \frac{1}{1 + a_3 (\beta_T L_R^2 / U_{tw})^2} \tag{24}$$

$$= a_1 \frac{1}{1 + a_3 \delta^2},$$

712 where a_3 is a modified tuning factor. Here $\delta = \beta_T L_R^2 / U_{tw}$ is the slope parameter of Blumsack
 713 and Gierasch (1972) which measures the ratio between topographic and isopycnal slopes.

714 This expression is interesting not only because it brings in the controlling param-
 715 eter of the modified Eady problem but also for its similarity to the slope-dependent pref-
 716 actor used by Wang and Stewart (2020) over retrograde slopes in the parameter regime
 717 where the bottom slope is not much larger than the isopycnal slope. Their prefactor F_{MLT}
 718 (from their table 3) has the topographic delta parameter to the power of one in the de-
 719 nominator, in contrast to our squared power. But we suggest that the impact of sam-
 720 pling errors in the empirical fitting be studied in future studies before the correspondence
 721 is rejected. We also note that the similar studies of prograde fronts by Brink (2016) and
 722 Wei et al. (2022) found best fits using similar expressions but using topographic Burger
 723 number Bu in place of the delta parameter, where the two are related via $Bu = (\sigma_E / f) \delta$.
 724 The latter study concluded that scalings using δ instead of Bu were not successful over
 725 prograde slopes. But, again, a comparison with our results are not straightforward since
 726 their diffusivities were constructed using diagnosed EKE while ours were fully param-
 727 eterized. The relationship between δ -based and Bu -based formulations is an obvious topic
 728 for future work.

729 Note, finally, that over the flat regions where the deformation radius will act as the
 730 relevant length scale, the 2D version of our efficiency factor becomes constant, in agree-
 731 ment with the behavior seen in Figure 3. In fact, the 2D version of E_{eff} was able to qual-
 732 itatively reproduce the observed eddy efficiency behaviour in the idealized channel sim-
 733 ulations, with some changes required for the tuning constants (not shown). We nonethe-
 734 less chose to use the 3D version in the realistic OMIP simulations in anticipation of a
 735 more complex hydrography and flow field where the various assumptions of the Eady model
 736 can be expected to hold to an even lesser degree than in the channel model. Interior thick-
 737 ness PV gradients, for example, are expected to be small in systems that are only forced
 738 by Ekman pumping, as our channel model is (see e.g. Meneghello et al., 2021; Manucharyan

739 & Stewart, 2022). In a real ocean, where e.g. thermohaline forcing can produce interior
 740 PV gradients, the suppression of eddy efficiency will inevitably be governed by additional
 741 non-dimensional parameters beyond Blumsack and Gierasch (1972) δ (or, alternatively,
 742 the topographic Burger number). Such 3D effects, caused by thermohaline forcing in ad-
 743 dition to wind stress, may also be the underlying reason for why E_{eff} had a much big-
 744 ger impact in the OMIP simulations than it did in the channel.

745 6 Summary and conclusions

746 Efforts to include topographic effects into mesoscale eddy parameterizations are
 747 warranted, especially at high latitudes where observations show that hydrographic fronts
 748 are typically locked to topography. The very existence of such fronts along continental
 749 slopes and submarine ridges imply not merely topographic steering of large-scale cur-
 750 rents but also suppression of mesoscale stirring across topography. Yet, despite all the
 751 observational evidence, as well as solid theoretical arguments for e.g. reduced growth rates
 752 and length scales of baroclinic instability over sloping topography, most eddy parame-
 753 terizations still fail to account for any bathymetric influence.

754 Here we have re-examined the relevance of the topographic Rhines scale in the mix-
 755 ing length approach to parameterizing the Gent-McWilliams diffusivity which is used for
 756 eddy advection. Constructing diffusivities using the Eady growth rate and a parameter-
 757 ized version of the topographic Rhines scale reproduces an observed order-of-magnitude
 758 reduction in diffusivity over continental slopes in idealized channel simulations. The sim-
 759 ulations and analysis cover both prograde and retrograde continental slopes, represent-
 760 ing mean flows in the same and opposite direction to topographic waves, respectively.
 761 Although differing in detail, both the observed and parameterized stirring suppression
 762 are of similar order of magnitude on both sides. The skill of the parameterization is en-
 763 hanced further, at least over the prograde slope, when the diffusivity is multiplied by an
 764 eddy efficiency factor E_{eff} that is sensitive to the strength of the mean flow vertical shear
 765 relative to the parameterized eddy velocity scale. Finally, we find that selecting a smooth
 766 minimum of the topographic Rhines scale and the internal deformation radius for length
 767 scale gives good skill over the entire idealized channel domain.

768 The parameterization is then tested in a realistic global ocean simulation. Com-
 769 parison with a simulation where topographic effects on the GM diffusivity are not in-
 770 cluded suggests that the parameterized topographic stirring suppression enhances the
 771 sharpness of hydrographic fronts and, as such, strengthens the thermal wind shear in bound-
 772 ary currents. The improvement is particularly noticeable at high latitudes, but we also
 773 observe large impacts throughout the world oceans. The globally-integrated tempera-
 774 ture and salinity bias reductions range from O(1%)-O(10%), with largest reductions seen
 775 in Southern Ocean temperatures and in Atlantic Water temperatures in the Arctic. How-
 776 ever, existing low-latitude thermocline biases tend to increase. This is not uncommon
 777 in a complex model as global bias reduction is very much a tuning exercise involving a
 778 range of free parameters associated with different parameterizations (e.g. eddy transport,
 779 vertical mixing and air-sea-ice fluxes). Our parameterization also has free parameters
 780 and, as is common, we found that the different model configurations might need differ-
 781 ent values for these. But we did not attempt a rigorous tuning, especially not for the dy-
 782 namically complex OMIP simulations. Our focus at this stage has not been on a well-
 783 tuned realistic global simulation, but rather on illustrating possible impacts of a topography-
 784 aware eddy parameterization.

785 The suggested parameterization is clearly incomplete. The large difference in im-
 786 portance of the efficiency factor E_{eff} between the channel simulations and the realis-
 787 tic OMIP simulations is one indication of this. A second one is the fact that we had to
 788 use an ad hoc limiter when applying this in the OMIP simulations. One key problem is
 789 likely that we have been ignoring any vertical structure in eddy velocities and, ultimately,

diffusivities. Fundamentally, the kinematic interaction with the bottom involves eddy bottom velocities, and a number of observations as well as theoretical arguments have indicated that these are often significantly smaller than surface or even depth-averaged eddy velocities (see e.g. Killworth, 1992; Wunsch, 1997; de La Lama et al., 2016; Lacasce, 2017). The topographic impact, under such considerations, would probably be smaller than if estimated with depth-averaged quantities. Future work clearly needs to be put on such vertical structure, for example by taking an equivalent barotropic structure as a starting point (Killworth, 1992). We also observe that in our coarse-resolution channel simulations the flow remains too baroclinic, similar to the results by Kjellsson and Zanna (2017); Yankovsky et al. (2022). Although addition of vertical structure to the buoyancy diffusivity might mitigate the issue, feeding the mean flow with vertically distributed eddy energy might be needed to resolve it (Yankovsky et al., 2022).

A related issue which we have entirely neglected in this study is the impact of bottom roughness or corrugations on fluxes—and how such impact may be asymmetric with respect to the flow direction. As demonstrated by Wang and Stewart (2020), bottom roughness along a retrograde topographic slope can set up additional eddy buoyancy transport and, thus, form stresses due to arrested topographic waves. The dynamics governing such fluxes are likely distinct from those captured by our parameterizations here for smooth topography. The relevant eddy length scale, for example, is probably not the same as for transient eddies, as indicated in the study by Khani et al. (2019) of transient vs. standing contributions to eddy form stress in an idealized Southern Ocean domain. The application of standing Rossby wave theory (e.g. Abernathey & Cessi, 2014; A. L. Stewart et al., 2023) appears to give promising results on the planetary beta plane with a flat but rough bottom. A natural next step may therefore be to examine such ideas to the ‘topographic beta’ problem, using e.g. the idealized two-slope model used here.

Yet another issue ignored here is the role of lateral eddy momentum fluxes over continental slopes. As shown in Figure 1 and also highlighted in earlier studies (e.g. Wang & Stewart, 2018; Manucharyan & Isachsen, 2019), such fluxes bring wind momentum off the slopes to relatively flat regions where baroclinic instability kicks in to transfer the momentum to the ground below. The lateral momentum flux may be up-gradient in places and form eddy-driven jets, as seen offshore of the retrograde slope in our idealized simulations (Fig. 1). And, as for eddy form stress, lateral momentum fluxes also appear to be impacted by corrugated bottoms, being associated with the formation of prograde jets near the bottom (Wang & Stewart, 2020). This last effect is again probably related to the formation of arrested topographic waves, as discussed by (e.g. Haidvogel & Brink, 1986), as well as being linked to down-gradient PV diffusion in the finite-amplitude limit Bretherton and Haidvogel (1976); Vallis and Maltrud (1993).

Finally, it’s worth remembering that eddy diffusion, even of buoyancy, may be anisotropic. So what really needs to be parameterized is a diffusion tensor rather than a single scalar. Bachman et al. (2020) discussed such anisotropy of the diffusion tensor and showed that at global scale the direction of the major axis of the tensor is well correlated with the mean flow direction and the minor axis is well correlated with the gradient of Ertel PV. In addition, Nummelin et al. (2021, Appendix A) suggested that in terms of Redi mixing, the Ferrari and Nikurashin (2010) type of mean flow suppression indeed suppresses the across-flow mixing, but that the inverse of the same factor enhances mixing in the along-flow direction. It remains unclear whether our eddy efficiency factor and the other empirical scaling factors (e.g. Wang & Stewart, 2020; Wei et al., 2022) act similarly (i.e. relate to tensor anisotropy) or if they indeed suppress the overall tensor magnitude. In other words, it remains a research question whether the mean flow and topography merely direct the eddy transport or if they impact the overall magnitude of the eddy transport. Nevertheless, if the tensor major axis is correlated with the mean flow (as suggested by Bachman et al., 2020) —and if that mean flow transport dominates over eddy transport— then the focus on the minor axis is likely justified.

Table 1. BLOM model constants for the channel simulations

Name	Symbol	Value
Wind stress	τ_x	0.05 N m ⁻²
Horiz. grid size	$\Delta x, \Delta y$	2 km
Baroclinic timestep	Δt	120 s
Domain x-size	L_x	416 km
Domain y-size	L_y	1024 km
Gravitational acceleration	g	9.806 m s ⁻²
Coriolis parameter	f_0	1×10^{-4} s ⁻¹
Slope mid-point distance from domain edge	Y_S	150 km
Shelf depth	H_{Shelf}	250 m
Slope height	H_{Slope}	2000 m

Table 2. Channel model experiments. L_{Rossby} is the mean deformation radius in the central basin (where bottom depth is larger than 2250 m).

Name	L_{Rossby}	Slope Width
Exp 1	34.1 ± 1.3 km	75 km
Exp 2	34.1 ± 1.1 km	100 km
Exp 3	34.4 ± 1.0 km	125 km
Exp 4	30.6 ± 1.3 km	75 km
Exp 5	30.6 ± 1.2 km	100 km
Exp 6	30.4 ± 1.0 km	125 km
Exp 8	24.9 ± 1.2 km	75 km
Exp 9	25.9 ± 1.0 km	100 km
Exp 10	24.9 ± 1.0 km	125 km

843 So important questions remain. But despite its many shortcomings, the relatively
844 simple parameterization investigated here at least reduces an excessive washing out of
845 hydrographic fronts over submarine ridges and continental slopes in ocean climate models—
846 a known problem with eddy parameterizations that are insensitive of bathymetry. One
847 of several important consequences of such adjustment is likely a more accurate repre-
848 sentation of oceanic heat transport across Antarctic and Greenland continental slopes
849 and onward to the great ice sheets whose melt rates depend intimately on such trans-
850 port. For this and other reasons, further scrutiny of all of the above unresolved issues
851 and their impacts in both regional and global realistic simulations are much needed.

852 7 Open Research

853 The model configuration is available at <https://github.com/NorESMhub/BLOM>
854 and the specific namelist for running the experiments used in this study can be obtained
855 from the first author. The key model output and scripts to reproduce the data are made
856 available through <https://archive.norstore.no/> and will be made available through <https://github.com/AleksiNummela>
857 upon publication.

Table 3. CORE-II hydrography bias (root mean square error) reduction compared to the bias of the control case. The observational data sets are the WOA 2018 climatologies for temperature (Locarnini et al., 2018) and salinity (Zweng et al., 2018).

Name	zonal mean T	zonal mean S	$T_{100-200m}$	$T_{200-500m}$	$T_{500-1000m}$
L_T	6%	4%	-2%	1%	3%
$0.5 \cdot L_T$	12%	9%	-4%	3%	7%
E_{eff}	25%	21%	-11%	2%	12%
L_T and E_{eff}	28%	24%	-13%	2%	16%
$0.5 \cdot L_T$ and E_{eff}	28%	26%	-16%	2%	18%

Table 4. Observed and simulated current transport in selected straits. The various perturbation experiments show percentage changes relative to the control case. The references for the observational values are as follows: Arctic Ocean gateway transports come from de Boer et al. (2018) with the original citations being Ingvaldsen et al. (2004) for Barents Sea Opening, Beszczynska-Möller et al. (2015) for Fram Strait, Curry et al. (2014) for Davis Strait (CAA), and Woodgate (2018); Woodgate et al. (2015) for Bering Strait; ACC transport come from Xu et al. (2020), for pure observational estimates see Koenig et al. (2014) and Donohue et al. (2016); and Florida–Bahamas Strait transport come from Larsen and Sanford (1985)

Name	obs	control	L_T	$0.5 \cdot L_T$	E_{eff}	L_T and E_{eff}	$0.5 \cdot L_T$ and E_{eff}
Barents Opening	2.1 Sv	2.4 Sv	0%	1%	4%	6%	7%
Bering Strait	1.0 Sv	0.7 Sv	2%	3%	5%	7%	8%
Canadian Arctic	-1.7 Sv	-1.6 Sv	4%	8%	14%	15%	16%
Fram Strait	-2.2 Sv	-1.3 Sv	-3%	-6%	-9%	-6%	-6%
Drake Passage (ACC)	157.3 Sv	152 Sv	0%	1%	4%	5%	7%
Florida–Bahamas Strait	32 Sv	13.2 Sv	1%	3%	4%	5%	6%

Acknowledgments

This work was funded in part by the two Research Council of Norway projects KeyClim (295046) and TopArctic (314826). A. Nummelin would like to thank Mats Bentsen for the help with the initial model setup.

References

- Abernathy, R., & Cessi, P. (2014). Topographic enhancement of eddy efficiency in baroclinic equilibrium. *J. Phys. Oceanogr.*, *44*, 2017–2126.
- Abernathy, R., Ferreira, D., & Klocker, A. (2013). Diagnostics of isopycnal mixing in a circumpolar channel. *Ocean Modelling*, *72*, 1 - 16. Retrieved from <http://www.sciencedirect.com/science/article/pii/S1463500313001200> doi: <https://doi.org/10.1016/j.ocemod.2013.07.004>
- Bachman, S. D. (2019). The GM+E closure: A framework for coupling backscatter with the Gent and McWilliams parameterization. *Ocean Modelling*, *136*, 85 - 106. Retrieved from <http://www.sciencedirect.com/science/article/pii/S1463500318301975> doi: <https://doi.org/10.1016/j.ocemod.2019.02.006>
- Bachman, S. D., Fox-Kemper, B., & Bryan, F. O. (2020). A diagnosis of anisotropic eddy diffusion from a high-resolution global ocean model. *Journal of Advances in Modeling Earth Systems*, *12*(2), e2019MS001904. Retrieved from <https://agupubs.onlinelibrary.wiley.com/doi/abs/10.1029/2019MS001904> doi: [10.1029/2019MS001904](https://doi.org/10.1029/2019MS001904)
- Beszczynska-Möller, A., von Appen, W.-J., & Fahrback, E. (2015). *Physical oceanography and current meter data from moorings F1-F14 and F15/F16 in the Fram Strait, 1997-2012* [data set]. PANGAEA. Retrieved from <https://doi.org/10.1594/PANGAEA.150016> doi: [10.1594/PANGAEA.150016](https://doi.org/10.1594/PANGAEA.150016)
- Blumsack, S. L., & Gierasch, P. J. (1972). Mars: The effects of topography on baroclinic instability. *J. Atmos. Sci.*, *29*, 1081-1089.
- Bretherton, F. P., & Haidvogel, D. (1976). Two-dimensional turbulence over topography. *J. Fluid. Mech.*, *78*, 129–154.
- Brink, K. H. (2012). Baroclinic instability of an idealized tidal mixing front. *J. Mar. Res.*, *70*(4), 661–688.
- Brink, K. H. (2016). Cross-shelf exchange. *Annual Review of Marine Science*, *8*(1), 59-78. Retrieved from <https://doi.org/10.1146/annurev-marine-010814-015717> (PMID: 26747520) doi: [10.1146/annurev-marine-010814-015717](https://doi.org/10.1146/annurev-marine-010814-015717)
- Buongiorno Nardelli, B. (2020). A multi-year time series of observation-based 3d horizontal and vertical quasi-geostrophic global ocean currents. *Earth System Science Data*, *12*(3), 1711–1723. Retrieved from <https://essd.copernicus.org/articles/12/1711/2020/> doi: [10.5194/essd-12-1711-2020](https://doi.org/10.5194/essd-12-1711-2020)
- Chang, P., Zhang, S., Danabasoglu, G., Yeager, S. G., Fu, H., Wang, H., ... Wu, L. (2020). An unprecedented set of high-resolution earth system simulations for understanding multiscale interactions in climate variability and change. *Journal of Advances in Modeling Earth Systems*, *12*(12), e2020MS002298. Retrieved from <https://agupubs.onlinelibrary.wiley.com/doi/abs/10.1029/2020MS002298> (e2020MS002298 2020MS002298) doi: <https://doi.org/10.1029/2020MS002298>
- Curry, B., Lee, C. M., Petrie, B., Moritz, R. E., & Kwok, R. (2014). Multi-year volume, liquid freshwater, and sea ice transports through Davis Strait, 2004–10. *Journal of Physical Oceanography*, *44*(4), 1244 - 1266. Retrieved from <https://journals.ametsoc.org/view/journals/phoc/44/4/jpo-d-13-0177.1.xml> doi: [10.1175/JPO-D-13-0177.1](https://doi.org/10.1175/JPO-D-13-0177.1)
- de Boer, A. M., Gavilan Pascual-Ahuir, E., Stevens, D. P., Chafik, L., Hutchinson, D. K., Zhang, Q., ... Willmott, A. J. (2018). Interconnectivity between volume transports through arctic straits. *Journal of Geophysical Research: Oceans*, *123*(12), 8714-8729. Retrieved from <https://doi.org/10.1029/2018JC014000>

- 911 [agupubs.onlinelibrary.wiley.com/doi/abs/10.1029/2018JC014320](https://doi.org/10.1029/2018JC014320) doi:
912 <https://doi.org/10.1029/2018JC014320>
- 913 de La Lama, M., Lacasce, J. H., & Fuhr, H. K. (2016). The vertical structure of
914 ocean eddies. *Dynamics and Statistics of the Climate System*, 1(1), 1–16. doi:
915 10.1093/climsys/dzw001
- 916 Donohue, K. A., Tracey, K. L., Watts, D. R., Chidichimo, M. P., & Chereskin, T. K.
917 (2016). Mean antarctic circumpolar current transport measured in drake
918 passage. *Geophysical Research Letters*, 43(22), 11,760–11,767. Retrieved
919 from [https://agupubs.onlinelibrary.wiley.com/doi/abs/10.1002/
920 2016GL070319](https://agupubs.onlinelibrary.wiley.com/doi/abs/10.1002/2016GL070319) doi: <https://doi.org/10.1002/2016GL070319>
- 921 Döös, K., Nycander, J., & Coward, A. C. (2008). Lagrangian decomposition of the
922 deacon cell. *Journal of Geophysical Research: Oceans*, 113(C7). Retrieved
923 from [https://agupubs.onlinelibrary.wiley.com/doi/abs/10.1029/
924 2007JC004351](https://agupubs.onlinelibrary.wiley.com/doi/abs/10.1029/2007JC004351) doi: <https://doi.org/10.1029/2007JC004351>
- 925 Eady, E. T. (1949). Long waves and cyclone waves. *Tellus*, 1(3), 33–52. Re-
926 trieved from [https://onlinelibrary.wiley.com/doi/abs/10.1111/
927 j.2153-3490.1949.tb01265.x](https://onlinelibrary.wiley.com/doi/abs/10.1111/j.2153-3490.1949.tb01265.x) doi: 10.1111/j.2153-3490.1949.tb01265.x
- 928 Eden, C. (2007). Eddy length scales in the North Atlantic Ocean. *J. Geophys. Res.*,
929 112(C06004). doi: 10.1029/2006JC003901
- 930 Eden, C., & Greatbatch, R. J. (2008). Towards a mesoscale eddy closure. *Ocean
931 Modelling*, 20(3), 223 - 239. Retrieved from [http://www.sciencedirect.com/
932 science/article/pii/S1463500307001163](http://www.sciencedirect.com/science/article/pii/S1463500307001163) doi: [https://doi.org/10.1016/
933 j.ocemod.2007.09.002](https://doi.org/10.1016/j.ocemod.2007.09.002)
- 934 Ferrari, R., & Nikurashin, M. (2010). Suppression of eddy diffusivity across jets in
935 the southern ocean. *Journal of Physical Oceanography*, 40(7), 1501–1519. doi:
936 10.1175/2010JPO4278.1
- 937 Fox-Kemper, B., Adcroft, A., nung, C. W. B., Chassignet, E. P., Curchitser,
938 E., Danabasoglu, G., ... Yeager, S. G. (2019, feb). Challenges and
939 prospects in ocean circulation models. *Frontiers in Marine Science*, 6. doi:
940 10.3389/fmars.2019.00065
- 941 Fox-Kemper, B., Ferrari, R., & Hallberg, R. (2008). Parameterization of mixed
942 layer eddies. part i: Theory and diagnosis. *Journal of Physical Oceanography*,
943 38(6), 1145 - 1165. Retrieved from [https://journals.ametsoc.org/view/
944 journals/phoc/38/6/2007jpo3792.1.xml](https://journals.ametsoc.org/view/journals/phoc/38/6/2007jpo3792.1.xml) doi: [https://doi.org/10.1175/
945 2007JPO3792.1](https://doi.org/10.1175/2007JPO3792.1)
- 946 Frajka-Williams, E., Ansorge, I. J., Baehr, J., Bryden, H. L., Chidichimo, M. P.,
947 Cunningham, S. A., ... Wilson, C. (2019). Atlantic meridional overturning
948 circulation: Observed transport and variability. *Frontiers in Marine Science*,
949 6. Retrieved from [https://www.frontiersin.org/articles/10.3389/
950 fmars.2019.00260](https://www.frontiersin.org/articles/10.3389/fmars.2019.00260) doi: 10.3389/fmars.2019.00260
- 951 Fratantoni, D. M. (2001). North Atlantic surface circulation during the 1990's ob-
952 served with satellite-tracked drifters. *Journal of Geophysical Research: Oceans
953 (1978–2012)*, 106(C10), 22067–22093.
- 954 Gent, P. R. (2011). The gent–mcwilliams parameterization: 20/20 hindsight. *Ocean
955 Modelling*, 39(1), 2 - 9. Retrieved from [https://doi.org/10.1016/j.ocemod
956 .2010.08.002](https://doi.org/10.1016/j.ocemod.2010.08.002) doi: 10.1016/j.ocemod.2010.08.002
- 957 Gent, P. R., & McWilliams, J. C. (1990). Isopycnal mixing in ocean circulation
958 models. *Journal of Physical Oceanography*, 20(1), 150–155. Retrieved from
959 [https://doi.org/10.1175/1520-0485\(1990\)020<0150:IMIOCM>2.0.CO;2
960 doi: 10.1175/1520-0485\(1990\)020\(0150:IMIOCM\)2.0.CO;2](https://doi.org/10.1175/1520-0485(1990)020<0150:IMIOCM>2.0.CO;2)
- 961 Gent, P. R., Willebrand, J., McDougall, T. J., & McWilliams, J. C. (1995).
962 Parameterizing eddy-induced tracer transports in ocean circulation mod-
963 els. *Journal of Physical Oceanography*, 25(4), 463–474. Retrieved from
964 [https://doi.org/10.1175/1520-0485\(1995\)025<0463:PEITTI>2.0.CO;2
965 doi: 10.1175/1520-0485\(1995\)025\(0463:PEITTI\)2.0.CO;2](https://doi.org/10.1175/1520-0485(1995)025<0463:PEITTI>2.0.CO;2)

- 966 Green, J. S. (1970). Transfer properties of the large-scale eddies and the general cir-
 967 culation of the atmosphere. *Quart. J. Roy. Meteor. Soc.*, *96*, 157–185.
- 968 Haidvogel, D. B., & Brink, K. H. (1986). Mean currents driven by topographic drag
 969 over the continental shelf and slope. *J. Phys. Oceanogr.*, *16*, 2159–2171.
- 970 Hallberg, R. (2013). Using a resolution function to regulate parameterizations of
 971 oceanic mesoscale eddy effects. *Ocean Modelling*, *72*, 92 - 103. Retrieved from
 972 <https://doi.org/10.1016/j.ocemod.2013.08.007> doi: 10.1016/j.ocemod
 973 .2013.08.007
- 974 Hetland, R. D. (2017). Suppression of baroclinic instabilities in buoyancy-driven flow
 975 over sloping bathymetry. *J. Phys. Oceanogr.*, *47*(1). doi: 10.1175/JPO-D-15
 976 -0240.1
- 977 Holmes, R. M., Groeskamp, S., Stewart, K. D., & McDougall, T. J. (2022). Sensi-
 978 tivity of a coarse-resolution global ocean model to a spatially variable neu-
 979 tral diffusivity. *Journal of Advances in Modeling Earth Systems*, *14*(3),
 980 e2021MS002914. Retrieved from [https://agupubs.onlinelibrary.wiley](https://agupubs.onlinelibrary.wiley.com/doi/abs/10.1029/2021MS002914)
 981 [.com/doi/abs/10.1029/2021MS002914](https://agupubs.onlinelibrary.wiley.com/doi/abs/10.1029/2021MS002914) (e2021MS002914 2021MS002914) doi:
 982 <https://doi.org/10.1029/2021MS002914>
- 983 Ingvaldsen, R. B., Asplin, L., & Loeng, H. (2004). Velocity field of the western en-
 984 trance to the barents sea. *Journal of Geophysical Research: Oceans*, *109*(C3).
 985 Retrieved from [https://agupubs.onlinelibrary.wiley.com/doi/abs/](https://agupubs.onlinelibrary.wiley.com/doi/abs/10.1029/2003JC001811)
 986 [10.1029/2003JC001811](https://agupubs.onlinelibrary.wiley.com/doi/abs/10.1029/2003JC001811) doi: <https://doi.org/10.1029/2003JC001811>
- 987 Isachsen, P. E. (2011). Baroclinic instability and eddy tracer transport across
 988 sloping bottom topography: How well does a modified eady model do in
 989 primitive equation simulations? *Ocean Modelling*, *39*(1), 183-199. Re-
 990 trieved from [https://www.sciencedirect.com/science/article/pii/](https://www.sciencedirect.com/science/article/pii/S1463500310001460)
 991 [S1463500310001460](https://www.sciencedirect.com/science/article/pii/S1463500310001460) (Modelling and Understanding the Ocean Mesoscale and
 992 Submesoscale) doi: <https://doi.org/10.1016/j.ocemod.2010.09.007>
- 993 Jansen, M. F., Adcroft, A., Khani, S., & Kong, H. (2019). Toward an Energet-
 994 ically Consistent, Resolution Aware Parameterization of Ocean Mesoscale
 995 Eddies. *Journal of Advances in Modeling Earth Systems*, *0*(0). Retrieved
 996 from [https://agupubs.onlinelibrary.wiley.com/doi/abs/10.1029/](https://agupubs.onlinelibrary.wiley.com/doi/abs/10.1029/2019MS001750)
 997 [2019MS001750](https://agupubs.onlinelibrary.wiley.com/doi/abs/10.1029/2019MS001750) doi: 10.1029/2019MS001750
- 998 Jansen, M. F., Adcroft, A. J., Hallberg, R., & Held, I. M. (2015). Parameterization
 999 of eddy fluxes based on a mesoscale energy budget. *Ocean Mod.*, *92*, 28–41.
- 1000 Khani, S., Jansen, M. F., & Adcroft, A. (2019). Diagnosing subgrid mesoscale eddy
 1001 fluxes with and without topography. *J. Adv. Mod. Earth Sci.*, *11*, 3995–4015.
 1002 doi: 10.1029/2019MS001721
- 1003 Killworth, P. D. (1992). An equivalent-barotropic mode in the Fine Resolu-
 1004 tion Antarctic Model. *J. Phys. Oceanogr.*, *22*, 1379–1387. doi: 10.1175/
 1005 1520-0485(1992)022
- 1006 Kjellsson, J., & Zanna, L. (2017). The impact of horizontal resolution on energy
 1007 transfers in global ocean models. *Fluids*, *2*(3). Retrieved from [https://www](https://www.mdpi.com/2311-5521/2/3/45)
 1008 [.mdpi.com/2311-5521/2/3/45](https://www.mdpi.com/2311-5521/2/3/45) doi: 10.3390/fluids2030045
- 1009 Klocker, A., Ferrari, R., & LaCasce, J. H. (2012). Estimating suppression of eddy
 1010 mixing by mean flows. *Journal of Physical Oceanography*, *42*(9), 1566–1576.
- 1011 Koenig, Z., Provost, C., Ferrari, R., Sennéchaël, N., & Rio, M.-H. (2014). Volume
 1012 transport of the antarctic circumpolar current: Production and validation of
 1013 a 20 year long time series obtained from in situ and satellite observations.
 1014 *Journal of Geophysical Research: Oceans*, *119*(8), 5407-5433. Retrieved
 1015 from [https://agupubs.onlinelibrary.wiley.com/doi/abs/10.1002/](https://agupubs.onlinelibrary.wiley.com/doi/abs/10.1002/2014JC009966)
 1016 [2014JC009966](https://agupubs.onlinelibrary.wiley.com/doi/abs/10.1002/2014JC009966) doi: <https://doi.org/10.1002/2014JC009966>
- 1017 Koszalka, I., LaCasce, J., Andersson, M., Orvik, K., & Mauritzen, C. (2011). Sur-
 1018 face circulation in the Nordic Seas from clustered drifters. *Deep-Sea Res. I*,
 1019 *58*, 468–485.
- 1020 LaCasce, J. H. (2000). Floats and f/H. *J. Mar. Res.*, *58*, 61–95.

- 1021 Lacasce, J. H. (2017). The Prevalence of oceanic surface modes. *Geophys. Res.*
 1022 *Lettr.*, *44*(21), 11097–11105. doi: 10.1002/2017GL075430
- 1023 Lacasce, J. H., & Brink, K. (2000). Geostrophic turbulence over a slope. *J. Phys.*
 1024 *Oceanogr.*, *30*, 1305–1324.
- 1025 Larsen, J. C., & Sanford, T. B. (1985). Florida current volume transports from volt-
 1026 age measurements. *Science*, *227*(4684), 302-304. Retrieved from [https://](https://www.science.org/doi/abs/10.1126/science.227.4684.302)
 1027 www.science.org/doi/abs/10.1126/science.227.4684.302 doi: 10.1126/
 1028 science.227.4684.302
- 1029 Locarnini, R. A., Mishonov, A. V., Baranova, O. K., Boyer, T. P., Zweng, M. M.,
 1030 Garcia, H. E., ... Smolyar, I. (2018). *World ocean atlas 2018, volume 1:*
 1031 *Temperature. a. mishonov technical ed.* NOAA Atlas NESDIS 81, 52pp. Re-
 1032 trieved from [https://www.ncei.noaa.gov/sites/default/files/2022-06/](https://www.ncei.noaa.gov/sites/default/files/2022-06/woa18.vol1.pdf)
 1033 [woa18.vol1.pdf](https://www.ncei.noaa.gov/sites/default/files/2022-06/woa18.vol1.pdf)
- 1034 Lumpkin, R., & Speer, K. (2007). Global ocean meridional overturning. *Journal*
 1035 *of Physical Oceanography*, *37*(10), 2550 - 2562. Retrieved from [https://](https://journals.ametsoc.org/view/journals/phoc/37/10/jpo3130.1.xml)
 1036 journals.ametsoc.org/view/journals/phoc/37/10/jpo3130.1.xml doi:
 1037 <https://doi.org/10.1175/JPO3130.1>
- 1038 Mak, J., Maddison, J. R., Marshall, D. P., & Munday, D. R. (2018). Implementation
 1039 of a geometrically informed and energetically constrained mesoscale eddy pa-
 1040 rameterization in an ocean circulation model. *Journal of Physical Oceanogra-*
 1041 *phy*, *0*(0), null. Retrieved from <https://doi.org/10.1175/JPO-D-18-0017.1>
 1042 doi: 10.1175/JPO-D-18-0017.1
- 1043 Manucharyan, G. E., & Isachsen, P. E. (2019). Critical Role of Continental Slopes
 1044 in Halocline and Eddy Dynamics of the Ekman-Driven Beaufort Gyre. *J. Geo-*
 1045 *phys. Res.*, *124*, 2679–2696. doi: 10.1029/2018JC014624
- 1046 Manucharyan, G. E., & Stewart, A. L. (2022). Stirring of interior potential porticity
 1047 gradients as a formation mechanism for large subsurface-intensified eddies in
 1048 the Beaufort Gyre. *J. Phys. Oceanogr.*, *52*, 3349–3370.
- 1049 Marshall, D. P., Maddison, J. R., & Berloff, P. S. (2012). A framework for pa-
 1050 rameterizing eddy potential vorticity fluxes. *Journal of Physical Oceanography*,
 1051 *42*(4), 539-557. Retrieved from <https://doi.org/10.1175/JPO-D-11-048.1>
 1052 doi: 10.1175/JPO-D-11-048.1
- 1053 Mechoso, C. R. (1980). Baroclinic instability of flows along sloping boundaries. *J.*
 1054 *Atmos. Sci.*, *37*, 1393–1399.
- 1055 Meneghello, G., Marshall, J., Lique, C., Isachsen, P. E., Doddridge, E., Campin,
 1056 J.-M., ... Talandier, C. (2021). Genesis and decay of mesoscale baro-
 1057 clinic eddies in the seasonally ice-covered interior arctic ocean. *Journal*
 1058 *of Physical Oceanography*, *51*(1), 115 - 129. Retrieved from [https://](https://journals.ametsoc.org/view/journals/phoc/51/1/jpo-d-20-0054.1.xml)
 1059 journals.ametsoc.org/view/journals/phoc/51/1/jpo-d-20-0054.1.xml
 1060 doi: 10.1175/JPO-D-20-0054.1
- 1061 Nummelin, A., Busecke, J. J. M., Haine, T. W. N., & Abernathey, R. P. (2021).
 1062 Diagnosing the scale- and space-dependent horizontal eddy diffusivity at the
 1063 global surface ocean. *Journal of Physical Oceanography*, *51*(2), 279 - 297. Re-
 1064 trieved from [https://journals.ametsoc.org/view/journals/phoc/51/2/](https://journals.ametsoc.org/view/journals/phoc/51/2/jpo-d-19-0256.1.xml)
 1065 [jpo-d-19-0256.1.xml](https://journals.ametsoc.org/view/journals/phoc/51/2/jpo-d-19-0256.1.xml) doi: 10.1175/JPO-D-19-0256.1
- 1066 Nøst, O. A., & Isachsen, P. E. (2003). The large-scale time-mean ocean circulation
 1067 in the Nordic Seas and Arctic Ocean estimated from simplified dynamics. *J.*
 1068 *Mar. Res.*, *61*, 175-210.
- 1069 Prandtl, L. (1925, January). 7. Bericht über Untersuchungen zur ausgebildeten Tur-
 1070 bulenz. *Zeitschrift Angewandte Mathematik und Mechanik*, *5*(2), 136-139. doi:
 1071 10.1002/zamm.19250050212
- 1072 Redi, M. H. (1982). Oceanic isopycnal mixing by coordinate rotation. *Jour-*
 1073 *nal of Physical Oceanography*, *12*(10), 1154-1158. Retrieved from [https://doi](https://doi.org/10.1175/1520-0485(1982)012<1154:OIMBCR>2.0.CO;2)
 1074 [.org/10.1175/1520-0485\(1982\)012<1154:OIMBCR>2.0.CO;2](https://doi.org/10.1175/1520-0485(1982)012<1154:OIMBCR>2.0.CO;2) doi: 10.1175/
 1075 1520-0485(1982)012(1154:OIMBCR)2.0.CO;2

- 1076 Rhines, P. (1977). The dynamics of unsteady currents. In *The sea* (Vol. 6,
1077 p. 189–318). New York: Wiley.
- 1078 Seland, Ø., Bentsen, M., Olivie, D., Toniazzo, T., Gjermundsen, A., Graff, L. S.,
1079 ... Schulz, M. (2020). Overview of the norwegian earth system model
1080 (noresm2) and key climate response of cmip6 deck, historical, and scenario
1081 simulations. *Geoscientific Model Development*, *13*(12), 6165–6200. Re-
1082 trieved from <https://gmd.copernicus.org/articles/13/6165/2020/> doi:
1083 10.5194/gmd-13-6165-2020
- 1084 Smith, K. S., & Marshall, J. (2009). Evidence for Enhanced Eddy Mixing at Mid-
1085 depth in the Southern Ocean. *Journal of Physical Oceanography*, *39*(1),
1086 50-69. Retrieved from <https://doi.org/10.1175/2008JPO3880.1> doi:
1087 10.1175/2008JPO3880.1
- 1088 Smith, R. D., & Gent, P. R. (2004). Anisotropic gent–mcwilliams parameteriza-
1089 tion for ocean models. *Journal of Physical Oceanography*, *34*(11), 2541-2564.
1090 Retrieved from <https://doi.org/10.1175/JPO2613.1> doi: 10.1175/JPO2613
1091 .1
- 1092 Speer, K., Rintoul, S. R., & Sloyan, B. (2000). The diabatic deacon cell.
1093 *Journal of Physical Oceanography*, *30*(12), 3212 - 3222. Retrieved from
1094 [https://journals.ametsoc.org/view/journals/phoc/30/12/1520](https://journals.ametsoc.org/view/journals/phoc/30/12/1520-0485_2000_030_3212_tddc_2.0.co_2.xml)
1095 [-0485_2000_030_3212_tddc_2.0.co_2.xml](https://journals.ametsoc.org/view/journals/phoc/30/12/1520-0485_2000_030_3212_tddc_2.0.co_2.xml) doi: [https://doi.org/10.1175/](https://doi.org/10.1175/1520-0485(2000)030(3212:TDDC)2.0.CO;2)
1096 [1520-0485\(2000\)030\(3212:TDDC\)2.0.CO;2](https://doi.org/10.1175/1520-0485(2000)030(3212:TDDC)2.0.CO;2)
- 1097 Stammer, D. (1997). Global Characteristics of Ocean Variability Estimated from Re-
1098 gional TOPEX/POSEIDON Altimeter Measurements. *J. Phys. Oceanogr.*, *27*,
1099 1743–1769.
- 1100 Stanley, Z., Bachman, S. D., & Grooms, I. (2020). Vertical structure of ocean
1101 mesoscale eddies with implications for parameterizations of tracer transport.
1102 *Journal of Advances in Modeling Earth Systems*, *12*(10), e2020MS002151.
1103 Retrieved from [https://agupubs.onlinelibrary.wiley.com/doi/abs/](https://agupubs.onlinelibrary.wiley.com/doi/abs/10.1029/2020MS002151)
1104 [10.1029/2020MS002151](https://doi.org/10.1029/2020MS002151) doi: <https://doi.org/10.1029/2020MS002151>
- 1105 Stewart, A. L., Neumann, N. K., & Solodoch, A. (2023). "Eddy" saturation of the
1106 Antarctic Circumpolar Current by standing waves. *J. Phys. Oceanogr.* doi: 10
1107 .1175/JPO-D-22-0154.1
- 1108 Stewart, K., Spence, P., Waterman, S., Sommer, J. L., Molines, J.-M., Lilly, J., &
1109 England, M. (2015). Anisotropy of eddy variability in the global ocean. *Ocean*
1110 *Modelling*, *95*, 53-65. Retrieved from [https://www.sciencedirect.com/](https://www.sciencedirect.com/science/article/pii/S1463500315001638)
1111 [science/article/pii/S1463500315001638](https://www.sciencedirect.com/science/article/pii/S1463500315001638) doi: [https://doi.org/10.1016/](https://doi.org/10.1016/j.ocemod.2015.09.005)
1112 [j.ocemod.2015.09.005](https://doi.org/10.1016/j.ocemod.2015.09.005)
- 1113 Stone, P. (1972). A simplified radiative-dynamical model for the static stability of
1114 rotating atmospheres. *J. Atmos. Sci.*, *29*, 405-418.
- 1115 Sutyrin, G. G., Radko, T., & Nycander, J. (2021). Steady radiating baroclinic vor-
1116 tices in vertically sheared flows. *Physics of Fluids*, *33*(3), 031705. Retrieved
1117 from <https://doi.org/10.1063/5.0040298> doi: 10.1063/5.0040298
- 1118 Trenberth, K. E., Zhang, Y., Fasullo, J. T., & Cheng, L. (2019). Observa-
1119 tion-based estimates of global and basin ocean meridional heat transport time
1120 series. *Journal of Climate*, *32*(14), 4567 - 4583. Retrieved from [https://](https://journals.ametsoc.org/view/journals/clim/32/14/jcli-d-18-0872.1.xml)
1121 journals.ametsoc.org/view/journals/clim/32/14/jcli-d-18-0872.1.xml
1122 doi: <https://doi.org/10.1175/JCLI-D-18-0872.1>
- 1123 Trodahl, M., & Isachsen, P. E. (2018). Topographic influence on baroclinic insta-
1124 bility and the mesoscale eddy field in the northern north atlantic ocean and
1125 the nordic seas. *Journal of Physical Oceanography*, *48*(11), 2593 - 2607. Re-
1126 trieved from [https://journals.ametsoc.org/view/journals/phoc/48/11/](https://journals.ametsoc.org/view/journals/phoc/48/11/jpo-d-17-0220.1.xml)
1127 [jpo-d-17-0220.1.xml](https://journals.ametsoc.org/view/journals/phoc/48/11/jpo-d-17-0220.1.xml) doi: 10.1175/JPO-D-17-0220.1
- 1128 Tsujino, H., Urakawa, L. S., Griffies, S. M., Danabasoglu, G., Adcroft, A. J., Ama-
1129 ral, A. E., ... Yu, Z. (2020). Evaluation of global ocean–sea-ice model simula-
1130 tions based on the experimental protocols of the ocean model intercomparison

- 1131 project phase 2 (omip-2). *Geoscientific Model Development*, 13(8), 3643–3708.
 1132 Retrieved from <https://gmd.copernicus.org/articles/13/3643/2020/>
 1133 doi: 10.5194/gmd-13-3643-2020
- 1134 Uchida, T., Jamet, Q., Dewar, W. K., Le Sommer, J., Penduff, T., & Balwada, D.
 1135 (2022). Diagnosing the thickness-weighted averaged eddy-mean flow interaction
 1136 from an eddying north atlantic ensemble: The eliasen-palm flux. *Journal*
 1137 *of Advances in Modeling Earth Systems*, 14(5), e2021MS002866. Retrieved
 1138 from [https://agupubs.onlinelibrary.wiley.com/doi/abs/10.1029/](https://agupubs.onlinelibrary.wiley.com/doi/abs/10.1029/2021MS002866)
 1139 [2021MS002866](https://doi.org/10.1029/2021MS002866) (e2021MS002866 2021MS002866) doi: [https://doi.org/10.1029/](https://doi.org/10.1029/2021MS002866)
 1140 [2021MS002866](https://doi.org/10.1029/2021MS002866)
- 1141 Vallis, G., & Maltrud, M. E. (1993). Generation of mean flows and jets on a beta-
 1142 plane and over topography. *J. Phys. Oceanogr.*, 23, 1346-1362.
- 1143 Visbeck, M., Marshall, J., Haine, T., & Spall, M. (1997). Specification of eddy trans-
 1144 fer coefficients in coarse-resolution ocean circulation models. *Journal of Physi-*
 1145 *cal Oceanography*, 27(3), 381-402. Retrieved from [https://doi.org/10.1175/](https://doi.org/10.1175/1520-0485(1997)027<0381:SOETCI>2.0.CO;2)
 1146 [1520-0485\(1997\)027<0381:SOETCI>2.0.CO;2](https://doi.org/10.1175/1520-0485(1997)027(0381:SOETCI)2.0.CO;2) doi: [10.1175/1520-0485\(1997\)](https://doi.org/10.1175/1520-0485(1997)027(0381:SOETCI)2.0.CO;2)
 1147 [027\(0381:SOETCI\)2.0.CO;2](https://doi.org/10.1175/1520-0485(1997)027(0381:SOETCI)2.0.CO;2)
- 1148 Wang, Y., & Stewart, A. L. (2018). Eddy dynamics over continental slopes
 1149 under retrograde winds: Insights from a model inter-comparison. *Ocean*
 1150 *Modelling*, 121, 1-18. Retrieved from [https://www.sciencedirect.com/](https://www.sciencedirect.com/science/article/pii/S146350031730183X)
 1151 [science/article/pii/S146350031730183X](https://www.sciencedirect.com/science/article/pii/S146350031730183X) doi: [https://doi.org/10.1016/](https://doi.org/10.1016/j.ocemod.2017.11.006)
 1152 [j.ocemod.2017.11.006](https://doi.org/10.1016/j.ocemod.2017.11.006)
- 1153 Wang, Y., & Stewart, A. L. (2020). Scalings for eddy buoyancy transfer across
 1154 continental slopes under retrograde winds. *Ocean Modelling*, 147, 101579.
 1155 Retrieved from [https://www.sciencedirect.com/science/article/pii/](https://www.sciencedirect.com/science/article/pii/S1463500319301775)
 1156 [S1463500319301775](https://www.sciencedirect.com/science/article/pii/S1463500319301775) doi: <https://doi.org/10.1016/j.ocemod.2020.101579>
- 1157 Wei, H., & Wang, Y. (2021). Full-depth scalings for isopycnal eddy mixing across
 1158 continental slopes under upwelling-favorable winds. *Journal of Advances in*
 1159 *Modeling Earth Systems*, 13(6), e2021MS002498. Retrieved from [https://](https://agupubs.onlinelibrary.wiley.com/doi/abs/10.1029/2021MS002498)
 1160 [agupubs.onlinelibrary.wiley.com/doi/abs/10.1029/2021MS002498](https://doi.org/10.1029/2021MS002498) doi:
 1161 <https://doi.org/10.1029/2021MS002498>
- 1162 Wei, H., Wang, Y., Stewart, A. L., & Mak, J. (2022). Scalings for eddy
 1163 buoyancy fluxes across prograde shelf/slope fronts. *Journal of Ad-*
 1164 *vances in Modeling Earth Systems*, 14(12), e2022MS003229. Retrieved
 1165 from [https://agupubs.onlinelibrary.wiley.com/doi/abs/10.1029/](https://agupubs.onlinelibrary.wiley.com/doi/abs/10.1029/2022MS003229)
 1166 [2022MS003229](https://doi.org/10.1029/2022MS003229) (e2022MS003229 2022MS003229) doi: [https://doi.org/10.1029/](https://doi.org/10.1029/2022MS003229)
 1167 [2022MS003229](https://doi.org/10.1029/2022MS003229)
- 1168 Woodgate, R. A. (2018). Increases in the pacific inflow to the arctic from 1990 to
 1169 2015, and insights into seasonal trends and driving mechanisms from year-
 1170 round bering strait mooring data. *Progress in Oceanography*, 160, 124-154.
 1171 Retrieved from [https://www.sciencedirect.com/science/article/pii/](https://www.sciencedirect.com/science/article/pii/S0079661117302215)
 1172 [S0079661117302215](https://www.sciencedirect.com/science/article/pii/S0079661117302215) doi: <https://doi.org/10.1016/j.pocean.2017.12.007>
- 1173 Woodgate, R. A., Stafford, K. M., & Prah, F. G. (2015). A synthesis of
 1174 year-round interdisciplinary mooring measurements in the bering strait
 1175 (1990–2014) and the rusalca years (2004–2011). *Oceanography*. Retrieved
 1176 from <https://doi.org/10.5670/oceanog.2015.57>
- 1177 Wunsch, C. (1997). The vertical partition of oceanic horizontal kinetic energy. *J.*
 1178 *Phys. Oceanogr.*, 27, 1770–1794.
- 1179 Xu, X., Chassignet, E. P., Firing, Y. L., & Donohue, K. (2020). Antarctic cir-
 1180 cumpolar current transport through drake passage: What can we learn from
 1181 comparing high-resolution model results to observations? *Journal of Geophys-*
 1182 *ical Research: Oceans*, 125(7), e2020JC016365. Retrieved from [https://](https://agupubs.onlinelibrary.wiley.com/doi/abs/10.1029/2020JC016365)
 1183 [agupubs.onlinelibrary.wiley.com/doi/abs/10.1029/2020JC016365](https://doi.org/10.1029/2020JC016365)
 1184 (e2020JC016365 2020JC016365) doi: <https://doi.org/10.1029/2020JC016365>
- 1185 Yankovsky, E., Zanna, L., & Smith, K. S. (2022). Influences of mesoscale ocean ed-

- 1186 dies on flow vertical structure in a resolution-based model hierarchy. *Journal of*
1187 *Advances in Modeling Earth Systems*, 14(11), e2022MS003203. Retrieved
1188 from [https://agupubs.onlinelibrary.wiley.com/doi/abs/10.1029/](https://agupubs.onlinelibrary.wiley.com/doi/abs/10.1029/2022MS003203)
1189 [2022MS003203](https://agupubs.onlinelibrary.wiley.com/doi/abs/10.1029/2022MS003203) (e2022MS003203 2022MS003203) doi: [https://doi.org/10.1029/](https://doi.org/10.1029/2022MS003203)
1190 [2022MS003203](https://doi.org/10.1029/2022MS003203)
- 1191 Zhang, W., & Wolfe, C. L. P. (2022). On the vertical structure of oceanic mesoscale
1192 tracer diffusivities. *Journal of Advances in Modeling Earth Systems*, 14(6),
1193 e2021MS002891. Retrieved from [https://agupubs.onlinelibrary.wiley](https://agupubs.onlinelibrary.wiley.com/doi/abs/10.1029/2021MS002891)
1194 [.com/doi/abs/10.1029/2021MS002891](https://agupubs.onlinelibrary.wiley.com/doi/abs/10.1029/2021MS002891) (e2021MS002891 2021MS002891) doi:
1195 <https://doi.org/10.1029/2021MS002891>
- 1196 Zweng, M. M., Reagan, J. R., Seidov, D., Boyer, T. P., Locarnini, R. A., Gar-
1197 cia, H. E., . . . Smolyar, I. (2018). *World ocean atlas 2018, volume 2:*
1198 *Salinity. a. mishonov technical ed.* NOAA Atlas NESDIS 82, 50pp. Re-
1199 trieved from [https://www.ncei.noaa.gov/sites/default/files/2022-06/](https://www.ncei.noaa.gov/sites/default/files/2022-06/woa18_vol2.pdf)
1200 [woa18_vol2.pdf](https://www.ncei.noaa.gov/sites/default/files/2022-06/woa18_vol2.pdf)

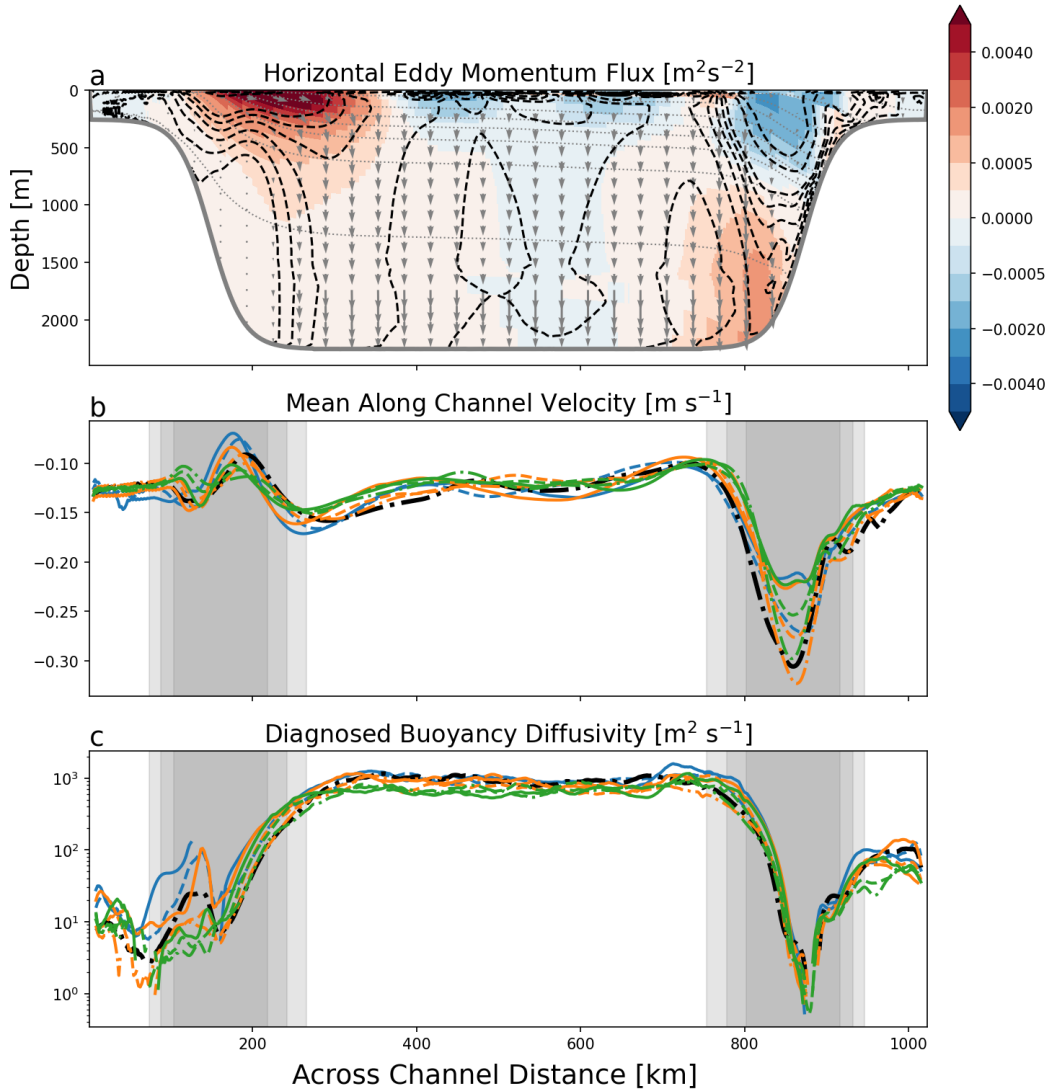


Figure 1. Cross section of zonally and temporally-averaged (a) horizontal eddy momentum flux (shading), E-P flux (gray arrows), mean velocity (dashed black contours), and mean density (dotted gray contours), (b) vertically-averaged along-channel velocity and (c) vertically-averaged meridional buoyancy (temperature) diffusivity. In panels b and c we indicate stratification by color (in descending order: blue, orange, green) and slope width (steepness) by line-style (in descending order: dashed-dotted, dashed, solid). The black line is experiment 3 (Table 2) and corresponds to the case shown in panel a. Gray shading shows the location of the slope regions in the different simulations (where $300m < H < 2250m$). For some of the simulations the diffusivity lines are broken because of negative diffusivities that are not shown on the log scale.

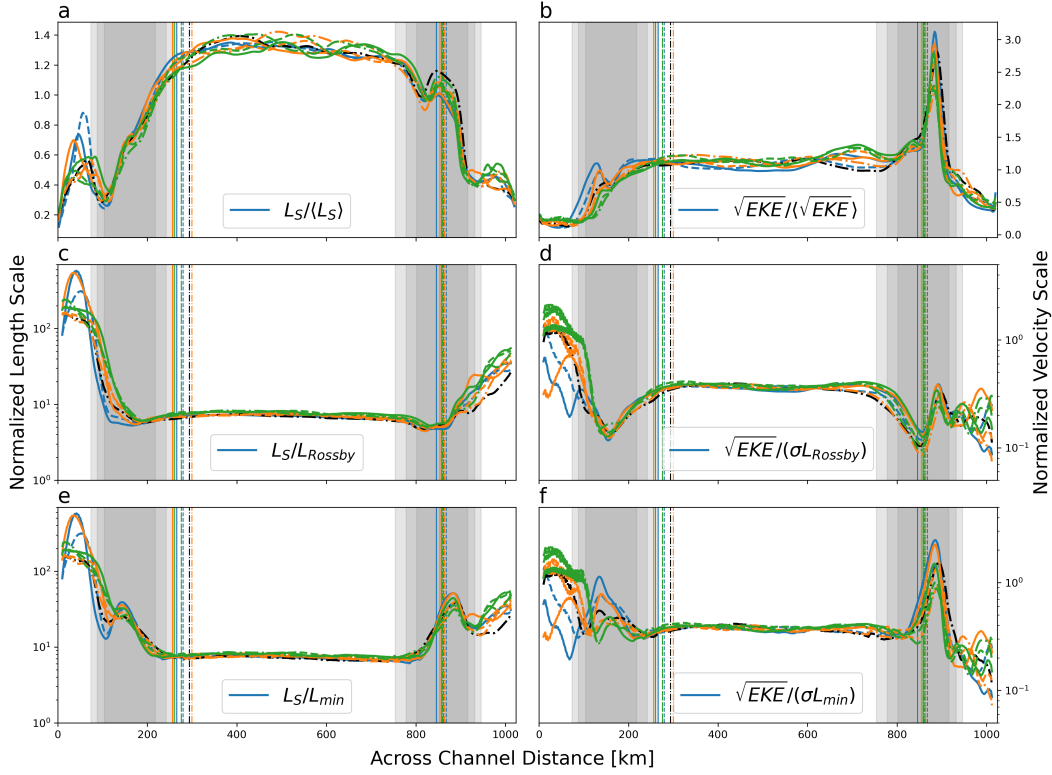


Figure 2. Diagnosed length scales (panels on the left) and velocity scales (panels on the right) for all experiments. All measures have been normalized. The top row (panels a and b) are normalized by the basin mean values. Length scales in panel c and panel e are normalized by the deformation radius and by the minimum of the deformation radius and topographic Rhines scale, respectively. In panels d and f we normalize by the parameterized velocity scale, using length scales from c and e, respectively. Colors and line styles as in Fig. 1. Gray shadings indicate the slope regions (similar to Fig. 1) and vertical lines indicate the location of maxima in depth-averaged velocity in each experiment.

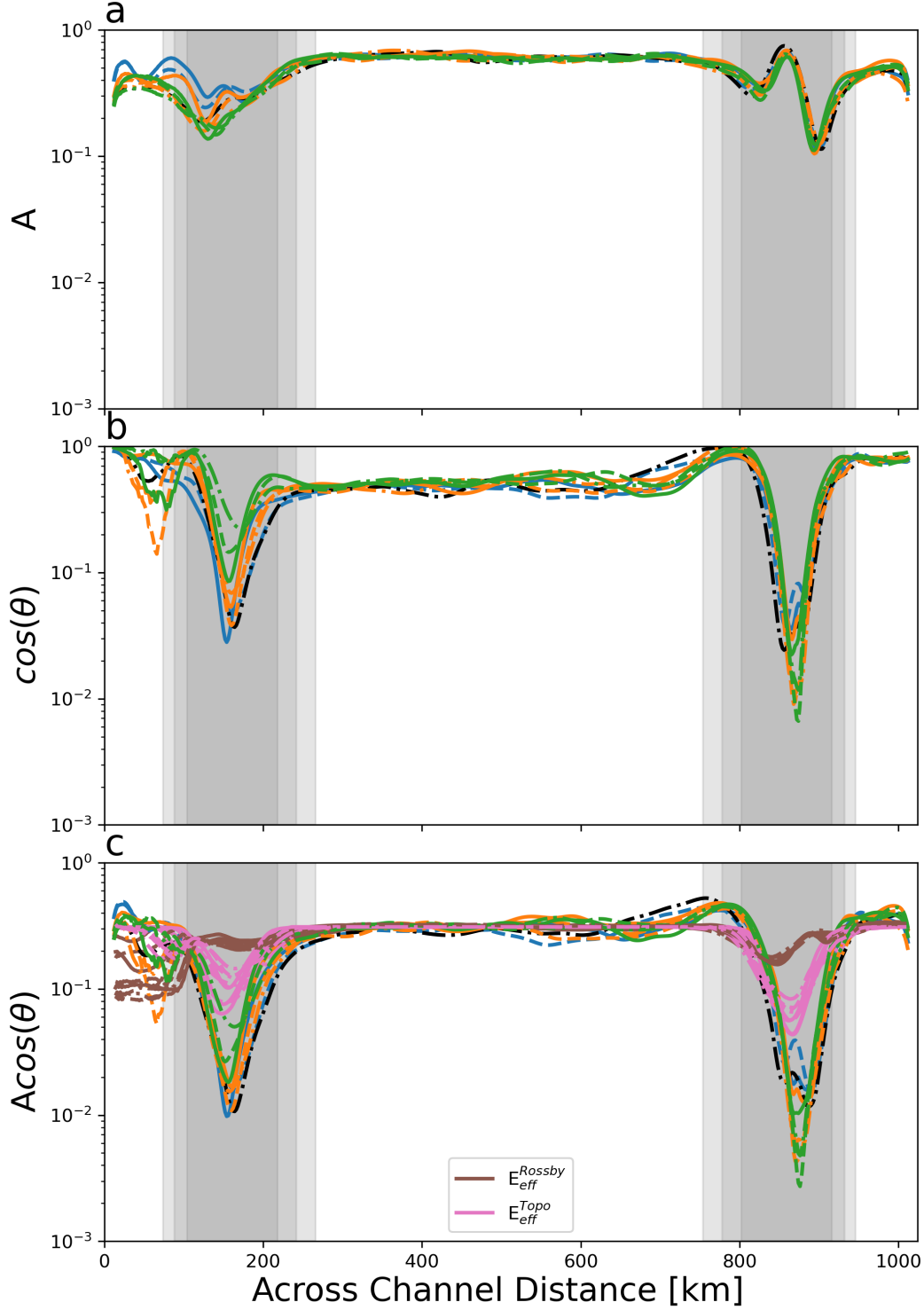


Figure 3. Measures of anisotropy and phase angle relationships: (a) eddy velocity anisotropy (A), (b) cosine of the phase angle between T' and v' and (c) the product of (a) and (b), as well as the parameterized eddy efficiency factors E_{eff} (brown when using deformation radius, pink when using the topographic Rhines scale). For the two E_{eff} estimates we use $a_2 = 10$ and $a_1 = 0.35$ and $a_1 = 0.32$, respectively, to match the mid-basin values of $A \cos(\theta)$. Colors and line styles for the diagnosed cases as in Fig. 1, and gray shadings indicate the slope regions (similar to Fig. 1)

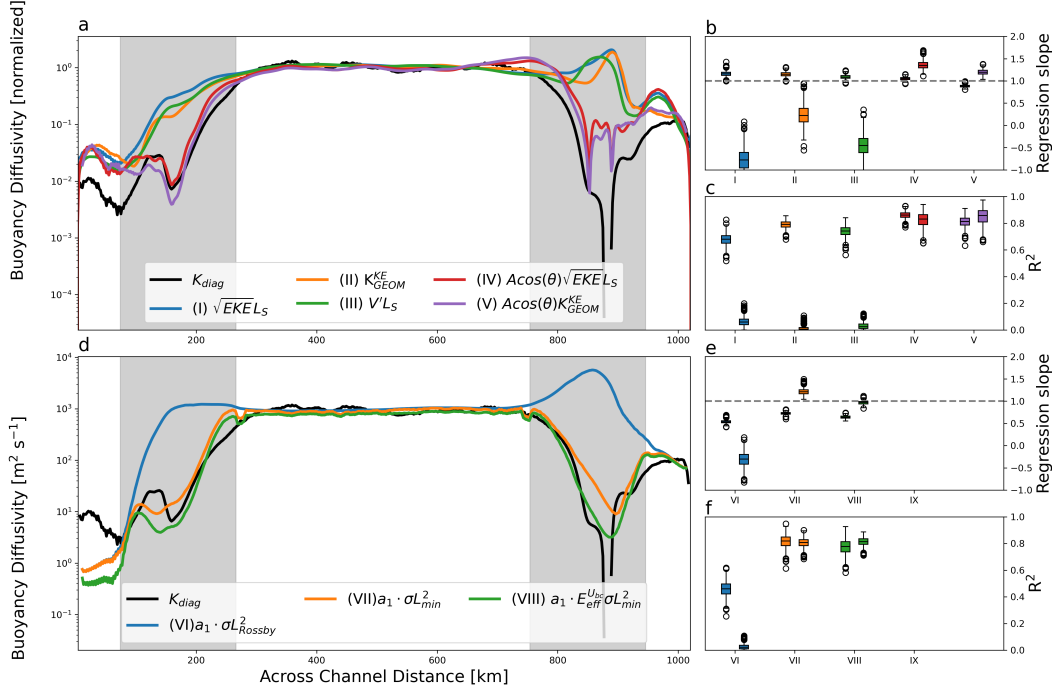


Figure 4. Partly-parameterized (a–c) and fully-parameterized (d–e) across-slope buoyancy diffusivities. The left panels show across-basin profiles for experiment 3 (Table 2) whereas the right panels summarize the statistics of linear fits between the diagnosed and parameterized diffusivities across all experiments (b–c, e–f; statistics are from a linear regression using 200 points across all cases that is repeated 5000 times). Boxes and whiskers come in pairs, with the left and right ones corresponding to the southern and northern slope, respectively. Linear regressions are done over the slope regions only (gray shading; similar to Fig. 1). Panel a shows diffusivities normalized by their basin mean value, whereas panel d shows absolute values. In panel d, $a_1 = 0.25$ for estimate VI, for VII–VIII $a_1 = 0.02$, and in VIII $a_2 = 10$.

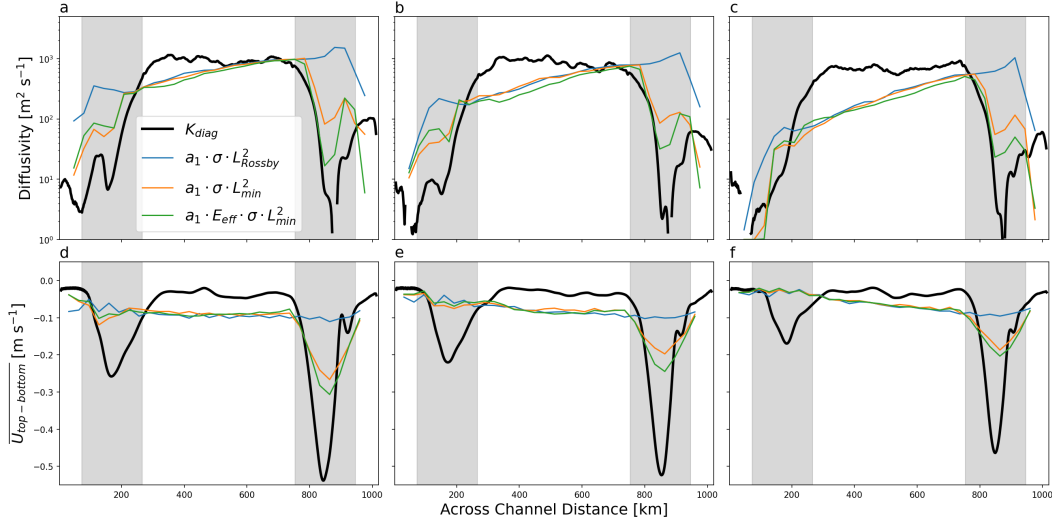


Figure 5. Buoyancy diffusivity (top panels) and top-to-bottom thermal wind shear (lower panels) in the coarse-resolution channel simulation compared to the high-resolution simulation (thick black line). The different columns are separated by stratification such that the initial conditions are the same as for Exp 3, 6 and 9 in the left, middle and right columns, respectively.

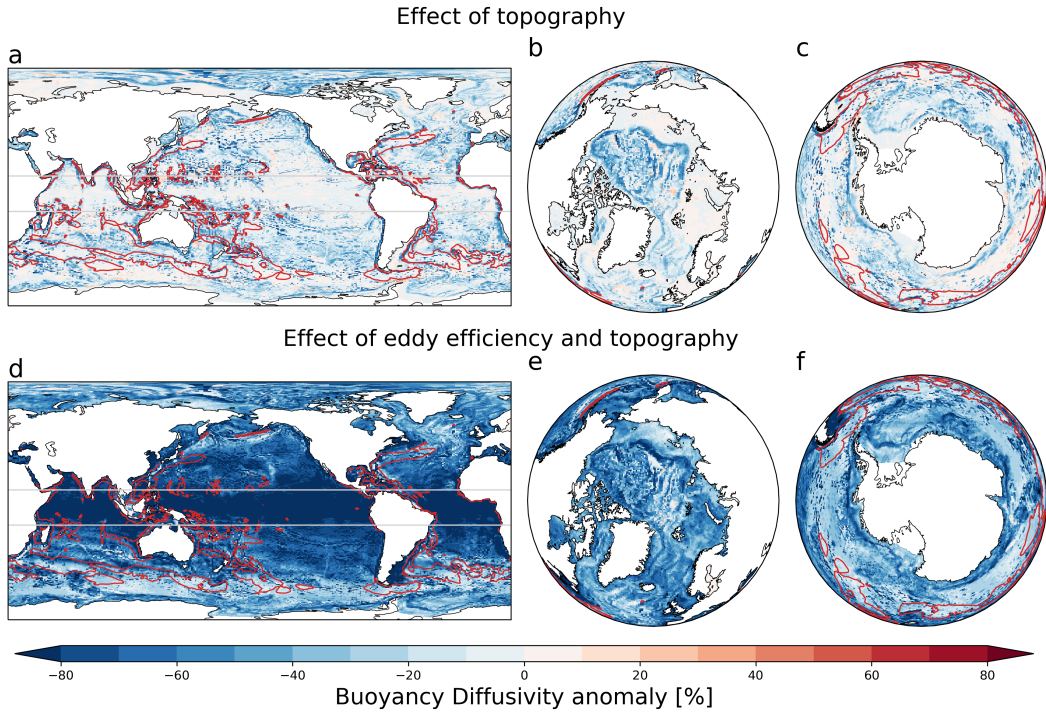


Figure 6. Anomalies from the control case in parameterized (depth-averaged) GM diffusivity due to implementation of (top row) the topographic Rhines scale and (bottom row) eddy efficiency in addition to the topographic Rhines scale. Red contours show the $1000 \text{ m}^2 \text{ s}^{-1}$ isoline for diffusivity in the control case and light gray contours show areas in the tropics where the grid size is smaller than the internal deformation radius and therefore the resolution function (Hallberg, 2013) reducing the GM coefficient is in effect.

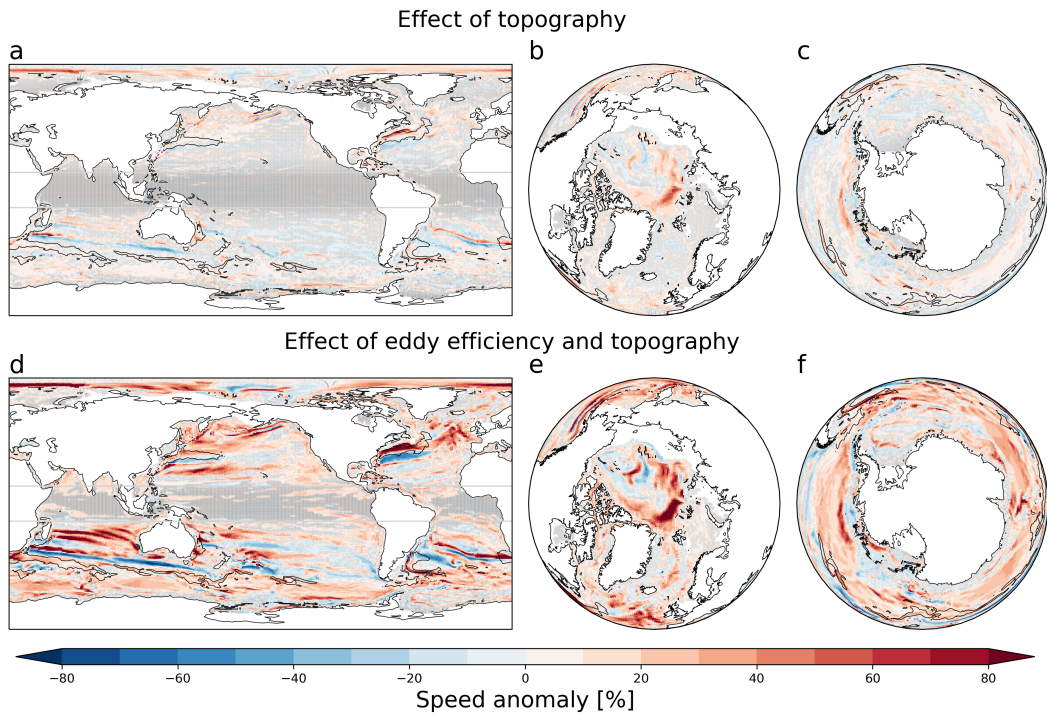


Figure 7. Flow speed anomalies from the control case at 100–200 m depth due to implementation of: (top row) the topographic Rhines scale and (bottom row) eddy efficiency in addition to the topographic Rhines scale. Black contours show the 0.25 m s^{-1} isolines for observational estimate of the quasi-geostrophic current speed (Buongiorno Nardelli, 2020) in the same 100–200 m depth interval. Gray dots mark grid cells where the mean difference from the control case is not significant at the 5% level (student’s t-test).

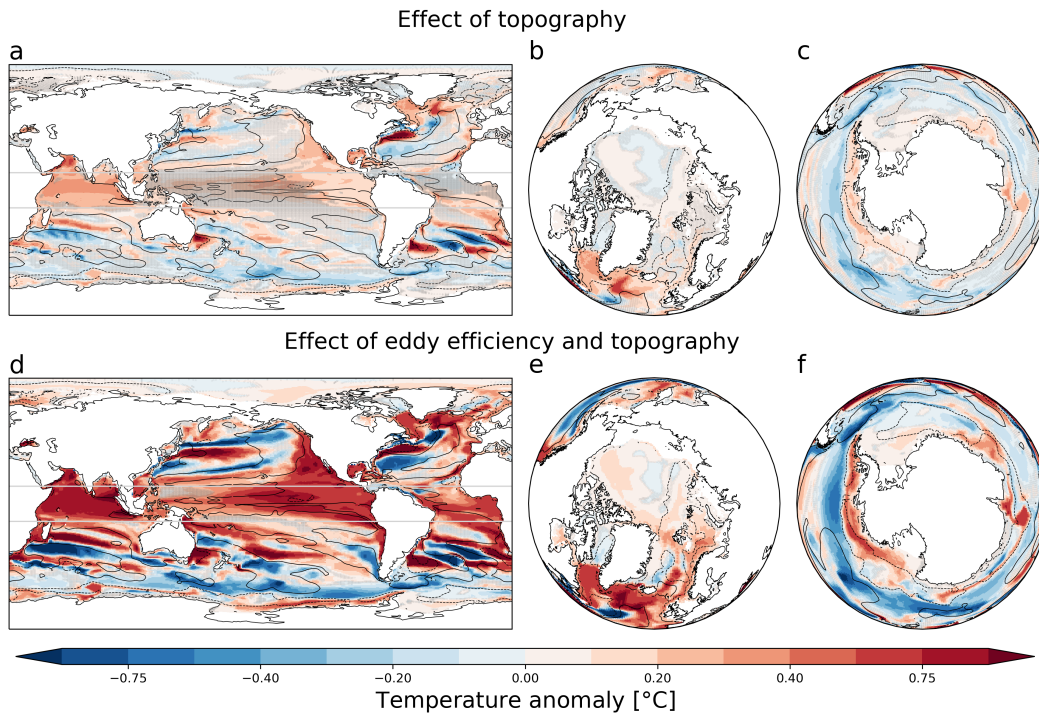


Figure 8. Temperature anomalies from the control case in resolved temperature field between 100–200 m depth due to implementation of: (top row) the topographic Rhines scale and (bottom row) eddy efficiency in addition to the topographic Rhines scale. Black contours show the $\pm 1^\circ\text{C}$ (solid/dashed) isoline for the control case bias relative to the WOA observations. Therefore, whenever solid (dashed) contours surrounds blue (red) areas the bias is reduced. Gray dots mark grid cells where the mean difference from the control case is not significant at the 5% level (student's t-test).

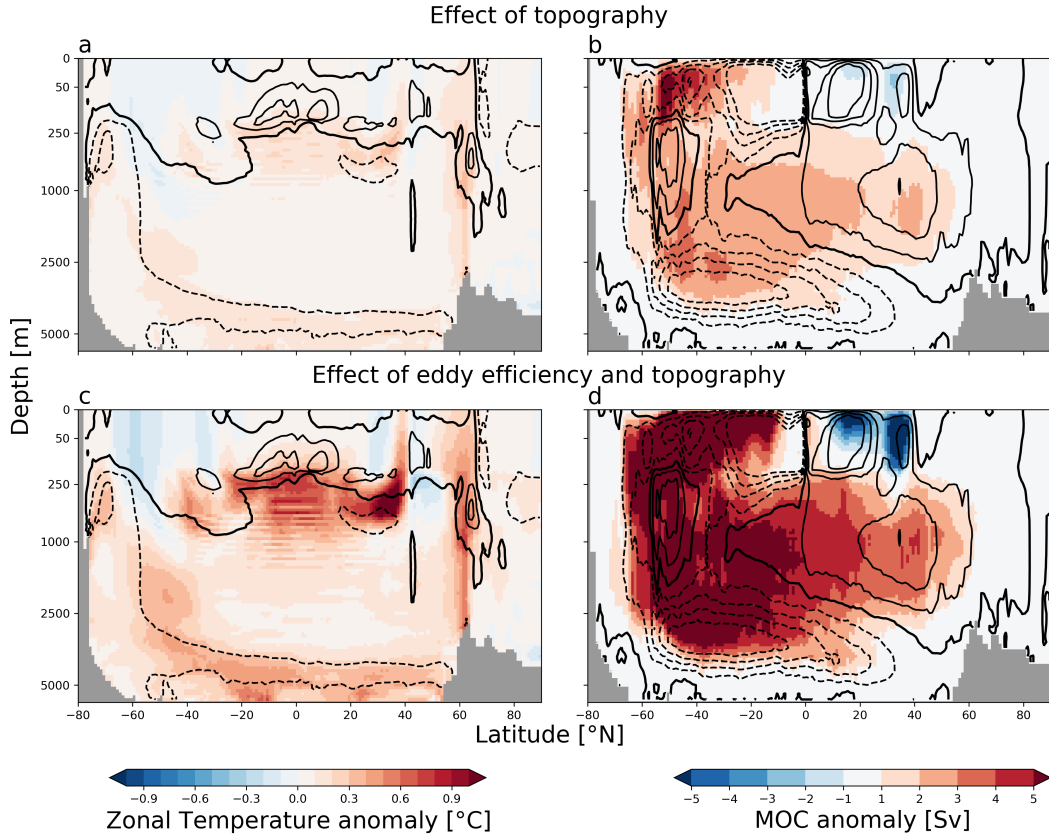


Figure 9. Zonal-mean temperature anomalies (left panels) and global meridional overturning stream function anomalies (right panels), relative to the control simulation, due to implementation of: (top row) the topographic Rhines scale and (bottom row) eddy efficiency in addition to the topographic Rhines scale. For temperature, black contours show the control case bias relative to the WOA observations in 0.25°C intervals (dashed for negative, solid for positive, the thick solid curve shows the zero contour). Therefore, whenever solid (dashed) contours surround blue (red) areas the bias to the observations is reduced. For MOC the contours show the control case MOC at 5 Sv intervals with the thick solid curve indicating the 0 Sv contour. Therefore solid (dashed) contours surrounding red (blue) indicates intensifying overturning.

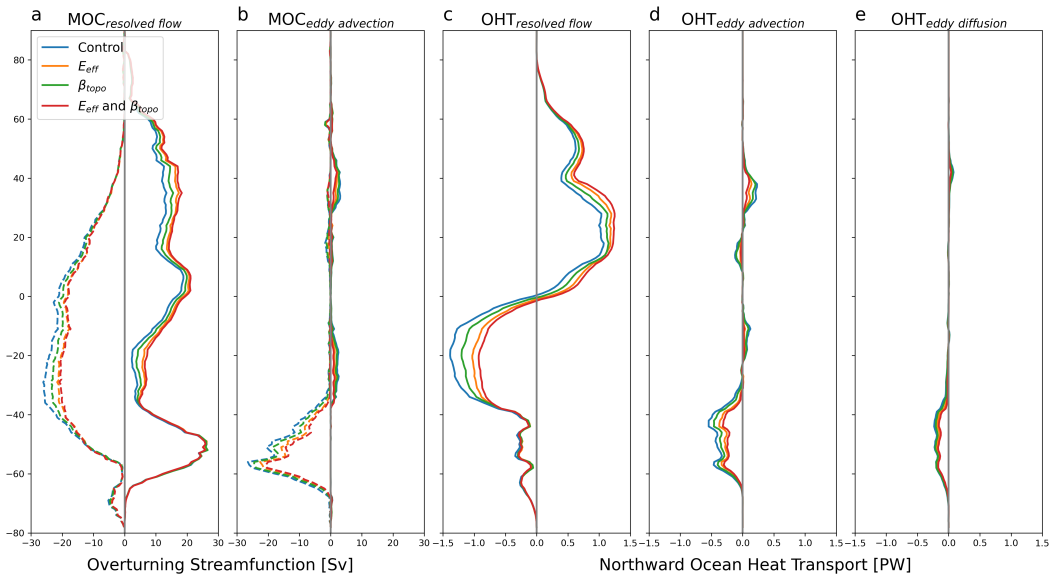


Figure 10. Resolved and eddy contributions to the global meridional overturning circulation (MOC, panels a and b) and to the global northward ocean heat transport (OHT, panels c–e). For the MOC we show the maximum (solid) and minimum (dashed) below 500 m to avoid the shallow surface overturning cells. For the OHT we show both advective and diffusive eddy contributions (panels d and e, respectively).

Figure 1.

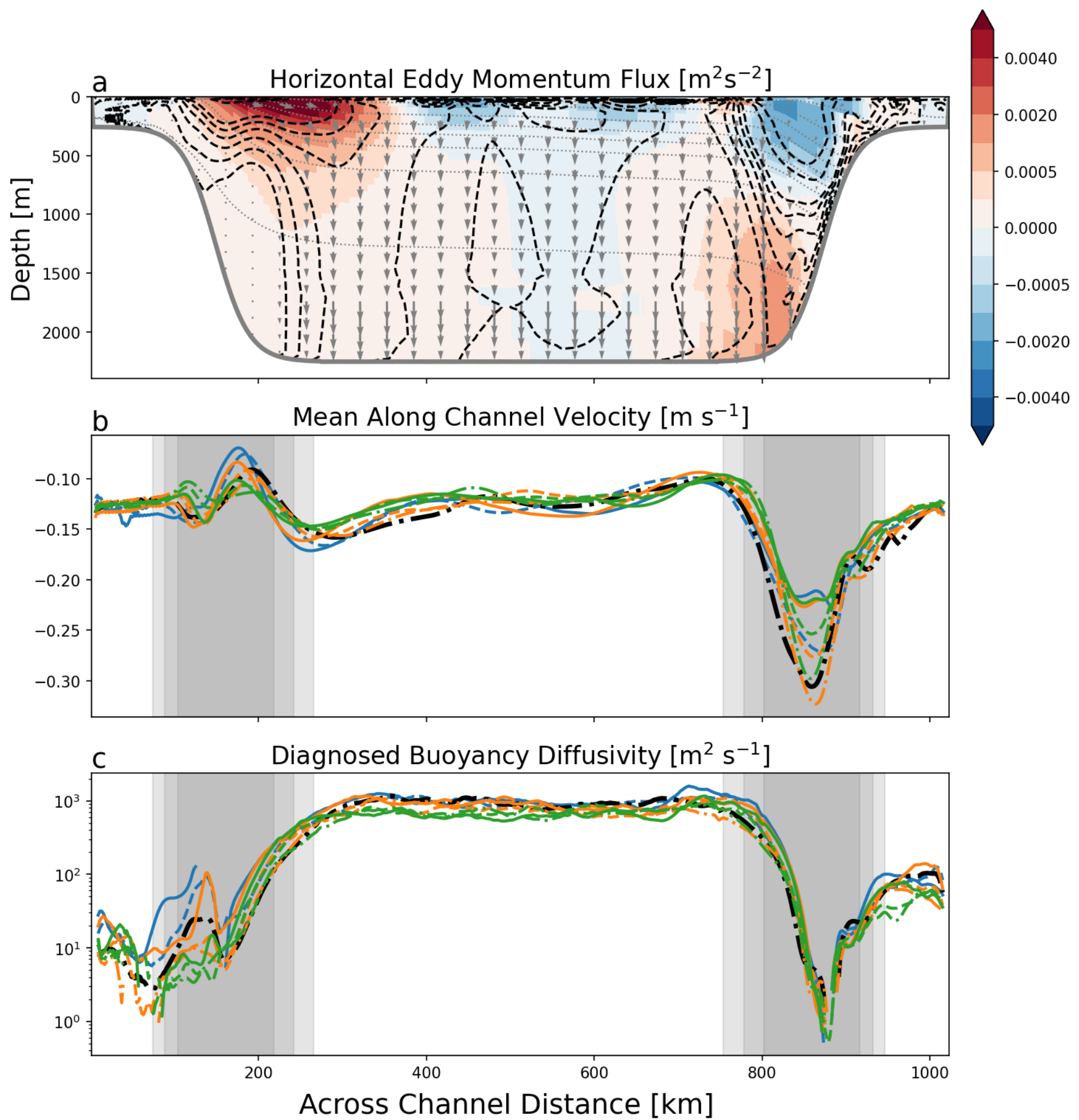


Figure 2.

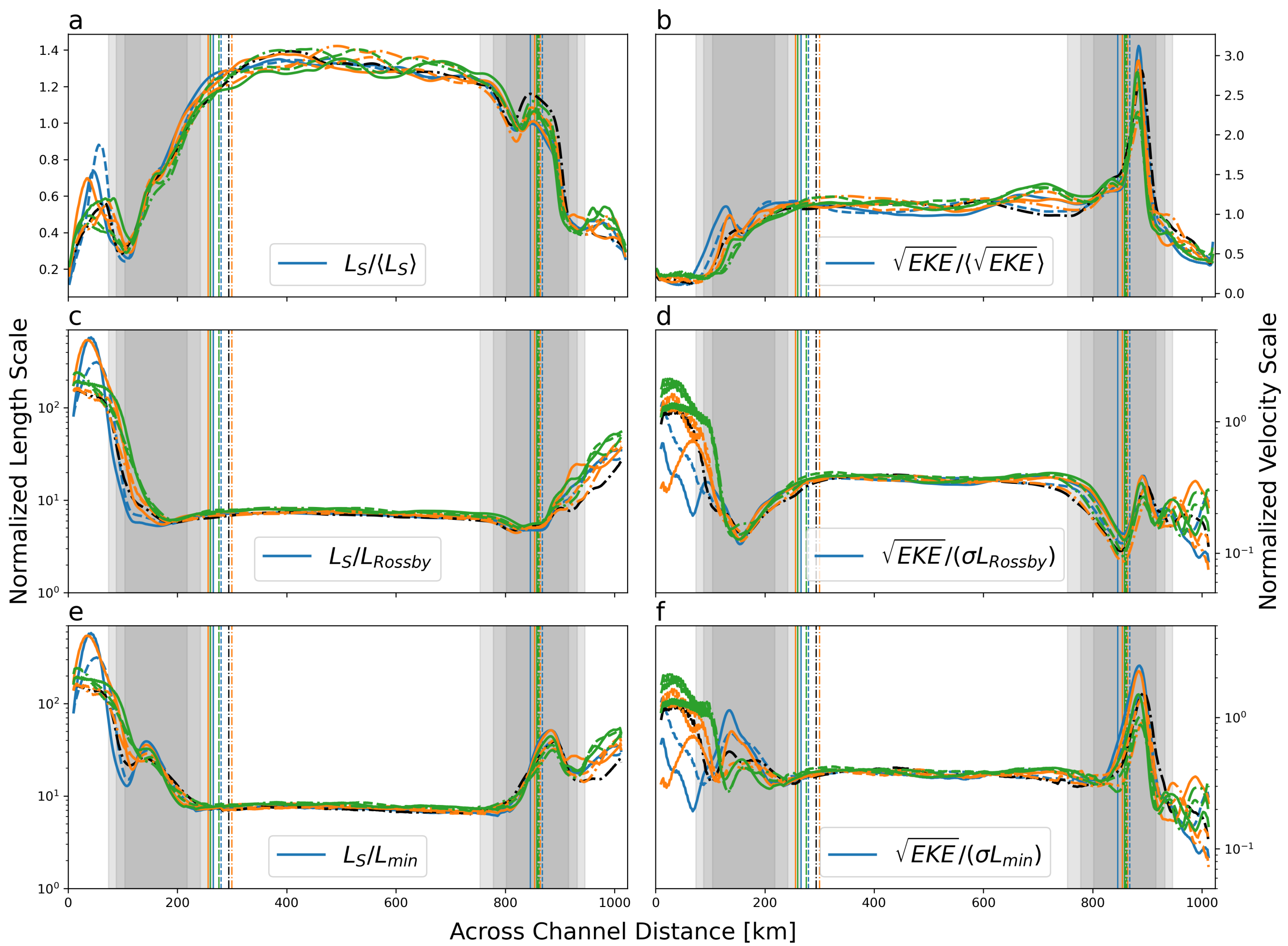


Figure 3.

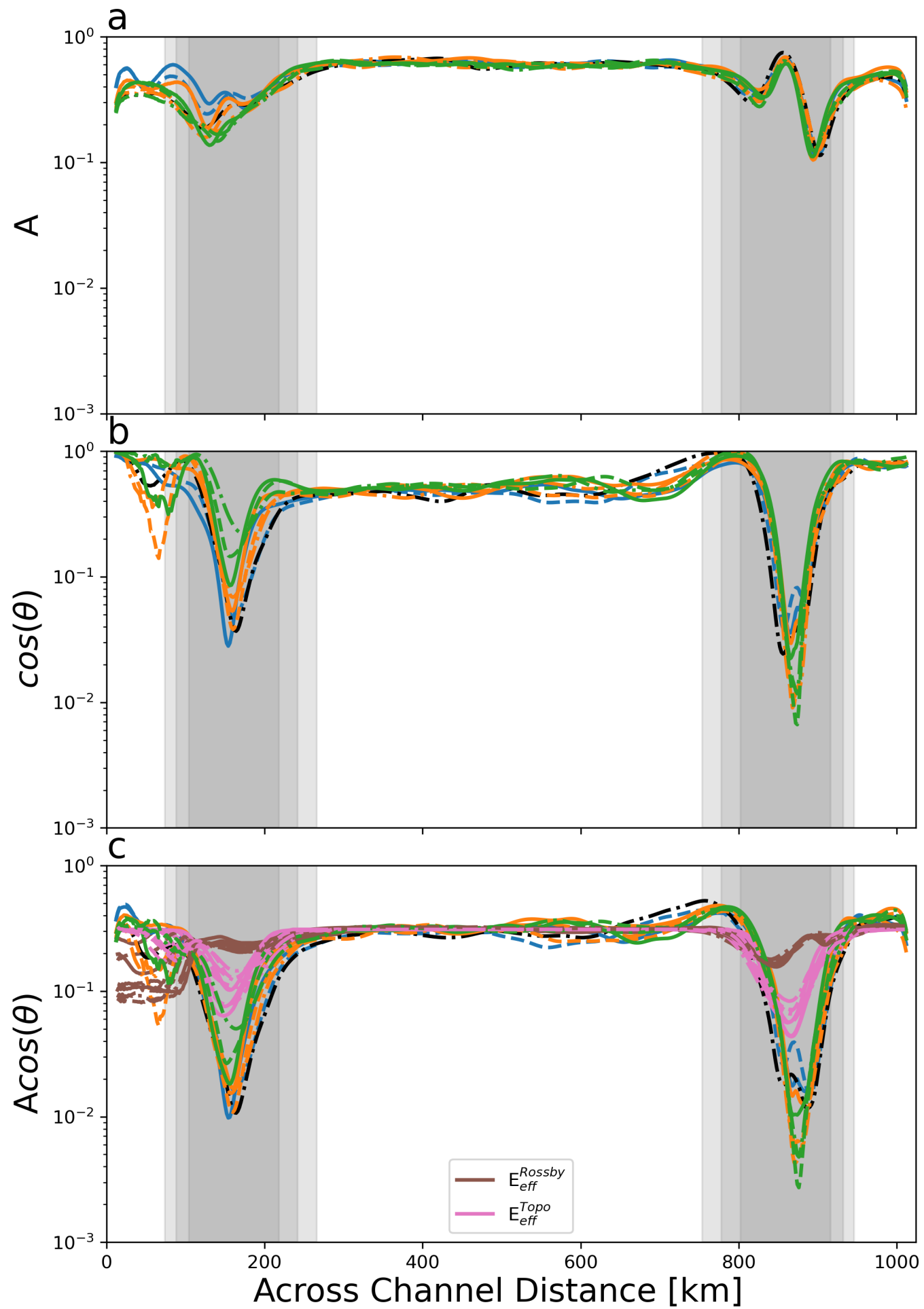
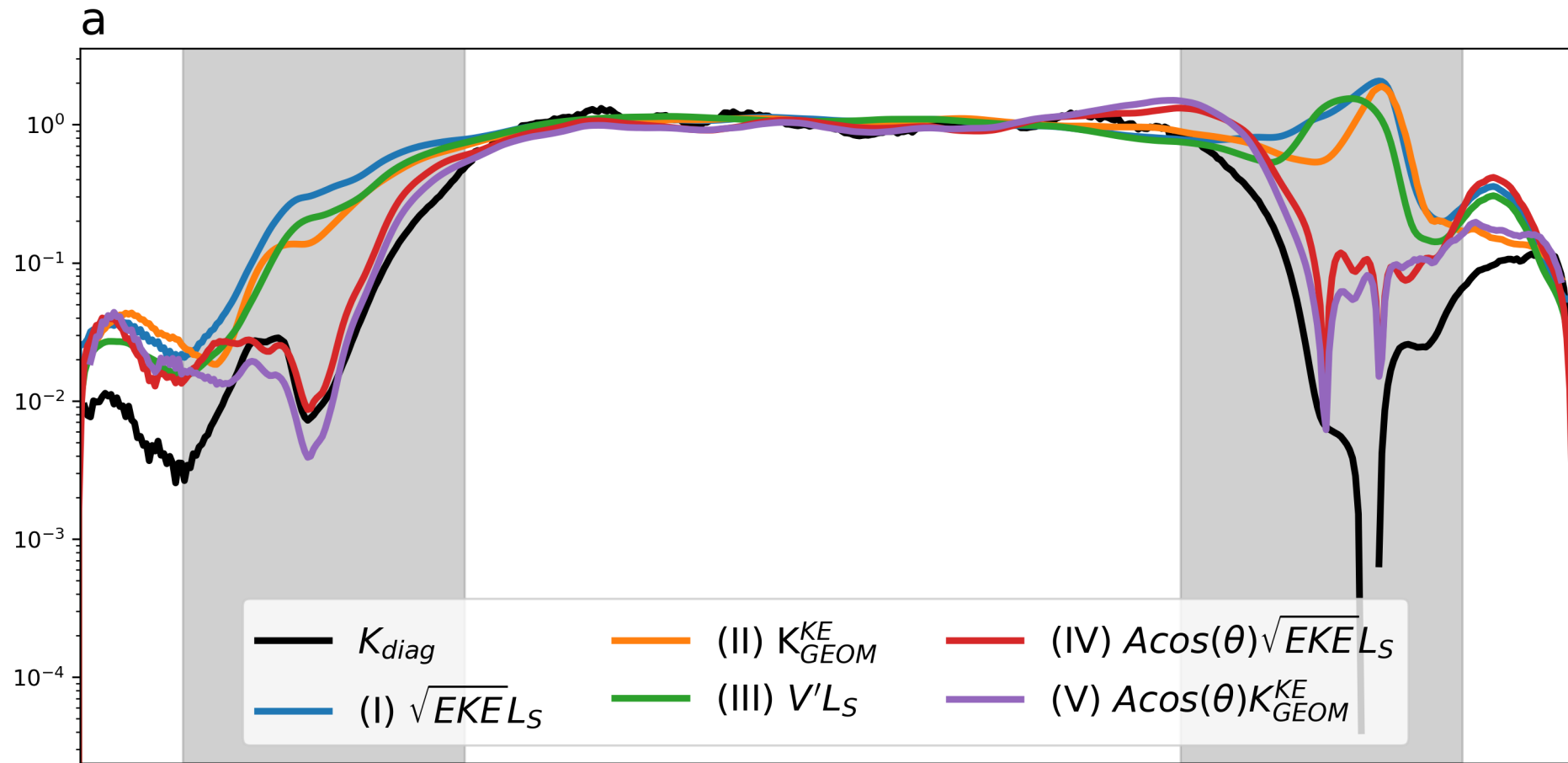
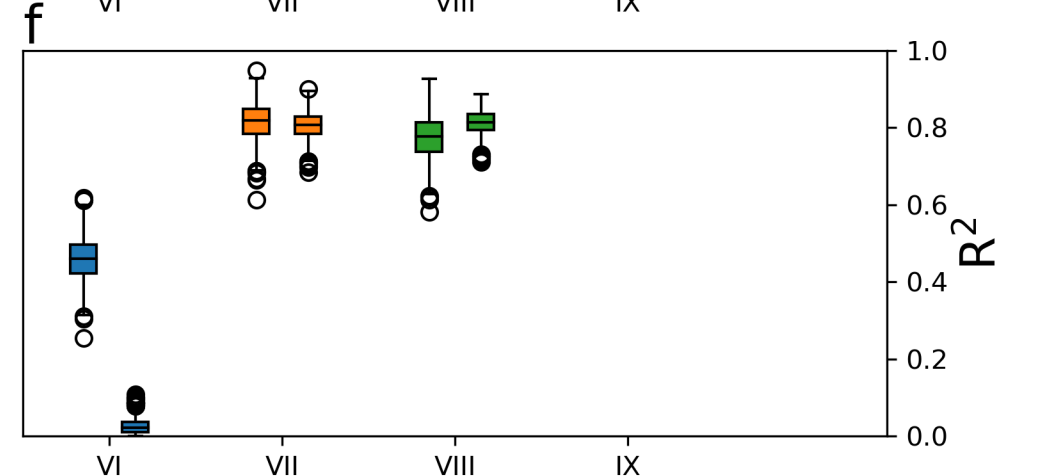
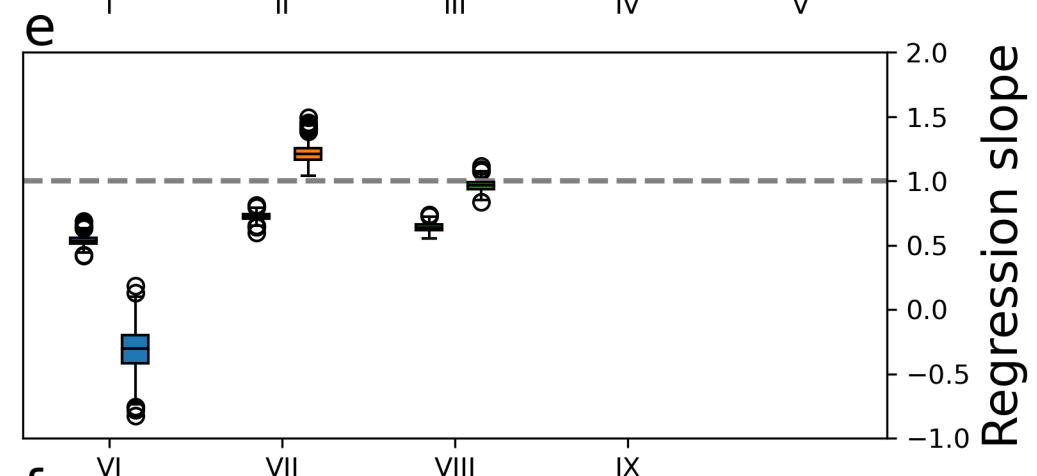
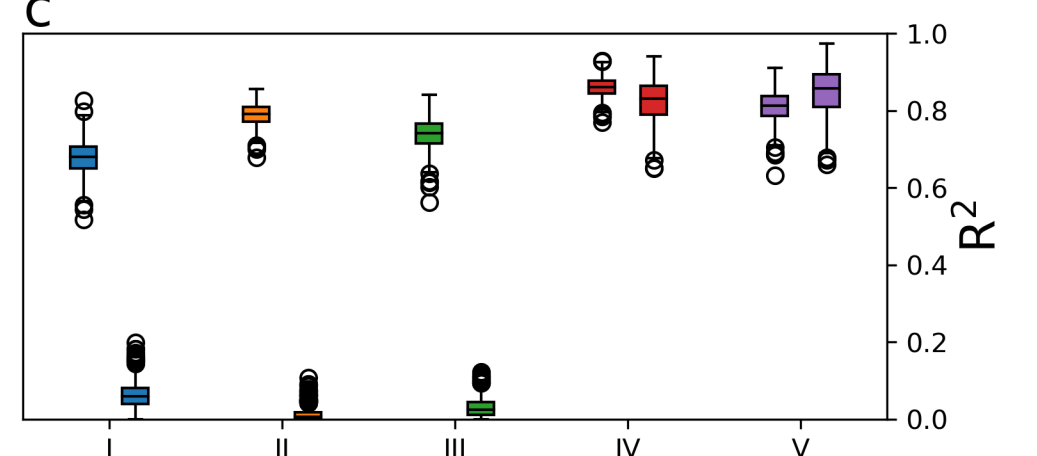
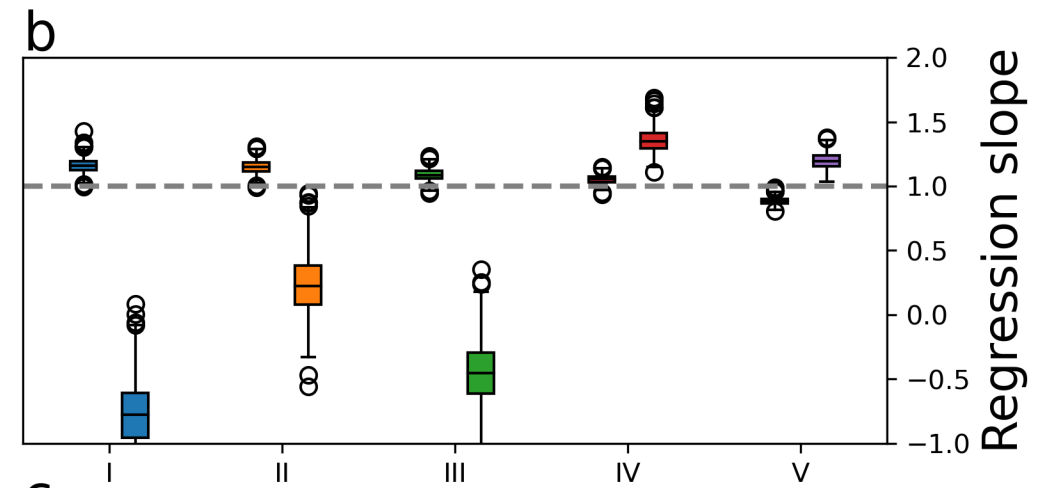
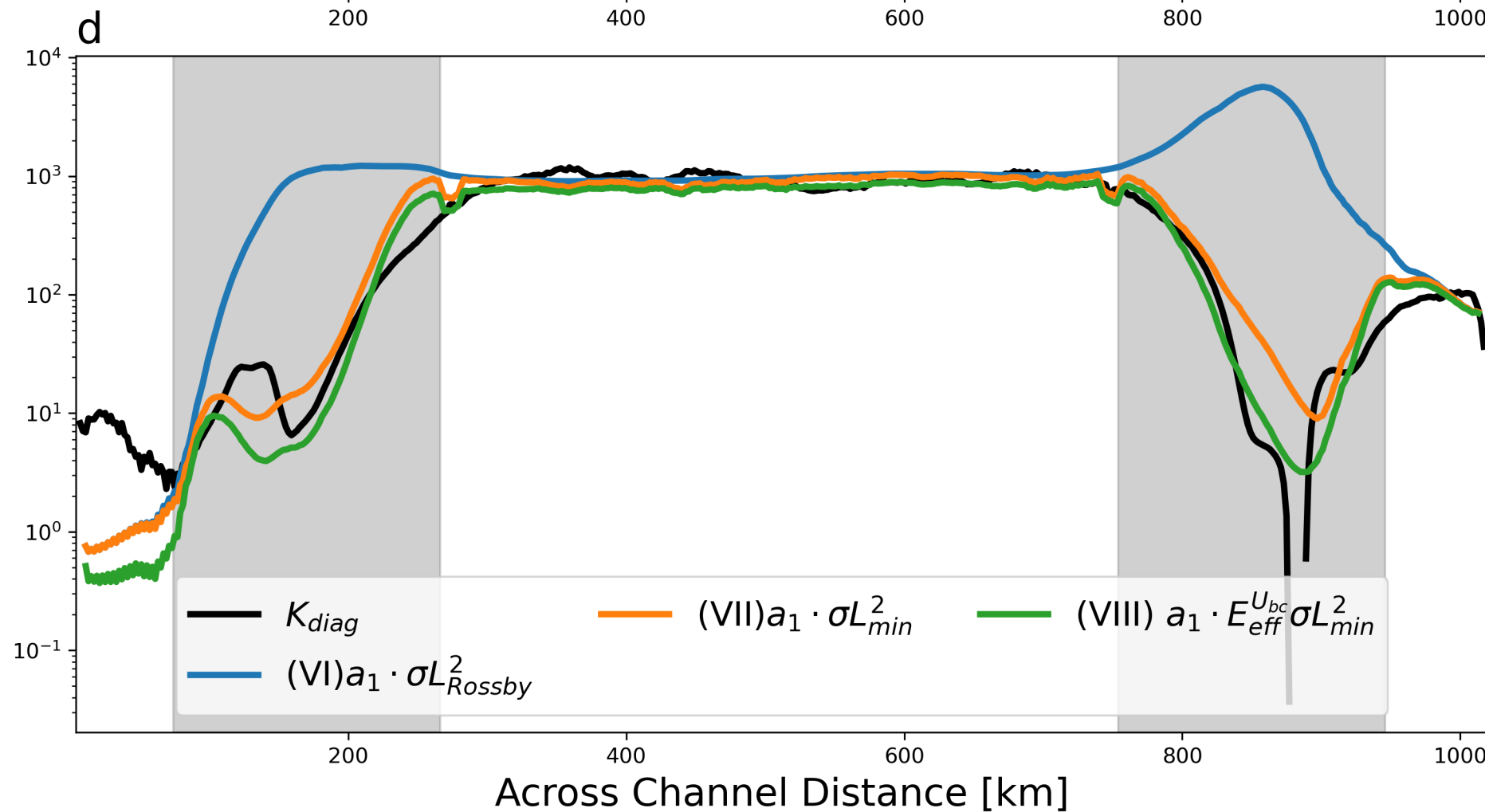


Figure 4.

Buoyancy Diffusivity [normalized]



Buoyancy Diffusivity [$m^2 s^{-1}$]



Across Channel Distance [km]

Figure 5.

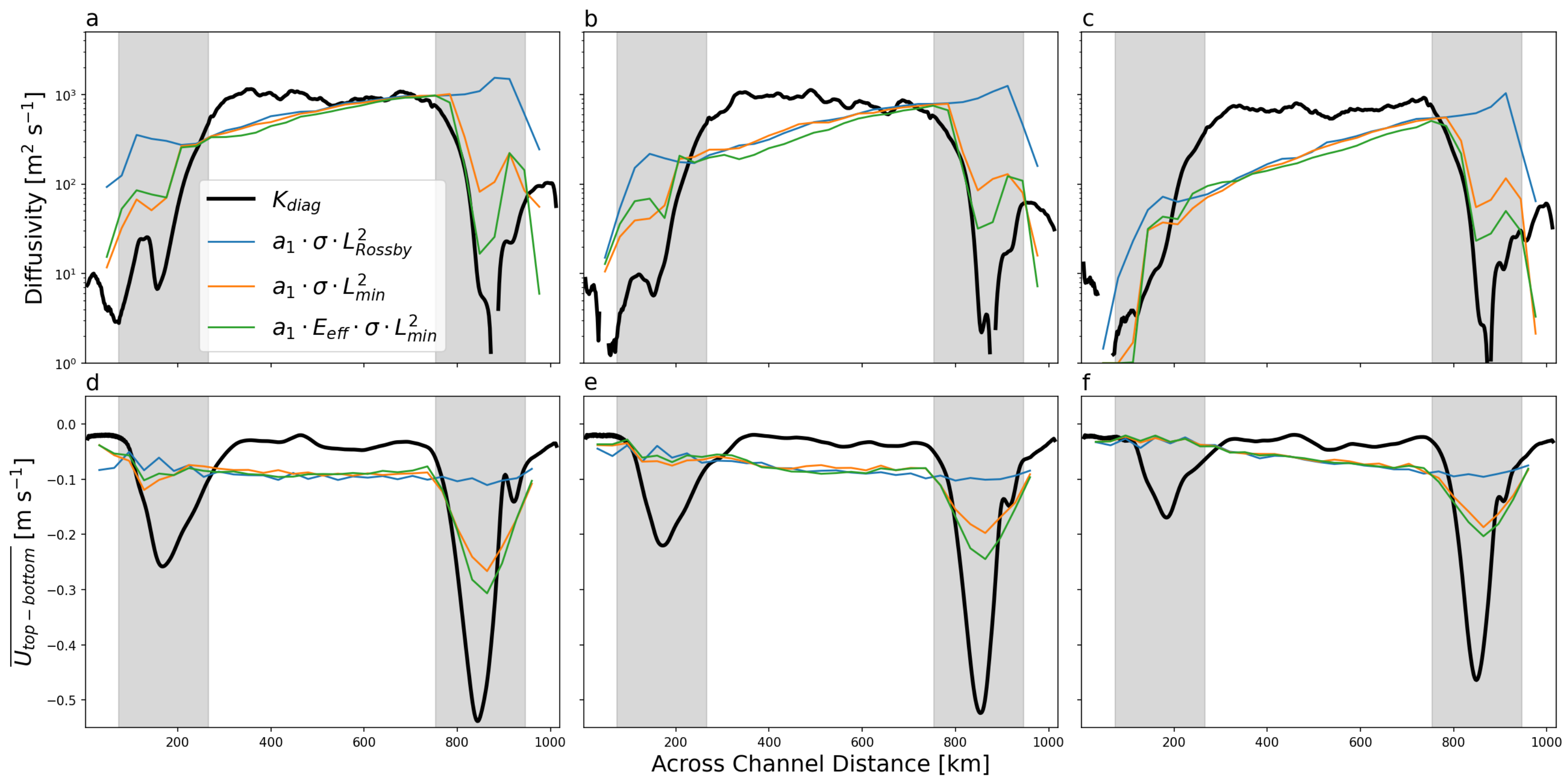
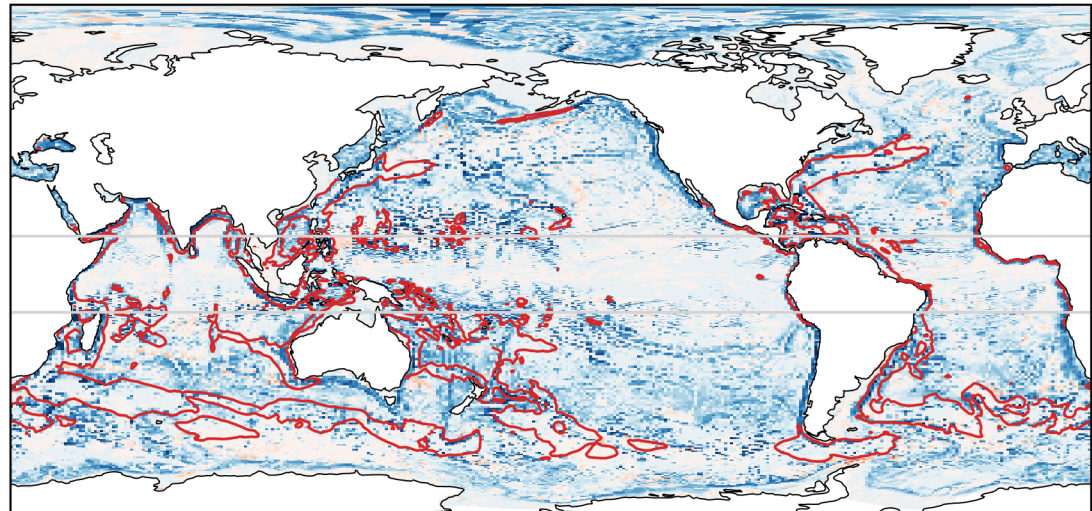


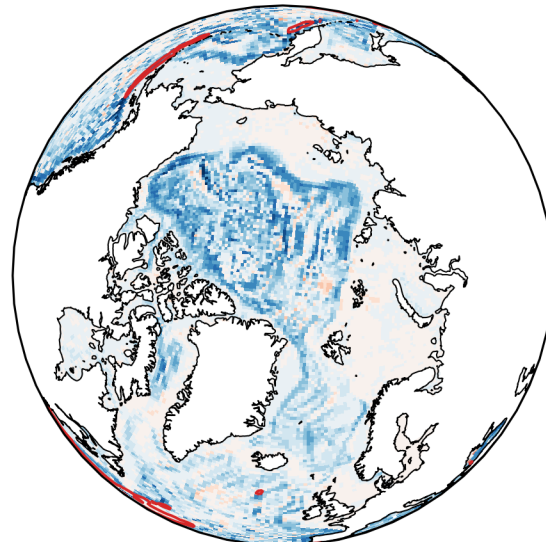
Figure 6.

Effect of topography

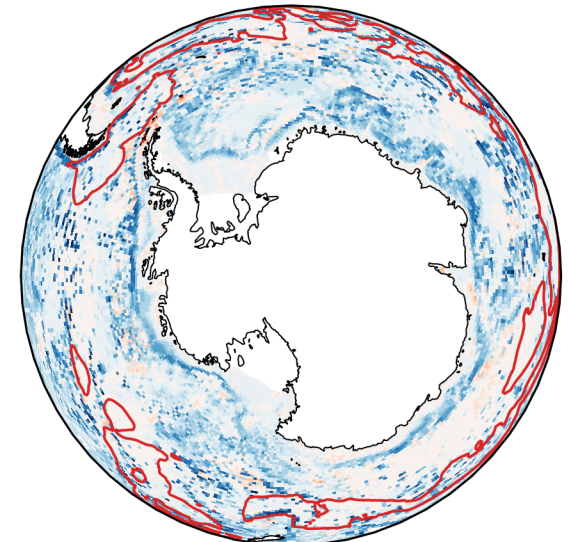
a



b

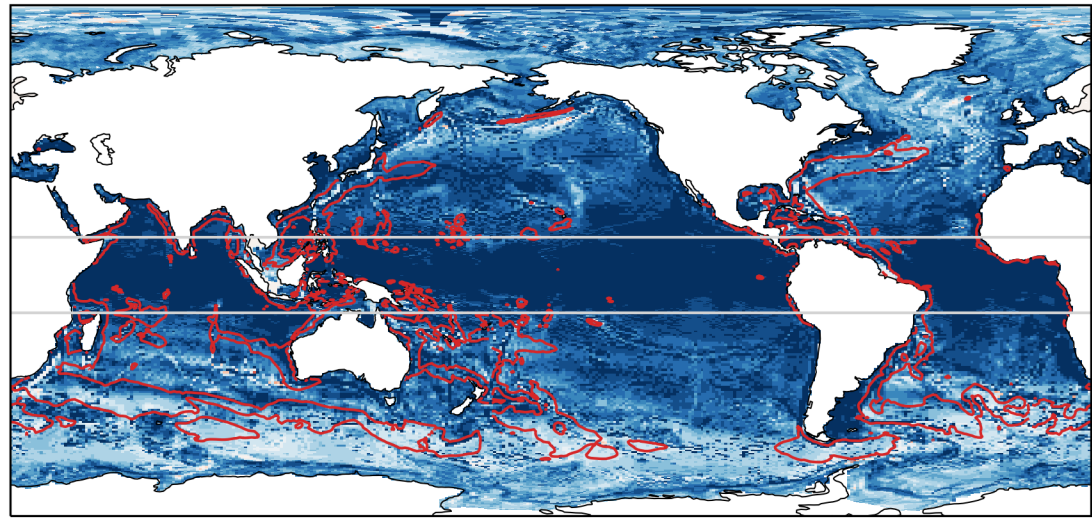


c

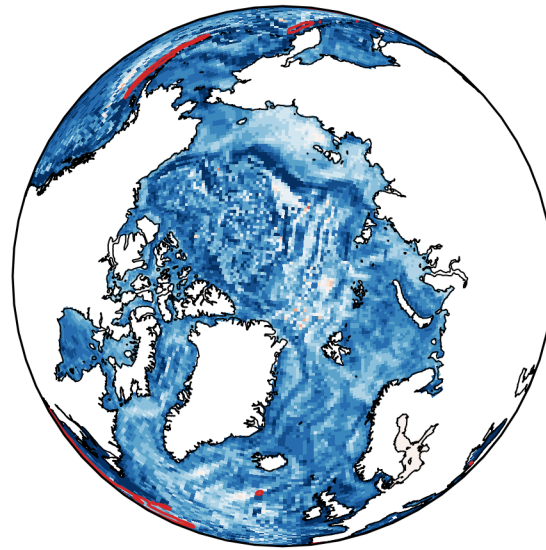


Effect of eddy efficiency and topography

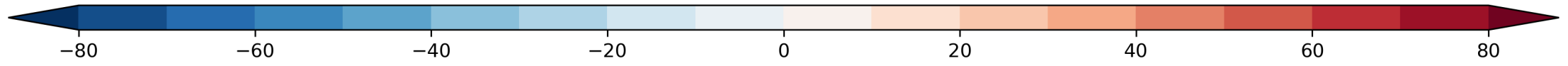
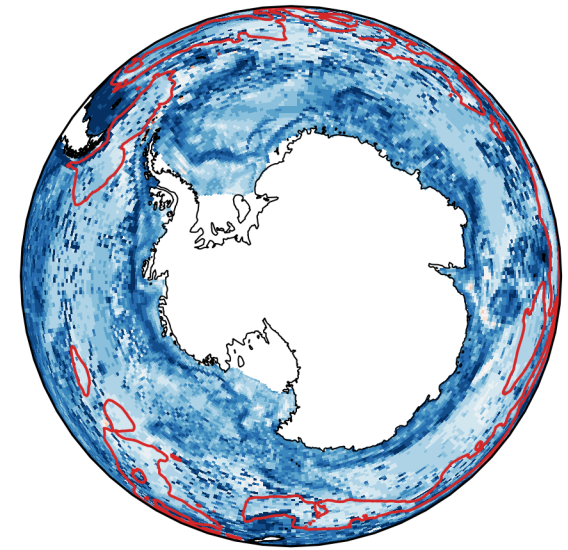
d



e



f

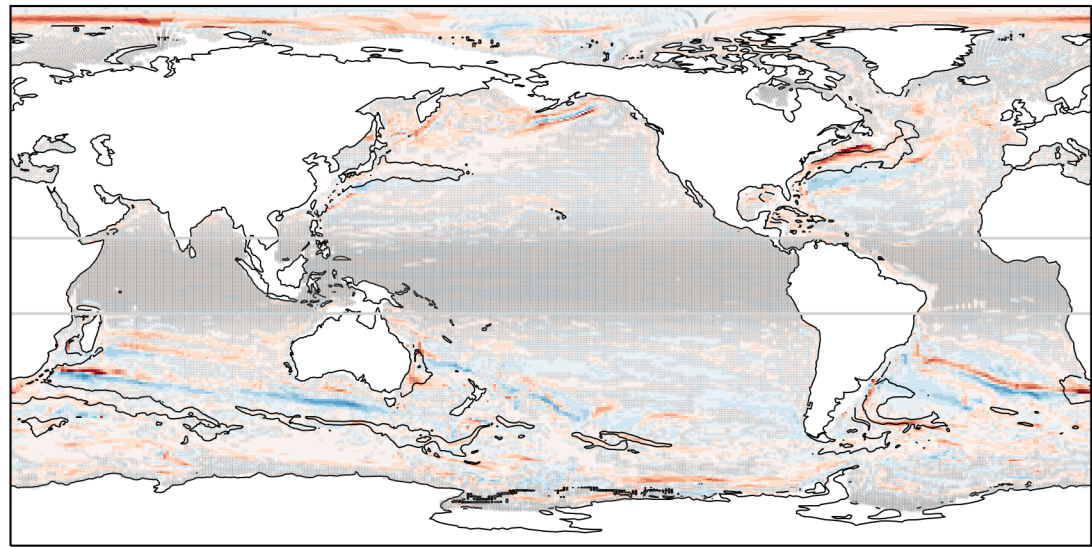


Buoyancy Diffusivity anomaly [%]

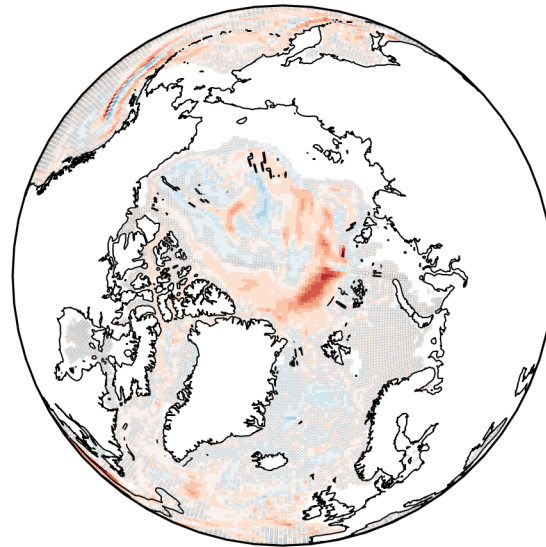
Figure 7.

Effect of topography

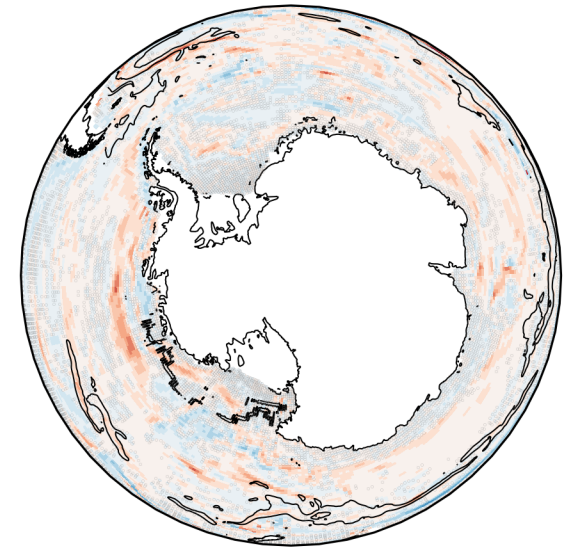
a



b

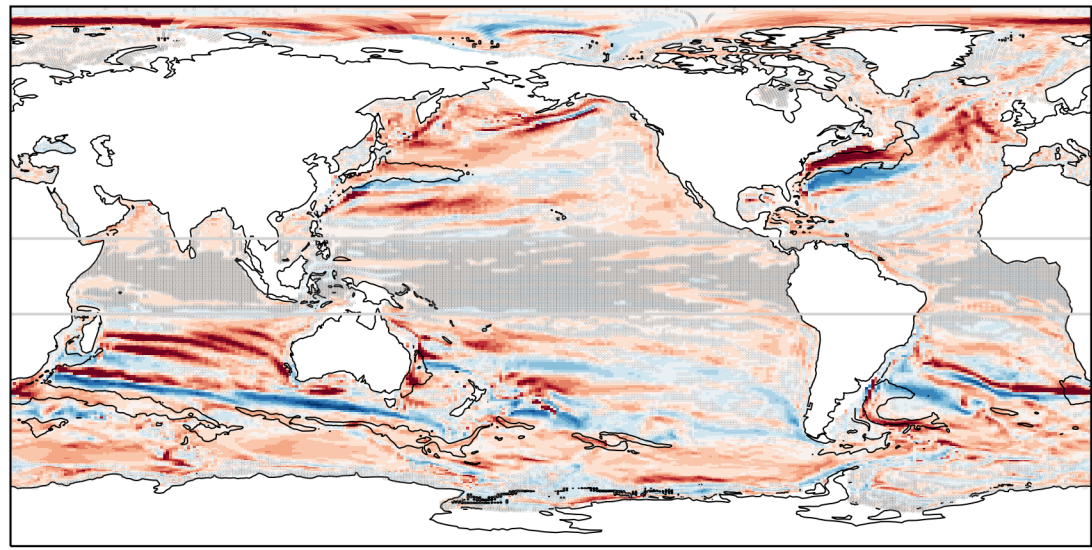


c

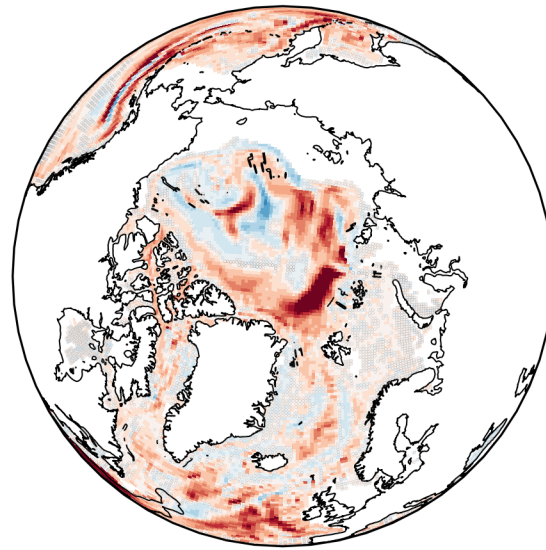


Effect of eddy efficiency and topography

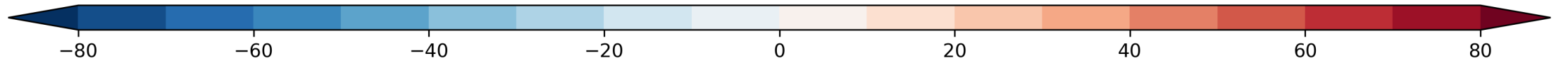
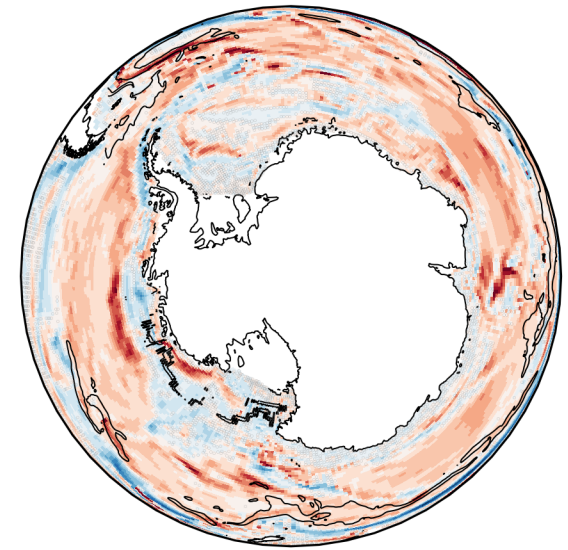
d



e



f

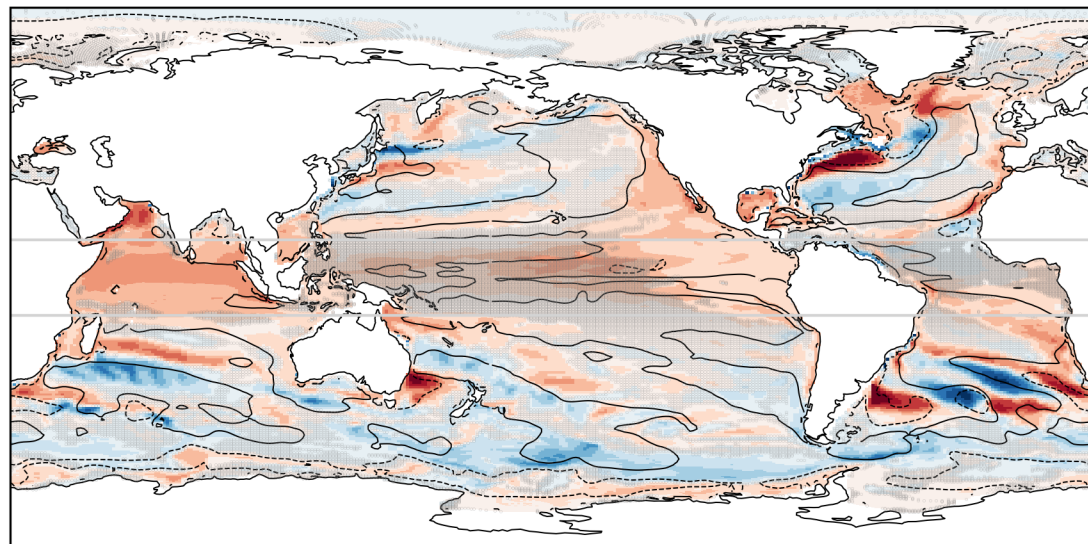


Speed anomaly [%]

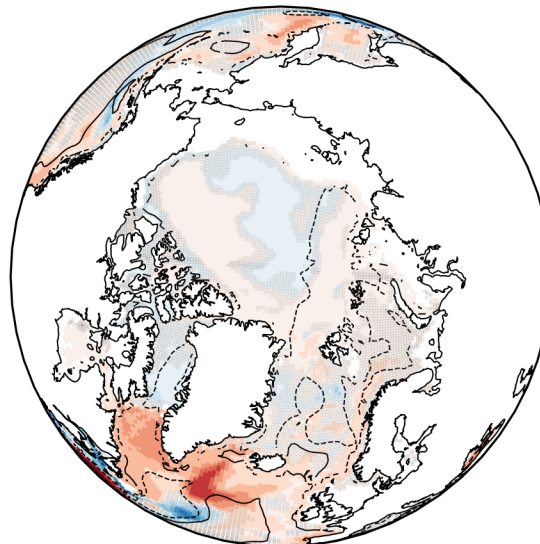
Figure 8.

Effect of topography

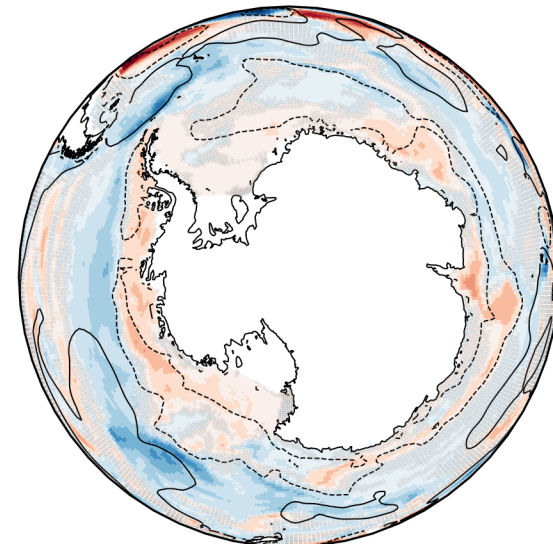
a



b

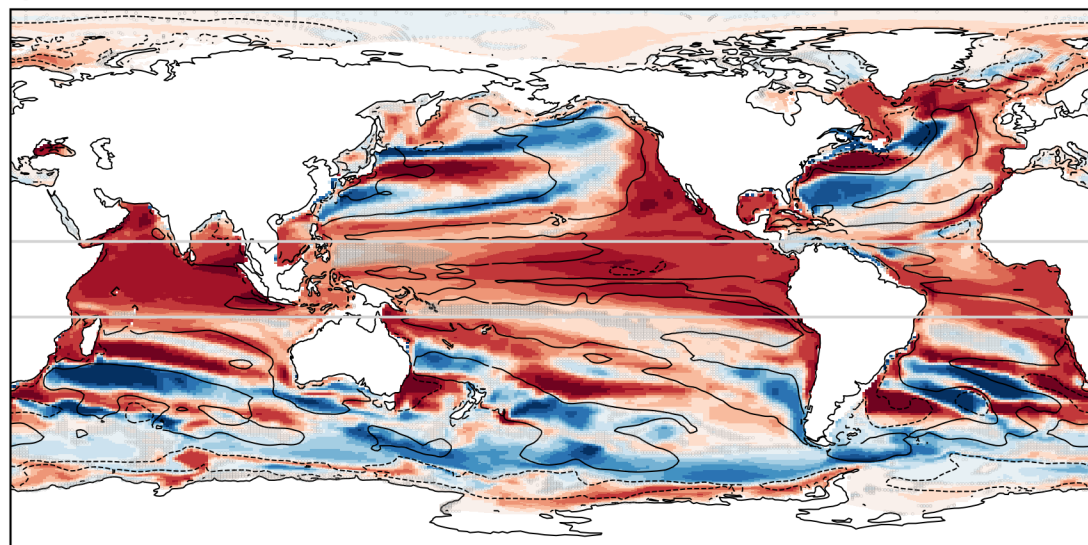


c

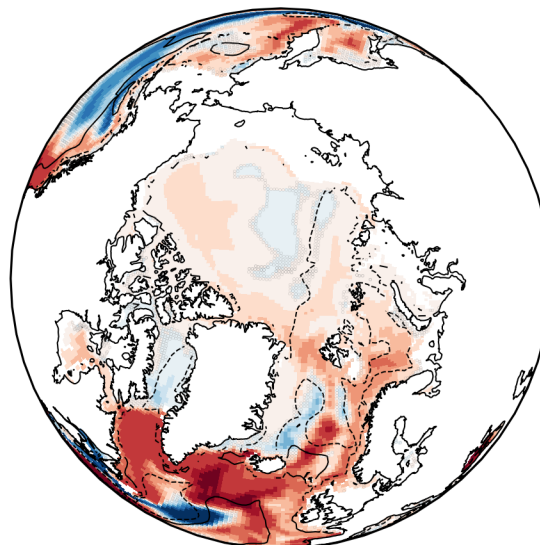


Effect of eddy efficiency and topography

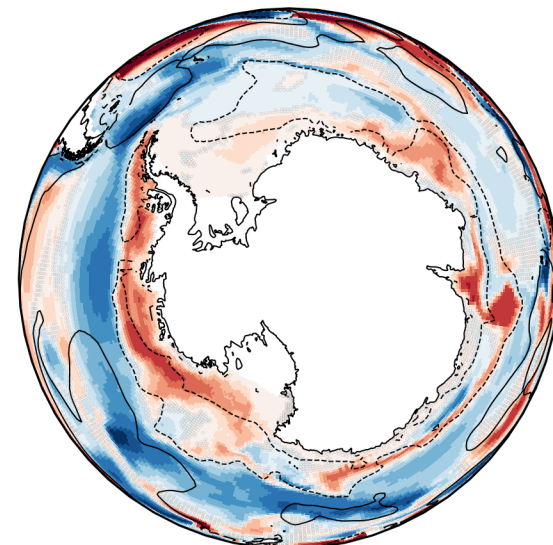
d



e



f



-0.75

-0.40

-0.20

0.00

0.20

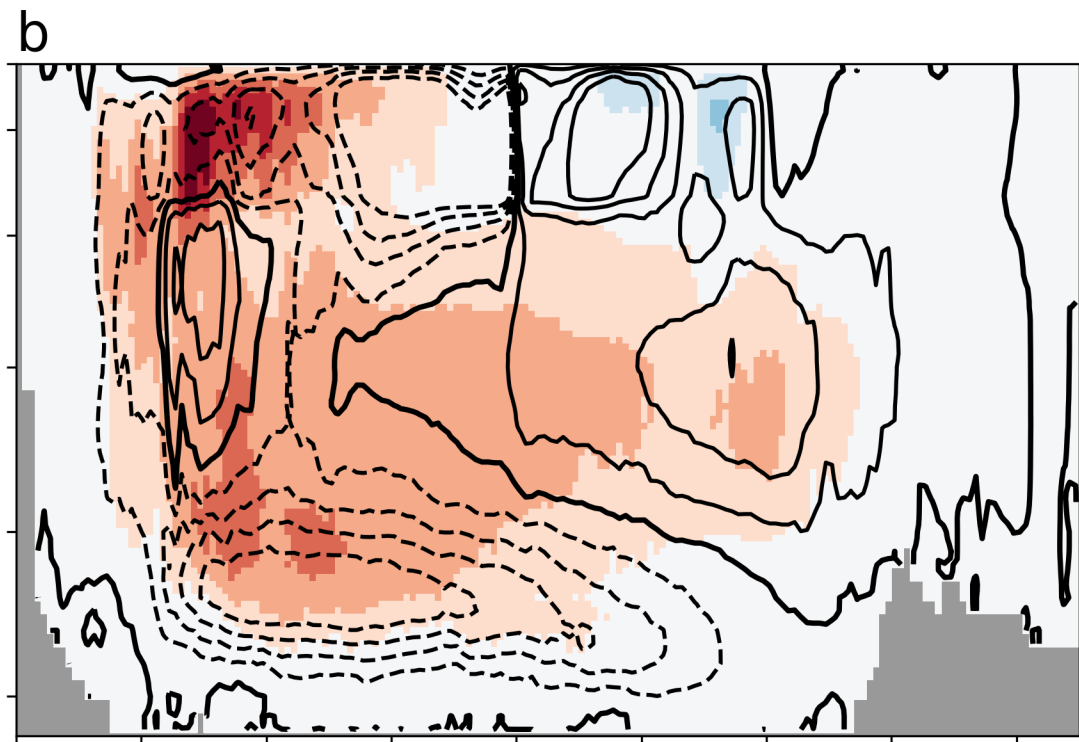
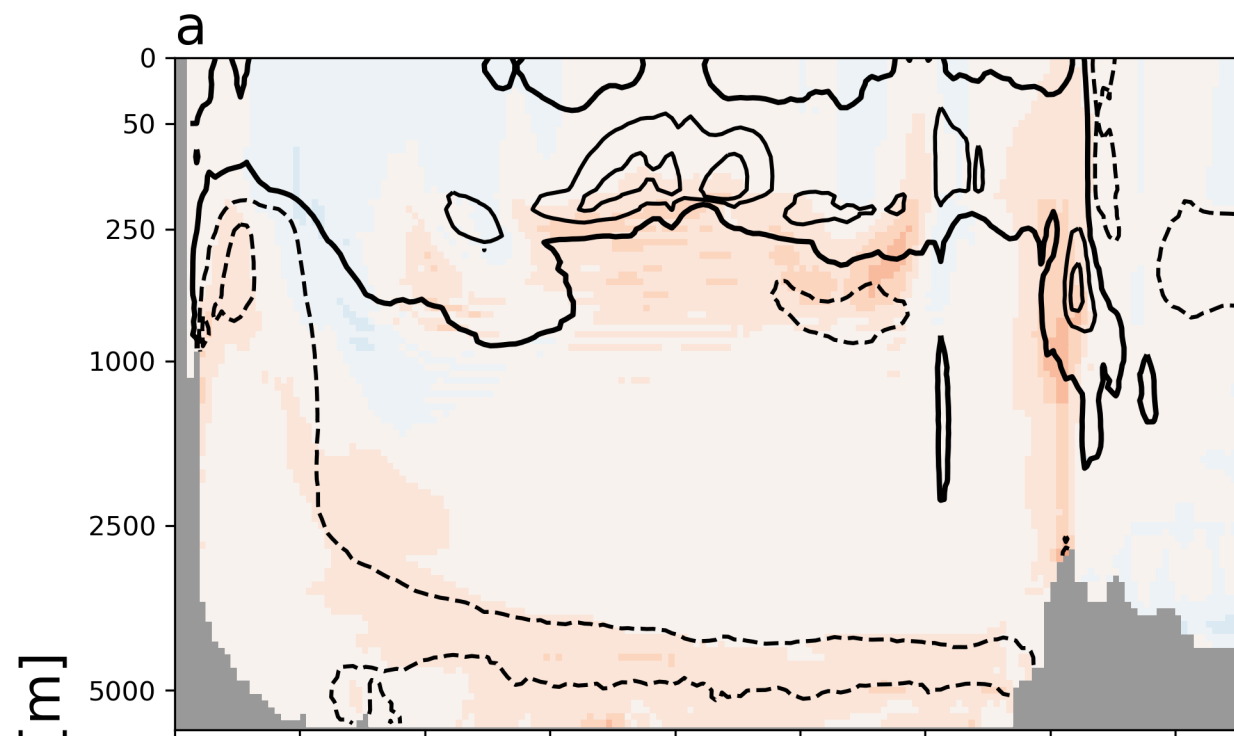
0.40

0.75

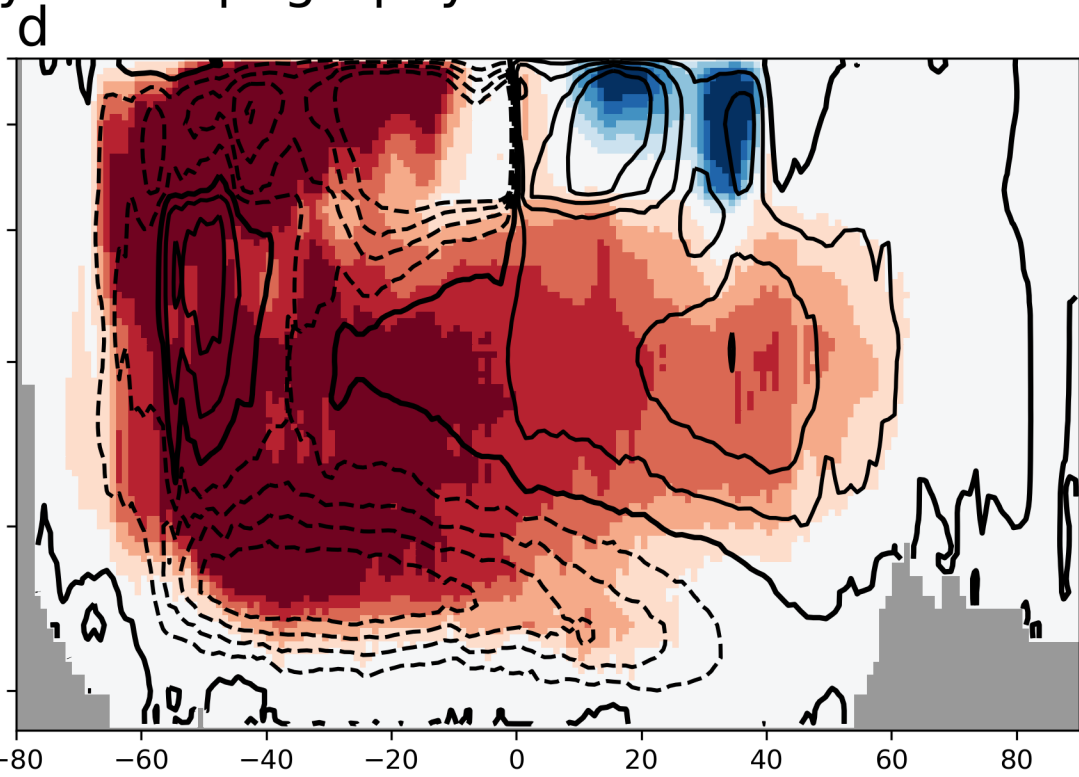
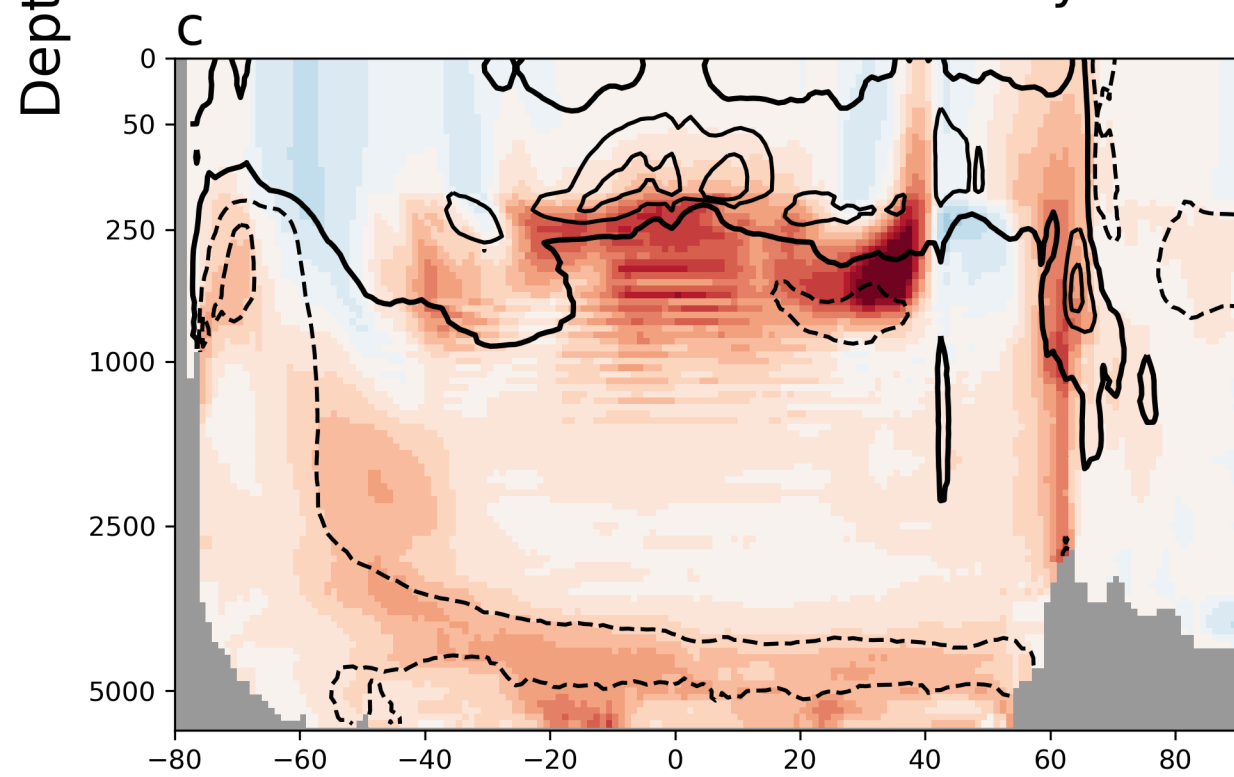
Temperature anomaly [°C]

Figure 9.

Effect of topography



Effect of eddy efficiency and topography



Latitude [$^{\circ}$ N]

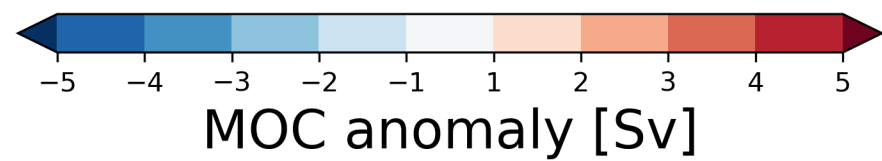
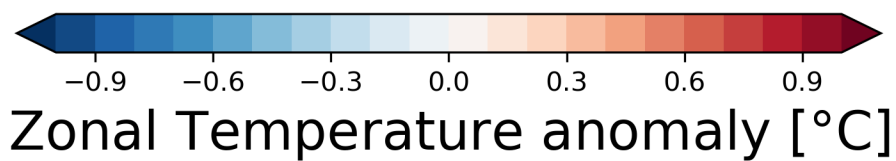


Figure 10.

